

# Modeling of the Near Infrared Emission From the Peculiar B[e]–Star MWC 349

**Dissertation**

zur

Erlangung des Doktorgrades (Dr. rer. nat)

der

Mathematisch–Naturwissenschaftlichen Fakultät

der

Rheinischen Friedrich–Wilhelms–Universität Bonn

vorgelegt von

**Michaela Kraus**

aus

Leonberg

Bonn 2000



# Contents

<b>Abstract</b>	<b>1</b>
<b>1 Introduction</b>	<b>3</b>
<b>2 The peculiar B[e] star MWC 349</b>	<b>9</b>
2.1 The nature of MWC 349 . . . . .	9
2.2 Observations and data calibration . . . . .	11
<b>3 The continuum of MWC 349</b>	<b>17</b>
3.1 The data . . . . .	17
3.2 Emission from the wind zone . . . . .	18
3.3 Emission from the dust disk . . . . .	28
<b>4 Hydrogen recombination lines</b>	<b>33</b>
4.1 Level population of recombined hydrogen atoms . . . . .	34
4.1.1 Debye-shielding . . . . .	37
4.1.2 The effect of pressure ionization . . . . .	39
4.2 Einstein coefficients of the neutral hydrogen atom . . . . .	41
4.3 Emission of the Pfund series . . . . .	41
<b>5 Modeling of the CO band emission</b>	<b>49</b>
5.1 The physics of CO molecules . . . . .	49
5.2 CO band emission under various circumstellar conditions . . . . .	54
5.2.1 A gaussian line profile for the CO gas . . . . .	55
5.2.2 CO bands from a Keplerian rotating disk . . . . .	59
5.2.3 Keplerian rotation plus gaussian component . . . . .	64
<b>6 Discussion</b>	<b>67</b>
<b>7 Conclusions</b>	<b>73</b>
<b>A Calculation of the gaunt factors <math>g_{\text{ff}}</math> and <math>g_{\text{fb}}</math></b>	<b>75</b>
<b>B The oscillator strength of neutral hydrogen</b>	<b>79</b>
<b>C Objects showing CO band emission</b>	<b>81</b>
<b>Bibliography</b>	<b>85</b>
<b>Acknowledgement</b>	<b>91</b>



# Abstract

The aim of this thesis is to investigate the first overtone band emission of CO from the peculiar B[e] star MWC 349. With the United Kingdom Infrared Telescope (UKIRT) in Hawaii, low resolution observations were made to determine the overall shape of the total band emission, and high resolution observations covering the  $(2 \rightarrow 0)$  and  $(3 \rightarrow 1)$  band heads to derive the velocity and optical depth of the CO gas.

Apart from the underlying continuum the observed spectra also show the existence of several hydrogen recombination lines contaminating the CO band spectrum. These contributions have to be discussed first to determine their influence on the total spectrum. Consequently, the thesis consists of three parts: The modeling of the continuum emission, the investigation of the Pfund line emission, and the discussion of the CO gas emitting the first overtone bands.

The continuum emission consists of several contributions. The radio range is dominated by free-free emission and the visible/ultraviolet part by free-bound emission, both occurring within the ionized wind zone. For the calculations, a wind model is discussed that allows the determination of several parameters like the electron temperature and radial distribution, and an estimate of the dimensions of the ionized stellar wind.

The infrared excess emission, on the other hand, is caused by circumstellar dust. The dust is arranged in a nearly edge-on circumstellar disk, and the contribution of this disk to the total continuum emission spectrum is modeled. The shape and strength of the disk spectrum strongly depends on the temperature and surface density distributions, the disk size and the inclination angle.

In the second part the contamination by the Pfund lines which arise in the ionized wind is discussed. Following Menzel's case B recombination theory, the emission is assumed to be optically thin. It is shown that the level population of the recombining hydrogen atoms are in local thermodynamical equilibrium. The model parameters that give the best fit agree with those found from the modeling of the continuum emission from the ionized wind.

The remaining part of the thesis deals with the hot CO gas. CO band emission is found in several young stellar objects, high-luminosity stars, and supergiants, all of them having large amounts of dust, especially in conjunction with a circumstellar disk. The  $(2 \rightarrow 0)$  band head which contains all the velocity information of the CO gas, has already been found to be a good tracer of the inner edge of circumstellar disks. Since the existence of a circumstellar disk around MWC 349 is quite sure, it seems to be the natural location of the CO gas.

Detailed calculations of different model scenarios are performed to locate the CO band emitting gas in the environment of MWC 349, because the  $(2 \rightarrow 0)$  band head shows no clear indication of pure rotational broadening. The most favoured scenario for the CO gas being located at the inner edge of the gas and dust disk proposes the existence of a disk bulge which absorbs radiation coming from the near part of the inner edge. The observer therefore only detects emission from a sector on the far side having a rather small radial velocity. Such a scenario opens prospects for future observations and more detailed model calculations.



# Chapter 1

## Introduction

MWC 349 is a really strange object. Although it has been known and analysed since the 1930s, no one has yet succeeded in determining the evolutionary state of this peculiar B[e] star. Many suggestions have been made ranging from a young stellar object (YSO) to an evolved asymptotic giant branch (AGB) star to a proto-planetary nebula. Recently, also Lamers et al. (1998) failed in fitting MWC 349 into their improved classification of B[e]-type stars because it shows characteristics of a pre-main sequence star as well as characteristics of a B[e] supergiant.

The detection of the first overtone band emission of CO, unfortunately, cannot help to decide into which category of objects MWC 349 belongs, but the study of these bands might bring us a bit closer to the nature of its circumstellar environment.

During stellar evolution, the production of heavy atoms like C, O, N, and Si occurs in nuclear synthesis. These elements are ejected into the interstellar medium (where they can form molecules) by various mass loss processes which may include stellar winds from giants and AGB stars, separation of stellar envelopes in planetary nebulae processes, and supernova explosions.

Carbon monoxide (CO) is a very stable molecule (dissociation at  $\sim 11$  eV). It is generally believed to be, after  $H_2$ , the most abundant molecule in the universe. Its millimeter wavelength rotational lines are widely used as tracers of molecular material both in hot diffuse clouds and in the denser and colder molecular clouds such as the dark clouds and the giant molecular complexes associated with H II regions. CO also serves to probe the molecular gas in other astrophysical objects such as comets, bipolar flows associated with regions of star formation, circumstellar envelopes and disks.

During the last 20 years emission of very hot CO gas ( $T_{CO} \simeq 2500 - 5000$  K) has been detected, for example in the circumstellar region of YSOs; the first one being the Becklin-Neugebauer (BN) object showing the first overtone bands (Scoville et al. 1979). These bands result from coupled vibrational-rotational transitions in the ground state of this diatomic molecule and can be found in the near infrared (NIR) part of the spectrum near  $2.3 \mu m$ . Other detections followed, ranging from low luminosity T Tauri stars to high luminosity YSOs embedded in molecular clouds (Geballe & Persson 1987; Carr 1989; Chandler et al. 1993; Greene & Lada 1996a; Najita et al. 1996).

In the following years several scenarios have been discussed to explain the origin of the hot and dense ( $n > 10^{11} \text{ cm}^{-3}$ ; Scoville, Krotkov & Wang 1980) CO gas. Accretion disk models have been proposed and investigated by Carr (1989), Calvet et al. (1991) and Chandler, Carlstrom & Scoville (1995). In the models of Calvet et al (1991) the disk is assumed to be optically thick at all radii, and the CO emission originates in the upper disk atmosphere in which a temperature inversion occurs by stellar irradiation. The other authors prefer a model in which the emission is produced in the inner regions of the disks which are assumed to be optically thin in the continuum. But both of these models are restricted to stars with relatively low mass accretion rates. The models of Calvet et al (1991) even predict the turn-over from emission to absorption with increasing accretion rates, a state which is inconsistent with the observation of strong CO band emission for example in the

T Tauri stars DG Tau and AS 353 A which are known to possess a strong accretion rate. To prevent such mispredictions, Najita et al. (1996) simply assumed a two-layer disk model in which the lower layer belongs to the continuum emission that can vary in optical depth, while in the upper layer the CO band emission is produced.

The possibility of the CO emission arising in a circumstellar wind or outflow has also been discussed (Carr 1989; Chandler, Carlstrom & Scoville 1995). The model spectra, however, are very sensitive to the wind parameters and there are many difficulties concerning the high CO temperature and density that are necessary for the CO bands to appear in emission. An additional mechanism to excite the first overtone bands has recently been proposed by Martin (1997). He suggests that the strong magnetic fields, which are known to exist in pre-main sequence stars, might disrupt the inner disk and channel the gas onto the stellar surface, thereby forming an accretion funnel which gives rise to the observed CO emission.

The discussion concerning the kinematics of the CO gas requires, however, that the NIR spectrum of the YSO of interest really exhibits CO band emission, because, as many observations of large samples showed, the NIR spectra of YSOs, particularly those of low luminosity and mass, rarely exhibit the overtone bands in *emission* but more commonly in *absorption* (see Table 1.1), and it turned out that the absorption is related to the spectral energy distribution (SED) class (e.g. Casali & Eiroa 1995, 1996; Greene & Lada 1996b).

**Table 1.1:** Samples of NIR observations of YSO.

Number of sample objects	Luminosity range [L <sub>⊙</sub> ]	Number of Objects with CO bands in		References
		Emission	Absorption	
Low Luminosity YSOs				
40	10 – 10 000	9	12	(1)
10	< 13	0	5	(2)
44	low	0	13/17 (≃ 76%) Class II 4/11 (≃ 36%) flat spectrum (Class I ?)	(3)
~ 100	0.1 – 50	2	all FU Ori type all Class III 90% Class II 60% flat spectrum none of Class I	(4)
High Luminosity YSOs				
16	≥ 10 <sup>4</sup>	4 + MWC 349	5	(5)

*References:* (1) Carr (1989); (2) Casali & Matthews (1992); (3) Casali & Eiroa (1995;1996); (4) Greene & Lada (1996b); (5) Geballe & Persson (1987).

Low luminosity YSOs can be classified by the shapes of their IR SED into an empirical evolutionary sequence (Lada 1987). Class 0 and Class I are the youngest and least evolved sources and most likely protostellar in nature (e.g. Adams, Lada & Shu 1987). They are surrounded by massive envelopes of gas and dust and their SEDs consequently peak in the far IR or sub millimeter. Class II sources are more evolved and commonly embedded T Tauri stars. They lack massive circumstellar envelopes and are usually optically visible. Their SEDs peak in the optical or near IR. Since they exhibit modest IR excesses they are believed to possess circumstellar accretion disks which give



rise to the NIR continuum emission. The most evolved objects (the classical pre-main sequence (PMS) stars of stellar evolution theory) belong to Class III. They lack both massive envelopes and circumstellar disks, and have SEDs of normal stellar photospheres without IR excess.

Greene & Lada (1996b) found that the strength of the CO *absorption* features is closely related to the SED class and the evolutionary state: The line strengths generally decrease from the unobscured Class III phase to the Class II phase to the deeply embedded Class I phase where absorption features are typically absent. This correlation of absorption strength with SED class is explained by the authors by a systematic increase in the veiling of an underlying stellar photosphere from Class III to Class I objects. They propose that the likely source of this veiling is continuum emission from increasing amounts of luminous circumstellar material surrounding these objects.

There exists, however, no common location of the CO gas around these objects: while in Class II and Class III sources the absorption is assumed to be produced in the photospheres (e.g. Casali & Eiroa 1996), it seems that in FU Ori type stars it comes from the interior of their accretion disks (e.g. Hartmann & Kenyon 1996). So the question we are dealing with is whether there is a common location around the YSOs where the CO band *emission* might occur.

The rapid technical developments of the last decades allows us now to make observations of high spectral resolution which are absolutely necessary to study the kinematics. By observing the CO ( $2 \rightarrow 0$ ) band head (i.e. the wavelength range with transitions of the form  $(v = 2, J) \rightarrow (v' = 0, J - 1)$ ) which defines the onset of the total band spectrum at its low wavelength end, it became obvious that the shape of this band head contains the complete velocity information of the gas, and that the most likely location of the hot and dense CO gas is indeed a neutral wind or a circumstellar disk.

**Table 1.2:** YSOs whose high resolution spectra of the  $(v = 2 \rightarrow v' = 0)$  band head could be modeled by either a Keplerian disk motion or a wind scenario. For NGC 2024 IRS 2 both models show good fits, while for SVS 13, S 106 IRS 4, and V 1331 Cyg a wind plus disk solution would better match the data. The investigation whether MWC 349 can also be fit by one of these scenarios is subject of this thesis.

Name	$\Delta v_{\text{res}}$ [km/s]	Wind Model			Keplerian Disk Model			Variable <sup>d)</sup>	Ref.
		$v_{\text{max}}$ [km/s]	$\Theta^a)$ [°]	$j^b)$ [°]	$R_i$ [R <sub>☉</sub> ]	$v_{\text{rot}}$ [km/s]	$i^c)$ [°]		
DG Tau	19	110	25	55				strongly	(1)
NGC 2024 IRS 2	19	~ 300	13	78	60	220	57		(1)
SVS 13	19				$\geq 5$	$\leq 200$	78	strongly	(1)
S 106 IRS 4	19				(175	165	25)	not	(1)
V 1331 Cyg	15							strongly	(2)
WL 16	13				$< 8$	290	30	not	(3)
	38				4.2	335	30		(1)
	7.5				5	300–310	30		(4)
1548 C 27	7.5				20	$\leq 200$	60	strongly	(4)
MWC 349	10–15							unknown <sup>e)</sup>	(5)

<sup>a)</sup> semiopening angle of the wind cone

<sup>b)</sup> inclination angle of the out flow axis with respect to the line of sight

<sup>c)</sup> inclination angle of the disk with respect to the line of sight ( $i = 0^\circ$  means edge on)

<sup>d)</sup> based on monitoring observations of the CO bands performed by Biscaya et al. (1997)

<sup>e)</sup> MWC 349 is, however, known to be a variable source in the visual spectral region

*References:* (1) Chandler, Carlstrom & Scoville (1995); (2) Carr & Tokunaga (1992), (1995); (3) Carr et al. (1993); (4) Najita et al. (1996); (5) this thesis.

From the literature a list of YSOs has been collected whose  $(2 \rightarrow 0)$  CO band head has been modeled. This list which is displayed in Table 1.2 strengthens the assumption that the emission of most of the objects originates in a Keplerian rotating disk rather than in a wind. But at first glance, a possible wind component in addition to the disk component cannot entirely be excluded. Although the existence of a circumstellar gas and dust disk has not yet been confirmed by the observations for all of these objects (see Table C.2 in Appendix C), it is quite convincing that with high spectral resolution observations of the  $(2 \rightarrow 0)$  band head a powerful tracer for circumstellar disks around YSOs is given (e.g. Najita et al. 1996; Kraus 1997).

But the phenomenon of CO band emission is not only a property of *young* stellar objects. Also the NIR spectra of several high-luminosity (P Cygni) emission line stars as well as some supergiants in our neighbouring galaxy, the Large Magellanic Cloud, show clear emission of the CO first overtone bands, and most of these sources seem to be surrounded by a dense disk or at least a dense dust shell. Even more curious was the detection of CO band emission in some relatively cool post AGB stars / proto-planetary nebulae. In at least two of the five sources the CO bands are variable appearing alternately in emission and in absorption. For HD 170756 (= AC Her) Oudmaijer et al. (1995) found that these changes are related to the pulsation period of the post AGB star indicating that emission occurs when the photosphere is contracting while absorption takes place when it is expanding. The authors propose that when the CO is in emission, it could trace a part of the envelope that is detached from the photosphere and might continue to expand or eventually fall back again if the outflow velocity is too low to escape. If this is correct, then the CO emission is related to episodic mass loss during a pulsation cycle. A list of all of the objects mentioned here is given in Table C.3 in Appendix C.

An additional really strange detection of CO band emission occurred during monitoring the NIR spectra of three recent Type II supernova explosions, namely SN 1987 A (Spyromilio et al. 1988), SN 1995 ad (Spyromilio & Leibundgut 1996), and SN 1998 S (Gerardy et al. 1999). The CO bands were found to disappear several months after maximum light because of the dilution in density as the remnant expanded. The discovery of emission from molecules near a supernova revolutionized the opinion, that the production of molecules cannot take place within the ejecta of supernova explosions.

We have seen that the appearance of CO band emission is a wide spread phenomenon arising in numerous very different types of objects. But these objects seem all to have either a circumstellar disk or a dense neutral wind or outflow in which the CO band emission can occur.

This thesis is engaged in a study of the peculiar B[e] star MWC 349. Earlier, low resolution observations already reported the detection of the first overtone CO bands in emission from this object (Geballe & Persson 1987). However, the evolutionary state of MWC 349 is still unknown, and a priori we cannot arrange it in one of the categories of CO band emitting objects listed above. But it is known to possess a dense circumstellar environment, including a neutral nearly edge-on gas and dust disk (see Chapter 2.1) which seems to be a promising location for the hot CO gas. For the investigation whether the emission is really connected to the circumstellar disk, the aim of this thesis, high resolution observations especially of the  $(2 \rightarrow 0)$  band head are necessary. Here we present new low and the first high resolution spectra of the CO first overtone band emission from MWC 349.

In Chapter 2, MWC 349 is introduced and its peculiarities are outlined. In addition the observations of the first overtone bands are presented together with a description of the data analysis and the flux calibration. Apart from the CO bands the spectra also contain higher order Pfund lines (i.e. transitions of the form  $n \rightarrow n' = 5$ ) of the hydrogen atom.

Chapter 3 deals with the modeling of the continuum data collected from the literature. The observations cover a wavelength range from the radio (21 cm) down to the visible (400 nm). It is found to consist of several contributions: free-free and free-bound emission from an optically thick wind zone in which the electron density varies with radius as  $r^{-2}$ , emission from a circumstellar

gas and dust disk seen nearly edge on, and emission from the central star.

In Chapter 4, first an introduction into recombination theory is given which also allows deviations from the local thermodynamic equilibrium (LTE). After that, the Pfund line emission is modeled (i) with a gaussian line profile, and (ii) arising in a spherical wind zone of constant wind velocity. The model parameters needed to fit the observed flux densities of the Pfund lines are compared to the ones found from modeling of the continuum emission from the wind zone, and deviations are discussed.

After a short presentation of the theory of CO bands, possible kinematical scenarios that result in CO band spectra of typical shape are investigated in Chapter 5. Of special interest is of course whether the CO bands can be modeled under the assumption of a Keplerian rotation of the CO gas. But also several other line profiles which result from the gas motion are discussed like a gaussian (or nearly gaussian) one in the case of a wind, or a profile which connects a rotation with a gaussian motion that can be expected from a disk plus wind solution.

In Chapter 6 the different models presented in the previous chapter are investigated in view of the real circumstellar conditions around MWC 349. The problems of the individual models are brought out and discussed, and a possible location of the CO band emitting gas is proposed.

Finally, Chapter 7 summarizes the main results and gives an outlook to future investigations that might help to find out the secrets of this peculiar star.



## Chapter 2

# The peculiar B[e] star MWC 349

### 2.1 The nature of MWC 349

MWC 349 was discovered during a survey of emission line stars of early spectral type (Merrill, Humason & Burwell 1932). It is located in direction to the Cygnus–X region, south of the OB 2 association (galactic coordinates:  $79.64 +0.47$ ). It is not clear whether MWC 349 whose distance has been determined to  $\sim 1.2$  kpc (Cohen et al. 1985) belongs to this association. The system MWC 349 is a binary consisting of the main component, MWC 349 A, we are interested in, and a B0 III companion, MWC 349 B, some  $2''.4$  west of the main component. For we are only interested in the main component, it will in the following be referred to as MWC 349. Its bolometric luminosity which suffers a visual extinction of  $A_V \simeq 10$  mag (two of them are thought to be circumstellar), is  $\sim 3 \cdot 10^4 L_\odot$  (Cohen et al. 1985). The circumstellar extinction seems also to be responsible for the systematic drop in visual magnitude starting with 13.2 mag in 1932 (Merrill, Humason & Burwell 1932), passing 14 mag in 1942 (Swings & Struve 1942), and reaching  $\sim 15.5$  mag in 1972 (Braes, Habing & Schoenmaker 1972).

The evolutionary state of MWC 349 is still unclear. Even the improved classification of B[e]–type stars by Lamers et al. (1998) leaves the type of MWC 349 still undetermined, because it shows some characteristics of a pre–main sequence B[e]–type star as well as characteristics of a B[e] supergiant. It is, however, a peculiar B[e] star because of its countless emission lines of both allowed and forbidden transitions. The existence or even non–existence of numerous ionization and excitation states allows to divide the circumstellar envelope of MWC 349 into several spatially distinct regions of different temperature and density (Hamann & Simon 1986; 1988), one being probably a circumstellar disk.

According to the strong IR excess, it has been known for a long time that there must be a bulge of circumstellar dust around MWC 349 (e.g. Geisel 1970). The proposition that MWC 349 also has a disk was supported by observations of double–peaked emission lines (Hamann & Simon 1986, 1988) and by NIR speckle interferometry (Leinert 1986; Mariotti et al. 1983) which revealed a disk–like structure of the dust emission in the east–west direction, seen nearly edge on.

The detection during the seventies that MWC 349 is even a very strong radio source made this star become more and more curious (Braes, Habing & Schoenmaker 1972; Altenhoff & Wendker 1973; Hjellming, Blankenship & Balick 1973; Gregory & Seaquist 1973). The spectral index found from these observations gave hint to an optically thick wind zone of non–constant electron density, and first, low resolution observations showed a spherical distribution of the free–free emission from the wind zone (Baldwin, Harris & Ryle 1973) whose mass loss rate found for a 50 km/s wind velocity is  $\sim 1.2 \cdot 10^{-5} M_\odot \text{yr}^{-1}$  (Cohen et al. 1985). Later on observations with the VLA better resolved the wind zone. These maps show a square shape of the envelope at 6 cm (Cohen et al. 1985) and a striking bipolar shape at 2 cm (White & Becker 1985), which also speaks in favour of an accumulation of neutral gas and dust in the equatorial plane.

Additional indicators for the circumstellar disk are the strong hydrogen recombination maser lines in the mm and submm range (e.g. Martín–Pintado et al. 1989). These maser lines have double-peaked profiles indicating a rotational motion of the gas. Recombination lines at different wavelengths sample different regions, which means that with decreasing quantum number  $n$ , i.e. increasing frequency, one sees ionized gas closer to the star. The fact that the rotational velocity of recombination lines with decreasing  $n$  displays a systematic increase led to the assumption that the double-peaked maser emission comes from the ionized atmosphere of a Keplerian rotating disk (Thum, Martín–Pintado & Bachiller 1992; Thum et al. 1994b). Rodríguez & Bastian (1994) could even determine the inclination angle of the disk towards the line of sight to  $15^\circ \pm 5^\circ$ .

**Table 2.1:** A sample of lines with an observed rotational velocity. The radial distance,  $r$ , was calculated for a  $26 M_\odot$  star. *References:* (1) Hamann & Simon (1986); (2) Thum et al. (1994a); (3) Thum et al. (1994b); (4) Thum et al. (1995); (5) Rodríguez & Bastian (1994).

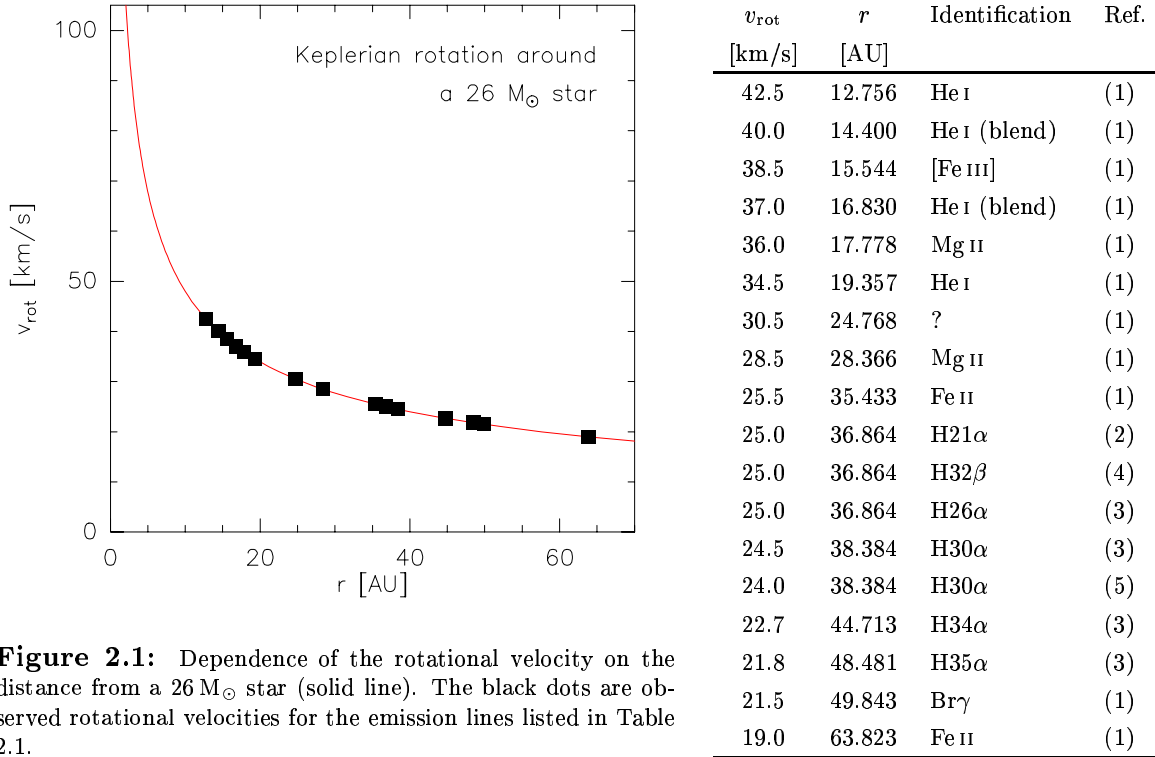


**Figure 2.1:** Dependence of the rotational velocity on the distance from a  $26 M_\odot$  star (solid line). The black dots are observed rotational velocities for the emission lines listed in Table 2.1.

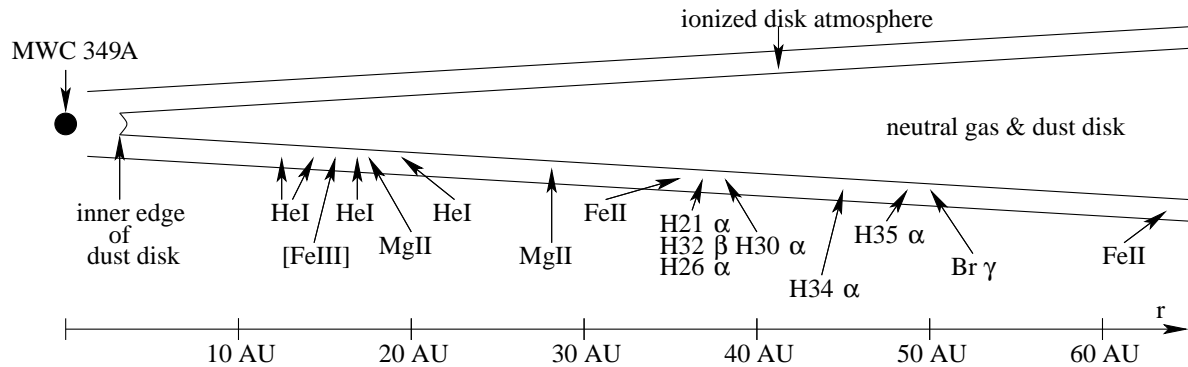


**Figure 2.2:** Sketch of the rotating disk and disk atmosphere around MWC 349 seen edge on. Shown are the locations of the observed rotating emission lines listed in Table 2.1.

We know from the observations that the H30 $\alpha$  recombination line is located at a distance of  $\sim 40$  AU from the star with a rotational velocity of  $\sim 24$  km/s (Planesas, Martín-Pintado, & Serabyn 1992). If we assume the recombination lines to come from the ionized skin of the Keplerian rotating disk, the mass of MWC 349 would be  $\sim 26 M_{\odot}$ . With the known mass of the central star we are able to localize the double-peaked emission lines mentioned above. The orbital velocity as a function of radial distance from the  $26 M_{\odot}$  central star is plotted as the solid line in Figure 2.1 and the black dots represent the emission lines collected from the literature which are expected to take part of the Keplerian rotation because of their double-peaked profiles, and whose distance from the  $26 M_{\odot}$  central star is calculated according to the Keplerian rotation law (see Table 2.1).

To get an impression of the circumstellar environment we translated these informations into a global picture: a disk with a corotating ionized atmosphere that gives rise to the double-peaked emission lines of the ionized heavy atoms and the hydrogen recombination maser lines. A sketch of a cut through this disk seen edge on is shown in Figure 2.2, but we should keep in mind that it can represent only a rough illustration of the real circumstellar region because still little data about MWC 349 are at hand.

## 2.2 Observations and data calibration

In 1997 we observed MWC 349 with the UKIRT telescope in the NIR range ( $1.85 - 2.5 \mu\text{m}$ ) with a spectral resolution of  $\sim 330$  km/s (Fig. 2.3).

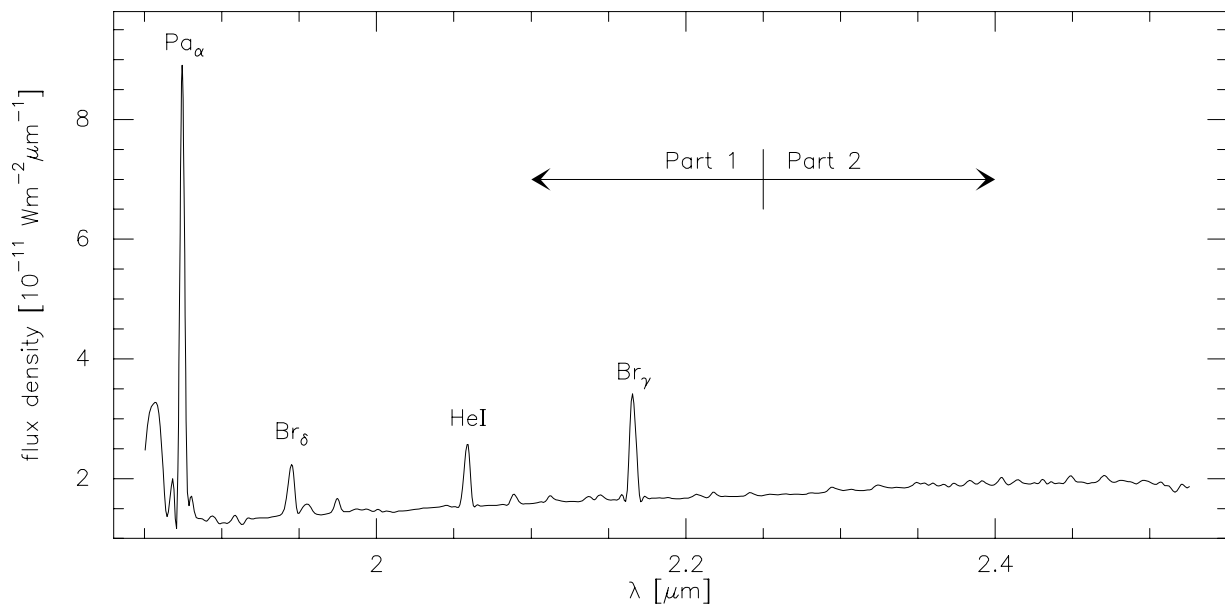


**Figure 2.3:** NIR spectrum of MWC 349 observed with UKIRT with a spectral resolution of  $\sim 330$  km/s. To emphasize the emission lines beneath the hydrogen lines we split the spectrum into two parts.

The most prominent emission lines within the spectrum are hydrogen and helium recombination lines. To show also several additional emission lines which are not this strong we partitionated the spectrum in two parts shown in Figure 2.4 (a) and (b). The list of some possible identifications of the emission lines in Part 1 (wavelength range  $1.85 \mu\text{m} - 2.25 \mu\text{m}$ ) is given in Table 2.2.

Part 2 (Figure 2.4 (b)) is the more interesting spectral range for this work. It covers the wavelength range from  $2.25 \mu\text{m}$  to  $2.5 \mu\text{m}$ . Apart from the CO first overtone band emission (indicated by the arrows) also most of the Pfund lines of the hydrogen atom are identified (vertical bars).

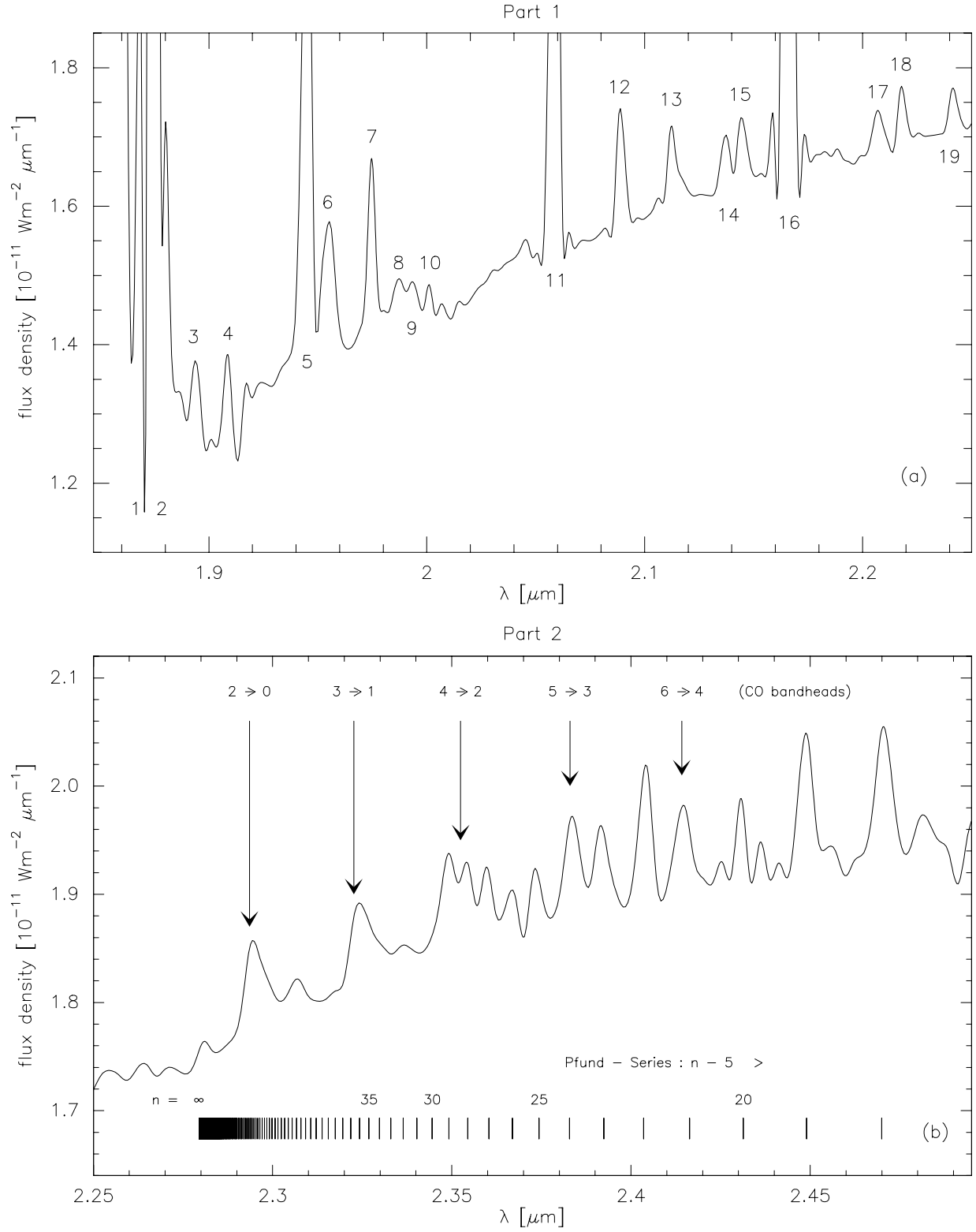


**Figure 2.4:** The two parts of the observed NIR spectrum: Part 1 (upper panel) shows a large number of emission lines that are identified and listed in Table 2.2. Part 2 (lower panel) contains the first overtone CO bands (indicated by the arrows) and most lines from the Pfund series of the hydrogen atom (vertical bars).



**Table 2.2:** List of probable identifications of the marked emission lines in the NIR spectrum of MWC 349 (Figs. 2.3 and 2.4 (a)).

number	wavelength [ $\mu\text{m}$ ]	line identification
1	1.86904	He I
2	1.87561	Pa $\alpha$
3	1.89282	C I, Ca I
4	1.90867	He I
5	1.94508	Br $\delta$ , Ca I
6	1.95445	N I
7	1.97470	Si I, C I, N I
8	1.98702	Ca I, C I
9	1.99318	Ca I, Si I, C I
10	2.00130	C I
11	2.05917	He I
12	2.08819	(?) Sn I, Fe II
13	2.11194	He I
14	2.13831	Mg II, C I, Si I
15	2.14359	Mg II, Ca II, [Fe III]
16	2.16611	Br $\gamma$
17	2.20687	Na I doublet, Si I, (?) O II
18	2.21741	C I
19	2.24113	(?) Fe II

An earlier study of CO band emission showed that for a low spectral resolution as it is the case in these observations all the velocity information of the CO gas is lost (Kraus 1997). Therefore, we reobserved the region containing the  $(2 \rightarrow 0)$  band head in June 1998 and in August 1998 the region around the  $(3 \rightarrow 1)$  band head. The spectral resolution is now 10 – 15 km/s. The way of calibrating the high resolution spectra is shown in Figure 2.5 (a) - (g):

The observations were split in four parts which have a small overlap at their edges, and each subspectrum was divided by the spectrum of  $\alpha$  Cyg during the observations to omit atmospheric influences (a). As can be seen, the subspectra are offset to each other, and at their low wavelength end, the measurements seem to be systematically too high. To make clear the wavelength ranges covered by each subspectra we plotted them in alternating colors.

The subspectra were sampled every 1/3 resolution element. So, we first smoothed them to their real resolution (b) and multiplied them afterwards with the continuum spectrum of  $\alpha$  Cyg given by Barlow & Cohen (1977) (c). Next, we smoothed the subspectra to the resolution of  $\sim 330$  km/s, i.e. to the same one as for the spectrum in Fig. 2.4 (b), and plotted them together with the spectrum of low resolution (d). Then we scaled each high resolution subspectrum with a factor near  $\sim 1$  so that the subspectra (red line) and the original spectrum of low resolution (blue line) could be made agree (e). To get an idea of the agreement between the red and blue curve we calculated the residue by subtracting the original low resolution spectrum from the smeared subspectra (g).

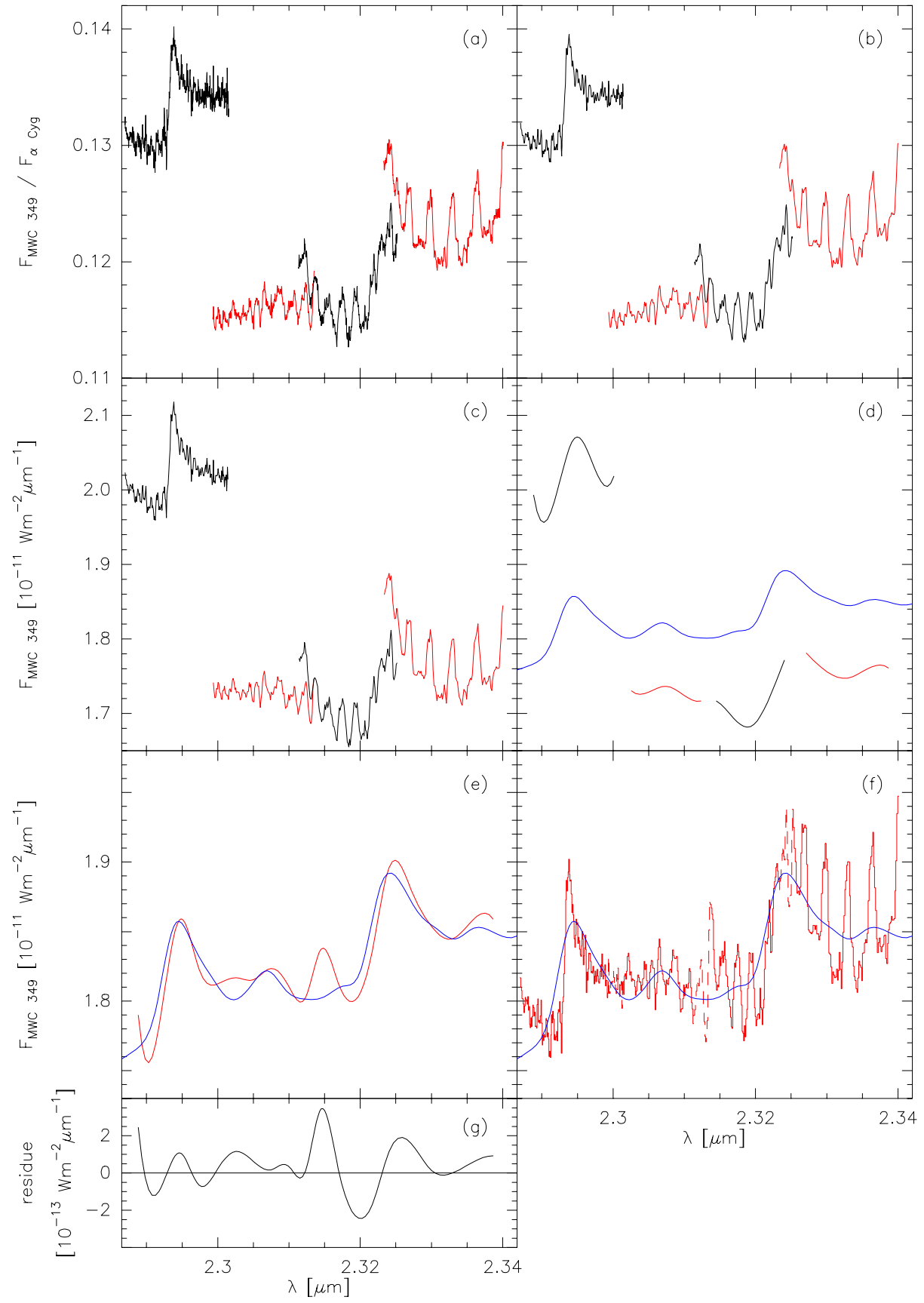


**Figure 2.5:** The different steps to calibrate the high resolution data. For more details see text.

Finally, we multiplied the high resolution subspectra with each corresponding scaling factor and combined them to the resulting total high resolution spectrum (red line, f).

The plot of the residue contains several features especially at wavelengths where the spectra were put together. This behaviour supports the assumption that the measurements seem to have a systematical fault. Another problem with the high resolution subspectra is the fact that the structure of the  $(3 \rightarrow 1)$  band head has been split during the observations. The strength of this band head is therefore subject to some uncertainty.

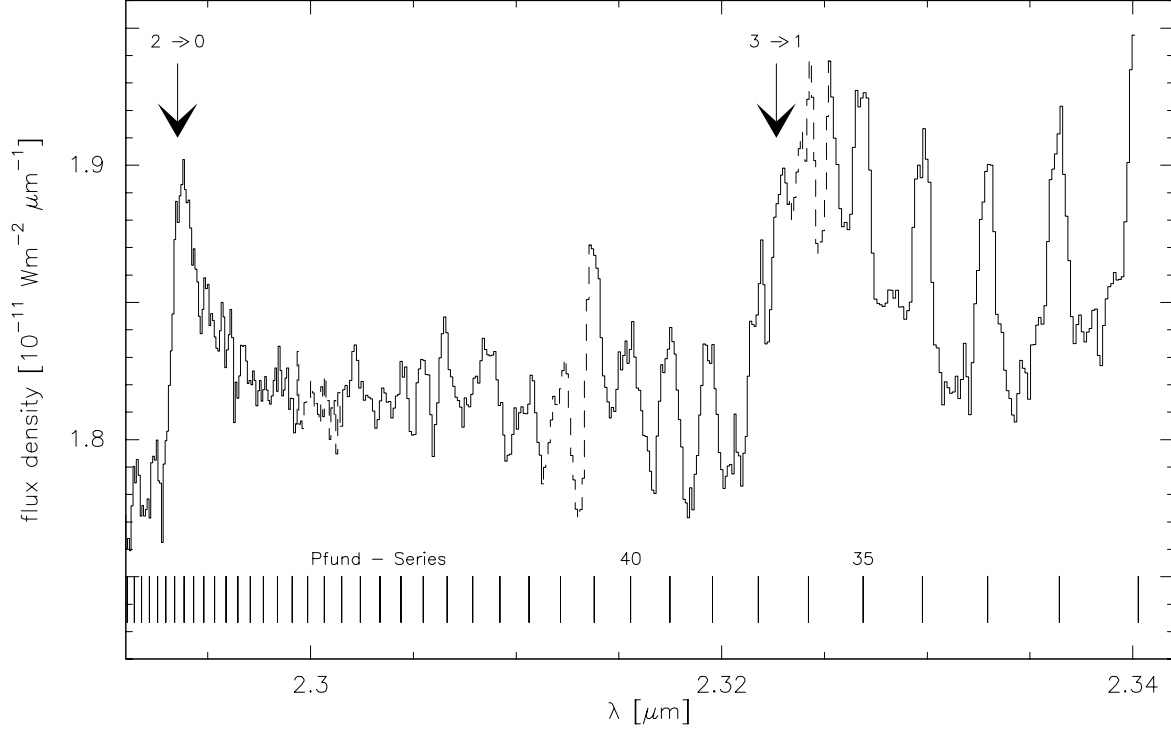


**Figure 2.6:** The absolute calibrated high resolution spectrum of MWC 349. The spectrum contains the  $(2 \rightarrow 0)$  and  $(3 \rightarrow 1)$  band heads of the CO molecule (arrows) and a number of Pfund lines of the hydrogen atom (vertical bars). The dashed regions within the spectrum mark the regions of calibrational uncertainties.

In Figure 2.6 we replotted the absolute calibrated high resolution spectrum. Also shown are the locations of the  $(2 \rightarrow 0)$  and  $(3 \rightarrow 1)$  band heads of the CO molecule as well as the rest wavelengths of the Pfund series of the hydrogen atom. As most locations of the emission features in the spectrum can be identified with one of the laboratory wavelengths of either CO or H, we assume the NIR spectrum of MWC 349 to consist of mainly three emission components: the continuum, parts of the Pfund series of the hydrogen recombination lines, and the CO  $\Delta v = 2$  bands.

The main attention of this work devotes to the modeling of the CO first overtone band emission and to the kinematics of the circumstellar molecular gas that can be obtained from this modeling. But before we can turn to the CO emission we first have to discuss the underlying continuum and the superimposed Pfund lines which contaminate the CO emission. This ‘cleaning’ procedure is performed in the two subsequent chapters.



## Chapter 3

# The continuum of MWC 349

### 3.1 The data

The continuum data of MWC 349 collected from the literature (Table 3.1) cover the wavelength range from the radio (21 cm) down to the visible (400 nm) and are plotted in Figure 3.1.

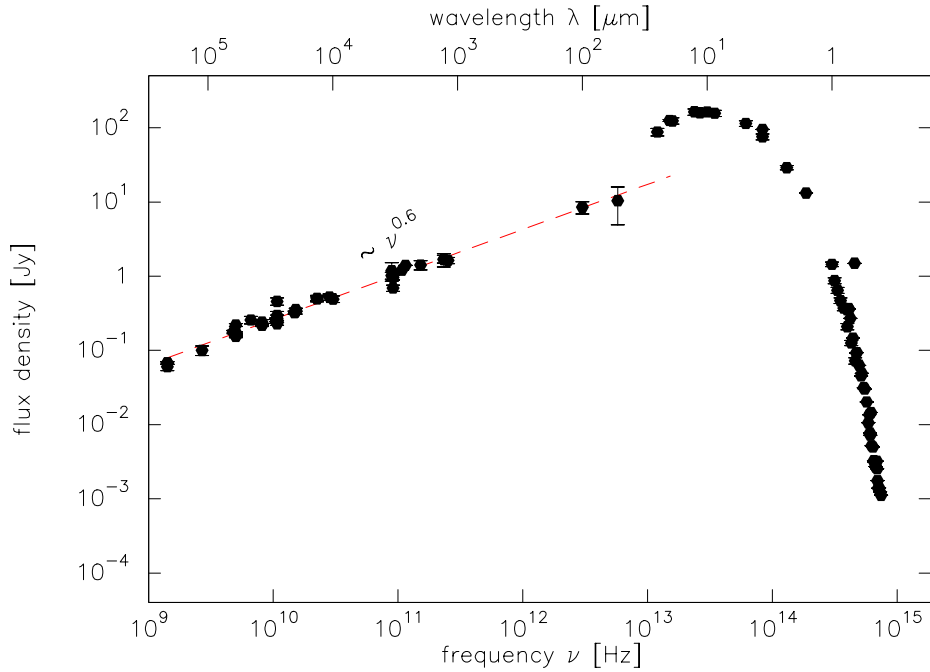


**Figure 3.1:** The complete continuum emission of MWC 349. The observations collected from the literature (big dots, see Table 3.1) can be fitted in the radio range with  $F_\nu \sim \nu^{0.6}$ , indicating free-free emission from an optically thick windzone with an electron density distribution of the form of Eq. 3.6.

The emission can be divided into several parts, each with its own radiation mechanism. In the radio and FIR range the data can roughly be fitted by a  $\nu^{0.6}$  curve indicating that the emission is produced by free-free processes within the circumstellar wind, while free-bound emission dominates in the visible and UV range. On the other hand, in the near IR the emission results from thermal dust that is assumed to sit within a circumstellar disk. The aim of this chapter is therefore to determine the contribution of each emission component to the overall continuum spectrum. The contribution from the central star whose maximum of emission occurs in the ultraviolet ( $T_* \simeq 35\,000$  K) plays only a minor role for the total continuum spectrum because most of its radiation

is absorbed by foreground material (the extinction to MWC 349 is about 10 mag).

**Table 3.1:** References for the continuum emission data from MWC 349 plotted in Figure 3.1.

wavelength range		Reference
radio :	21 cm – 10 mm	(1);(2);(3);(4);(5)
mm – submm :	10 mm – 0.1 mm	(6);(7);(8);(9)
FIR – NIR :	100 $\mu$ m - 0.8 $\mu$ m	(10);(11);(12)
optical :	750 nm – 400 nm	(13);(14)

*References:* (1) Altenhoff, Strittmatter & Wendker (1981) and references therein; (2) Dreher & Welch (1983); (3) Escalante et al. (1989); (4) Olmon (1975) and references therein; (5) White & Becker (1985); (6) Altenhoff, Thum & Wendker (1994); (7) Martín–Pintado et al. (1994) and references therein; (8) Schwartz (1980); (9) Schwartz & Spencer (1977); (10) Harvey, Thronson, & Gatley (1979) and references therein; (11) Herzog, Gehrz & Hackwell (1980); (12) McGregor, Persson & Cohen (1984); (13) Kuhl (1973); (14) Lee (1970).

## 3.2 Emission from the wind zone

In an ionized gas, different radiation mechanisms can occur: (i) free–free radiation induced by scattering of electrons with protons, (ii) free–bound radiation of an electron that has been captured by a proton into an excited level  $n$  of the newly formed atom, and (iii) bound–bound radiation which takes place between two discrete states within the atom. Only the first two mechanisms are important for the continuum emission from the wind zone, whereas the third one produces line radiation at discrete frequencies which is discussed in the next chapter. Here, we will concentrate on the first two processes, i.e. free–free and free–bound emission.

For free–free radiation the emission coefficient,  $j_\nu$ , is given by

$$j_\nu = \frac{8}{3} \left( \frac{2\pi}{3} \right)^{\frac{1}{2}} \frac{Z^2 e^6}{m_e^{3/2} c^3 (kT)^{1/2}} g_{\text{ff}} N_e N_i e^{-\frac{h\nu}{kT}} \quad (3.1)$$

where  $N_e$  and  $N_i$  are the number densities of the electrons and ions, respectively,  $Z$  is the ionic charge,  $m_e$  and  $e$  are the electron mass and charge, and  $g_{\text{ff}}$  is the free–free gaunt factor. According to Kirchhoff’s law, which is valid in the case of LTE, the absorption coefficient,  $\kappa_\nu$ , is connected to the emission coefficient by

$$\kappa_\nu = \frac{j_\nu}{B_\nu}, \quad (3.2)$$

and  $B_\nu = B_\nu(T)$  is the Planck function, defined as

$$B_\nu(T) = \frac{2h\nu^3}{c^2} \frac{1}{e^{\frac{h\nu}{kT}} - 1}. \quad (3.3)$$

The combination of the three formulae (Eqs. (3.1; 3.2; 3.3)) and the fact that the resulting relation also holds for free–bound processes but with  $g_{\text{fb}}$  instead of  $g_{\text{ff}}$ , leads to the total absorption coefficient in  $\text{cm}^{-1}$

$$\kappa_\nu = \frac{4}{3} \left( \frac{2\pi}{3km_e^3} \right)^{\frac{1}{2}} \frac{Z^2 e^6}{hc\nu^3 T^{1/2}} N_e N_i \left( 1 - e^{-\frac{h\nu}{kT}} \right) (g_{\text{ff}} + g_{\text{fb}})$$

$$\simeq 3.692 \cdot 10^8 \frac{Z^2 N_e N_i}{\nu^3 T^{1/2}} \left(1 - e^{-\frac{h\nu}{kT}}\right) (g_{\text{ff}} + g_{\text{fb}}) . \quad (3.4)$$

Expressions to calculate the gaunt factors for free-free and free-bound radiation can be found in Appendix A.

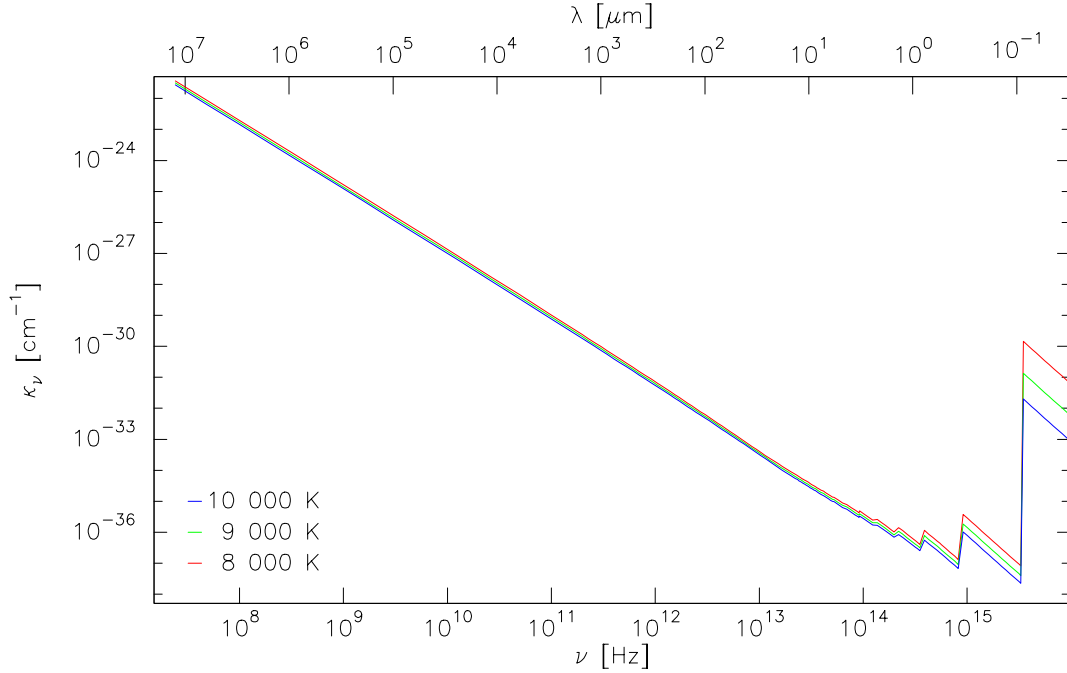


**Figure 3.2:** Absorption coefficient for free-free and free-bound emission.

The behaviour of  $\kappa_\nu$  with frequency, after inserting  $Z = 1$  and  $N_i = N_e = 1 \text{ cm}^{-3}$ , is shown in Figure 3.2. In the radio range, where  $h\nu \ll kT$  and the free-bound gaunt factors are negligible, the curves can be approximated by

$$\kappa_\nu \simeq 1.772 \cdot 10^{-2} \frac{g_{\text{ff}}}{\nu^2 T^{3/2}} . \quad (3.5)$$

As  $g_{\text{ff}}$  is only weakly dependent on frequency, the absorption coefficient varies approximately as  $\nu^{-2}$ , i.e. it increases with wavelength as  $\lambda^2$ .

The spectral index of the continuum emission in the radio and far IR range of  $\sim 0.6$  (see Figure 3.1) indicates free-free emission from an optically thick wind zone in which the electron density distribution is of the form

$$N_e(r) = N_0 \left( \frac{r}{R_0} \right)^{-2} . \quad (3.6)$$

Such a wind zone can be spherical (Olson 1975; Panagia & Felli 1975), where the factor  $N_0 R_0^2$  is constant, or non-spherical in nature (Schmid-Burgk 1982), where it depends on geometry:  $N_0 R_0^2 = f(\theta, \phi)$ .

We describe the wind zone following Panagia & Felli (1975) with the simplest model: a sphere containing a completely ionized gas with a constant electron temperature and an electron density distribution given by Eq. (3.6). Figure 3.3 illustrates the frame of reference used. Here,  $\zeta$  means the distance of a line parallel to the  $z$  axis which passes through the center of the star, and  $s$  is the linear coordinate along that line, with origin at the intersection with the  $x - y$  plane.

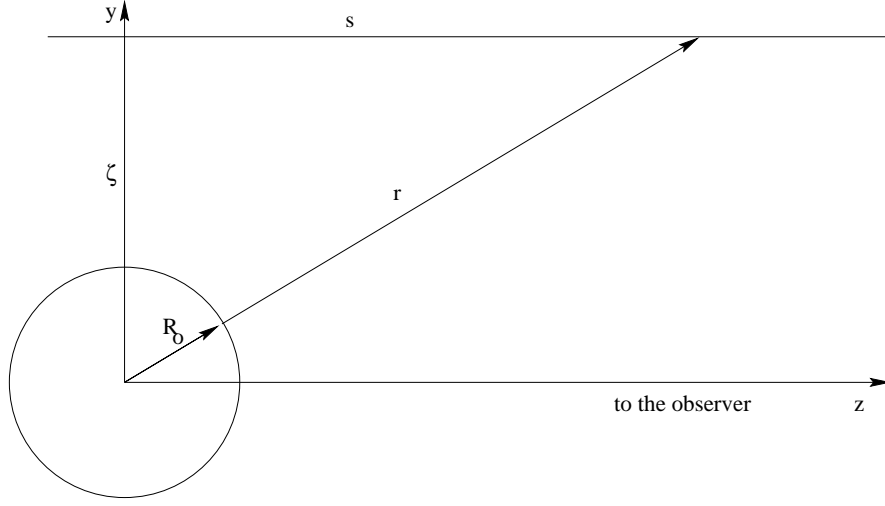


**Figure 3.3:** Frame of reference used for the calculations. The  $x$ -axis is perpendicular to the drawing-plane.

To suppress errors in determining the turn-over frequency, i.e. the frequency at which the spectrum turns from optically thick to optically thin emission, we also permit free-bound processes in the first instance.

We use a simple radiation transfer equation to calculate the intensity

$$I_\nu = B_\nu(T) \left(1 - e^{-\tau(\zeta)}\right), \quad (3.7)$$

where  $B_\nu(T)$  is a constant. The total emission is obtained by integrating the intensity along the line of sight over the entire wind zone

$$E_\nu = 4\pi \int_0^{\zeta=R_{\max}} B_\nu(T) \left(1 - e^{-\tau(\zeta)}\right) 2\pi\zeta d\zeta. \quad (3.8)$$

The factor  $4\pi$  thereby accounts for the isotropy of the emission. To finally end up with the observed flux density, the total emission is divided by  $4\pi d^2$  where  $d$  is the distance of the star

$$F_\nu = \frac{E_\nu}{4\pi d^2} = \frac{2\pi}{d^2} \int_0^{\zeta=R_{\max}} B_\nu(T) \left(1 - e^{-\tau(\zeta)}\right) \zeta d\zeta. \quad (3.9)$$

We will keep the outer radius of the wind zone,  $R_{\max}$ , as a free parameter. The optical depth along each line of sight,  $\tau(\zeta)$ , can be obtained from

$$\tau(\zeta) = 2 \int_0^{s_{\max}} \kappa_\nu(s) ds, \quad \zeta \geq R_0 \quad (3.10)$$

$$\tau(\zeta) = \int_{s_{\min}}^{s_{\max}} \kappa_\nu(s) ds, \quad \zeta < R_0 \quad (3.11)$$

with  $s_{\min} = \sqrt{R_0^2 - \zeta^2}$ ,  $s_{\max} = \sqrt{R_{\max}^2 - \zeta^2}$ , and the absorption coefficient  $\kappa_\nu$  (see Eq. (3.4)).

The calculation of free-free and free-bound emission from the spherical wind zone is performed from an inner radius,  $R_0$ , to an outer radius,  $R_{\max}$ . By assuming that  $Z \simeq 1$  and  $N_i(s) \simeq N_e(s)$ ,



whereby the latter is given by Eq. (3.6) with  $r = \sqrt{s^2 + \zeta^2}$  according to Figure 3.3, we can calculate the optical depth as a function of  $\zeta$ . With

$$\kappa_\nu(s) = k_\nu \cdot \frac{1}{(s^2 + \zeta^2)^2} \quad (3.12)$$

where

$$k_\nu = 3.692 \cdot 10^8 \frac{(N_0 R_0^2)^2}{\nu^3 T^{1/2}} (1 - e^{-h\nu/kT}) (g_{\text{ff}} + g_{\text{fb}}) \quad (3.13)$$

we find

$$\tau(\zeta) = \begin{cases} \frac{k_\nu}{3} \left[ \frac{1}{R_0^3} - \frac{1}{R_{\text{max}}^3} \right] & ; \quad \zeta = 0 \\ \frac{k_\nu}{2\zeta^2} \left[ \left( \frac{s_{\text{max}}}{R_{\text{max}}^2} - \frac{s_{\text{min}}}{R_0^2} \right) + \frac{1}{\zeta} \left( \arctan \frac{s_{\text{max}}}{\zeta} - \arctan \frac{s_{\text{min}}}{\zeta} \right) \right] & ; \quad 0 < \zeta < R_0 \\ \frac{k_\nu}{\zeta^2} \left[ \frac{s_{\text{max}}}{R_{\text{max}}^2} + \frac{1}{\zeta} \arctan \frac{s_{\text{max}}}{\zeta} \right] & ; \quad R_0 < \zeta < R_{\text{max}} \end{cases}$$

The factor  $N_0 R_0^2$  and the inner radius  $R_0$  are determined by the stellar parameters of MWC 349:

For a star with a stationary spherically symmetric wind, the mass loss rate,  $\dot{M}$ , is related to the density,  $\rho$ , and the velocity,  $v$ , at any point in the wind via the equation of mass continuity

$$\dot{M} = 4\pi r^2 \rho(r) v(r). \quad (3.14)$$

This leads to an electron density distribution of the form

$$N_e(r) = \frac{\dot{M}}{4\pi r^2 v \mu m_H} = N_0 R_0^2 r^{-2} \quad (3.15)$$

with

$$N_0 R_0^2 = \frac{\dot{M}}{4\pi v \mu m_H} \quad (3.16)$$

where  $\mu$  is the mean atomic weight. Inserting the known wind velocity of  $\sim 50$  km/s and the mass loss rate of  $1.2 \cdot 10^{-5} \text{ M}_\odot \text{ yr}^{-1}$  for MWC 349 we get  $N_0 R_0^2 = 6.48 \cdot 10^{36} \text{ cm}^{-1}$  which is in good agreement with the value of  $8 \cdot 10^{36} \text{ cm}^{-1}$  derived by Dreher & Welch (1983) and corrected for the distance of 1.2 kpc. With this value the electron density distribution within the wind zone becomes

$$N_e(r) = 2.9 \cdot 10^{10} \left( \frac{r}{1 \text{ AU}} \right)^{-2} \text{ cm}^{-3}. \quad (3.17)$$

As the inner radius of the wind zone,  $R_0$ , we choose the stellar radius of MWC 349 which is about  $3.3 \cdot 10^{11} \text{ cm} \simeq 4.7 R_\odot$  in the case of a main sequence star. Since MWC 349 is not on the main sequence its radius should be larger. For example, in the case of MWC 349 being a supergiant star, its radius could of course be more than 100 times larger (e.g. de Vaucouleurs 1970).

The emission resulting from such a spherical wind zone is shown in Figure 3.4. The calculations cover the complete wavelength range from the radio to the UV, and the influences of the electron temperature  $T_e$ , the inner radius of the wind zone  $R_0$ , the interstellar visual extinction  $A_V$ , and the outer radius of the wind zone  $R_{\text{max}}$  are presented.

The calculated spectra resemble for electron temperatures that vary between 8 000 and 10 000 K (1). The small deviations in the visible and UV result from the temperature dependence of the gaunt factor of free-bound emission,  $g_{\text{fb}}$ , but a clear temperature determination with the help of these curves is hardly possible. The second panel (2) shows the changes in the spectrum that can be

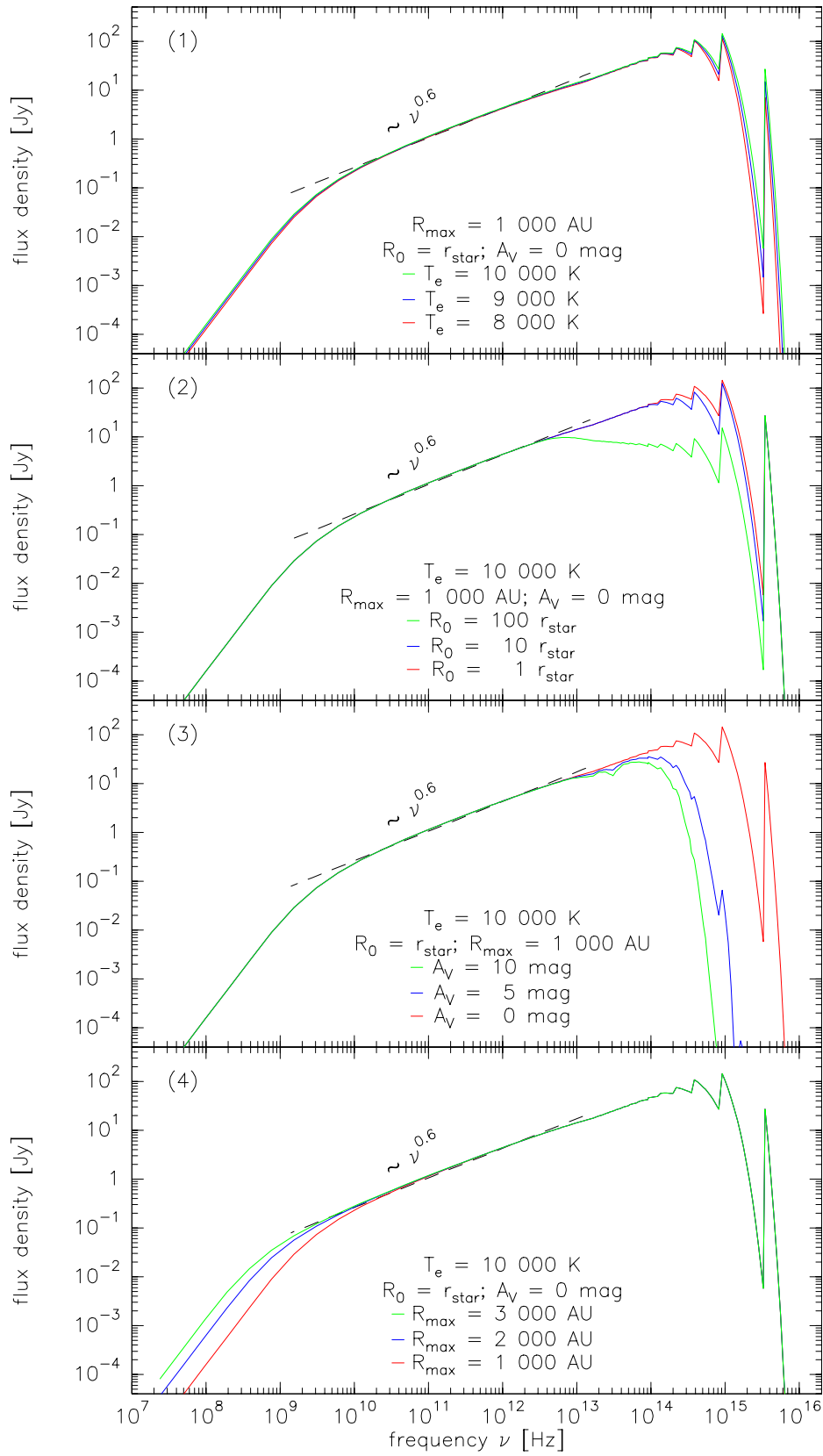


**Figure 3.4:** Synthetic spectra of free-free and free-bound emission from a spherical wind zone with a radial electron density distribution  $N_e(r) \sim r^{-2}$ . Shown are the influence of electron temperature (1), inner radius (2), interstellar visual extinction (3), and outer radius (4). In all panels the  $\nu^{0.6}$  fit is included (dashed line).

expected when the real stellar radius of MWC 349 is taken instead of the lower limit main sequence value. Then, with larger  $R_0$  the infrared emission becomes optically thin.

The existence of a foreground extinction strongly influences the high frequency part of the spectrum (3). It causes an exponential decrease in intensity

$$I = I_0 e^{-\tau_{\text{ISM}}} = I_0 10^{-0.4 A} \quad (3.18)$$

where  $\tau_{\text{ISM}}$  is the optical depth caused by the extinction  $A$  of the interstellar material and can be calculated for all wavelengths according to

$$\tau_{\lambda}^{\text{ISM}} = 0.4 \cdot \ln(10) \cdot A_{\lambda} = 0.4 \cdot \ln(10) \cdot A_V \frac{A_{\lambda}}{A_V}. \quad (3.19)$$

The ratio  $A_{\lambda}/A_V$  follows from the standard interstellar extinction curve (see e.g. Mathis 1990). Consequently, with increasing visual extinction the flux density in the visual and UV spectral range drops by several orders of magnitude whereas radiation emitted in the radio range does not suffer from the interstellar extinction. The emission from this latter part depends, however, strongly on the outer radius of the wind zone (4). Here, with decreasing frequency the spectral index turns from 0.6 to 2, and this turn-over happens at lower frequency the larger the outer radius becomes.

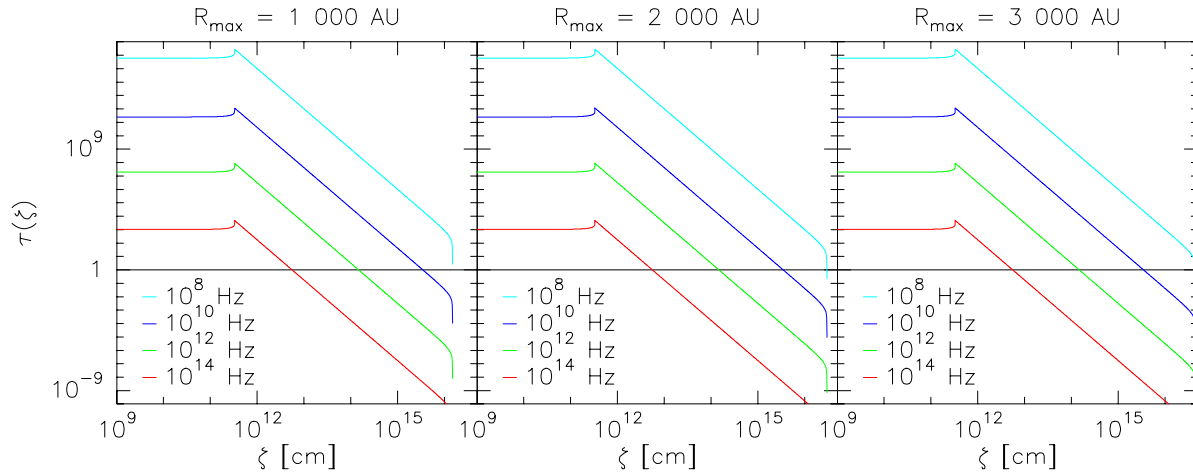


**Figure 3.5:** Optical depth as a function of radial distance from the central star for different frequencies. The lower the frequency, the further out the emission becomes optically thin. The frequency where the emission stays optically thick throughout the wind zone, leading to the spectral index of 2, becomes smaller with increasing outer radius.

To understand this behaviour we calculated the optical depth along the line of sight as a function of the radial distance parameter  $\zeta$  for wind zones of different sizes (Figure 3.5). As shown above, the absorption coefficient in the radio range is nearly proportional to  $\nu^{-2}$  (Equation 3.5; Figure 3.2). Therefore,  $\tau_{\nu}$  along a line of sight into the wind at radial distance  $\zeta$  increases to longer wavelengths as  $\lambda^2$ , and this wavelength dependence of the optical depth causes the star to appear enlarged when it is observed at lower frequencies (higher wavelengths; see Figure 3.6). If the frequency is high enough ( $\geq 10^{11}$  Hz) the total emission is composed of optically thick as well as optically thin contributions, and this mixture causes the emission to fit into the  $\nu^{0.6}$  curve. As the optical depth increases with lower frequency at a fixed  $\zeta$ , there exists a limiting frequency below which the radiation produced within a wind zone of well defined outer radius can no more contain contributions of optically thin emission so that the wind zone radiates at these frequencies like

a blackbody. Consequently, the spectral index in this frequency range becomes 2. The limiting frequency thereby depends on the size of the wind zone; it decreases with increasing radius. In the continuum data of MWC 349 there is no turn over of the spectral index (see Figure 3.1) indicating that the wind zone must have a radius of at least  $R_{\text{max}} \geq 3\,000$  AU.

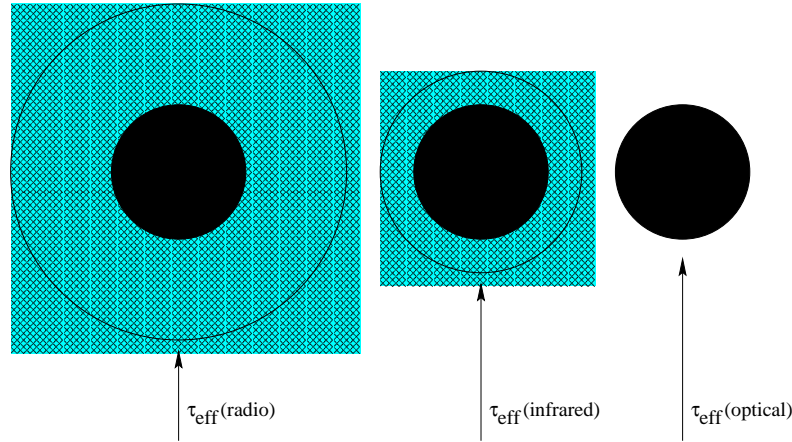


**Figure 3.6:** Sketch of the effective radius of the star that increases with the observing wavelength.

We now turn to the determination of the effective optical depth of the extended wind zone around MWC 349. For this, the effective radius  $r_{\text{eff}}$  must be calculated which is defined as the distance from the star within which approximately half of the emission at frequency  $\nu$  is produced. We computed the emission originating in a wind zone with growing radius  $\zeta$ . The results can be found for different frequencies in the upper panels of the four plots in Figure 3.7. The lower panels (as in Figure 3.5) show the decrease in optical depth with increasing wind radius. At the effective radius, when the flux density has reached half of its maximum value, we can read off the effective optical depth. We find, that for all frequencies  $\tau_{\text{eff}} \simeq 1/3$  which is only half the value compared to the case of a plane parallel atmosphere where  $\tau_{\text{eff}} = 2/3$ .

The sequence of the plots in Figure 3.7 shows clearly that the effective radius for decreasing frequency is reached further away from the star. This behaviour can also be seen in Figure 3.8 where  $r_{\text{eff}}$  is shown as a function of frequency. For a well defined outer radius, the emission at larger wavelengths can therefore no more reach its maximum value (given as the value for an infinite wind zone) leading also to a reduced flux in the radio range of the model calculations.

From the curve in Figure 3.8 we can additionally conclude that in the radio and far IR range the effective radius increases with wavelength ( $r_{\text{eff}} \sim \nu^{-2}$ ) which was already demonstrated in the sketch of Figure 3.6 above.

Before we can finish the discussion of the free-free and free-bound continuum emission we still have to determine the electron temperature. As we are dealing with a rather narrow temperature range, the spectral flux density distribution presented in Figure 3.4 (1) does not allow to derive the electron temperature. We therefore try to compare our model calculations performed for a spherical wind zone with the 6 cm radio continuum map taken by Cohen et al. (1985) whose contour lines look to a certain extent circular (see the left panel of Figure 3.9).

For reference we take the 10% and the 2% contour levels. To prevent possible deformations of the wind zone caused by the companion MWC 349 B (marked with a black dot) which is located west of the main component MWC 349 A we are interested in, we choose the direction east of the central star to read off the angular distance. A probable influence of the companion star might be the arc like structure perpendicular to the line connecting both stars. This arc is interpreted by the authors as the shock front of the two colliding wind zones. In addition, the contour lines

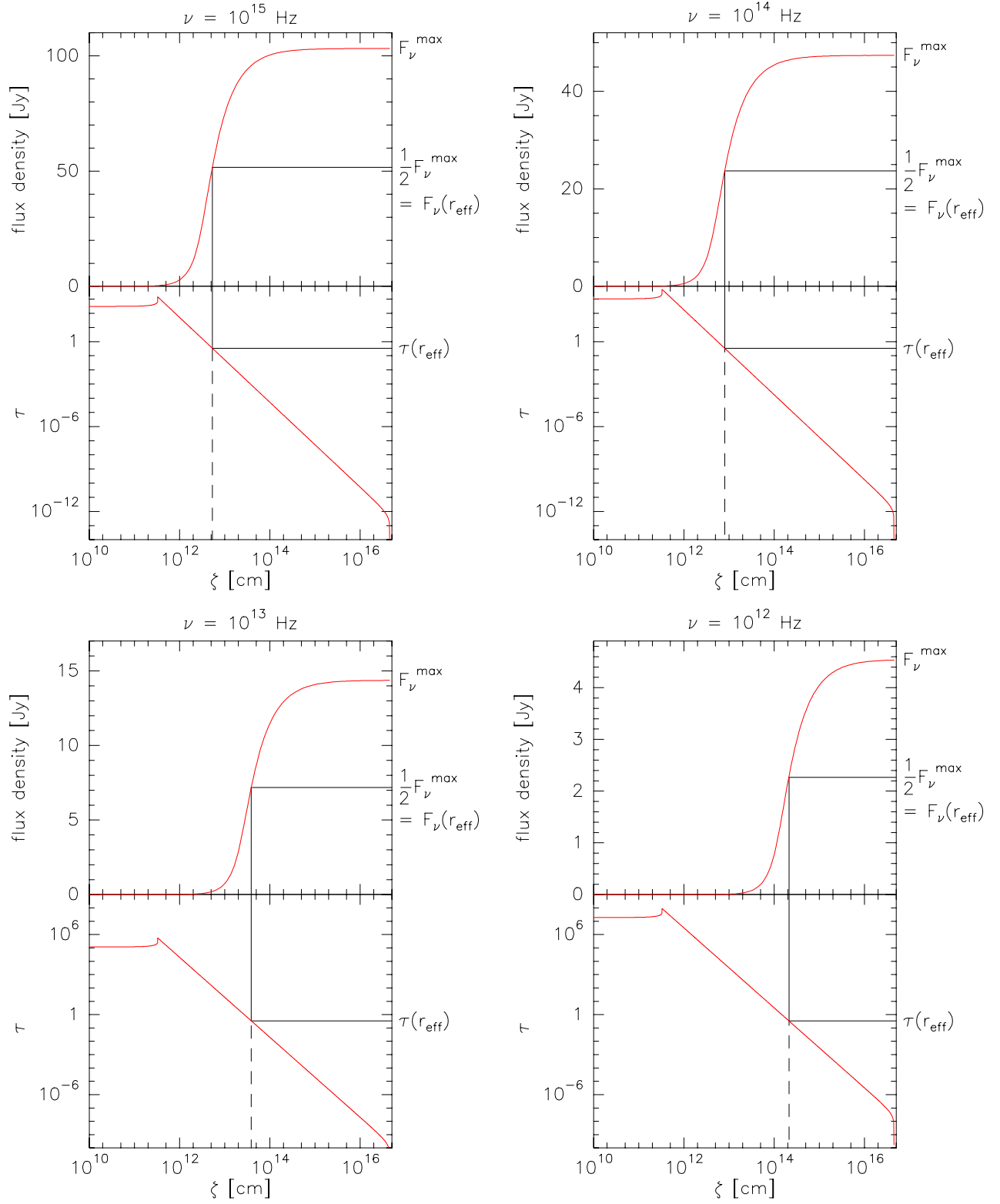


**Figure 3.7:** Determination of the effective optical depth. Each upper panel shows the flux density calculated within a wind zone of radius  $\zeta$ . The effective radius, where the emission has reached half of its maximum value, determines the effective optical depth which in all cases tends to  $1/3$ .

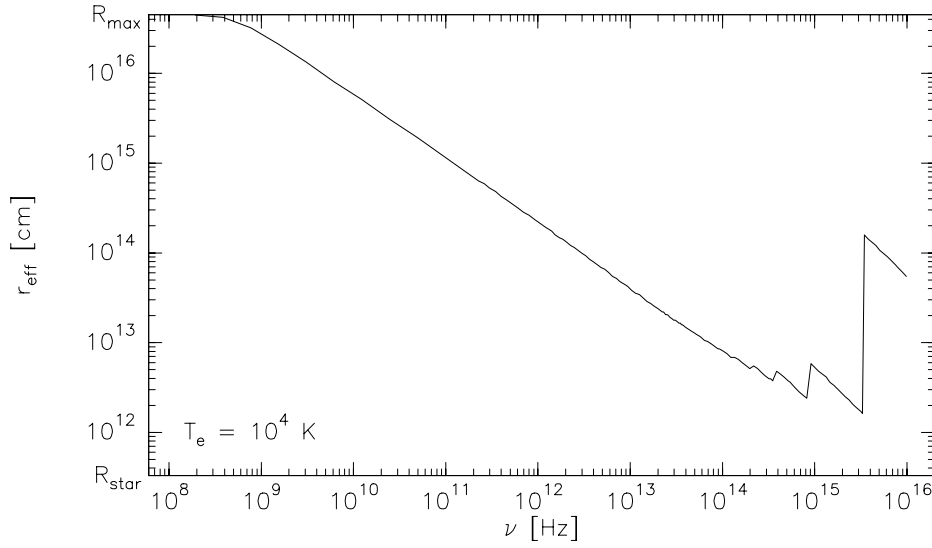


**Figure 3.8:** Calculated effective radius in the wind zone of MWC 349.

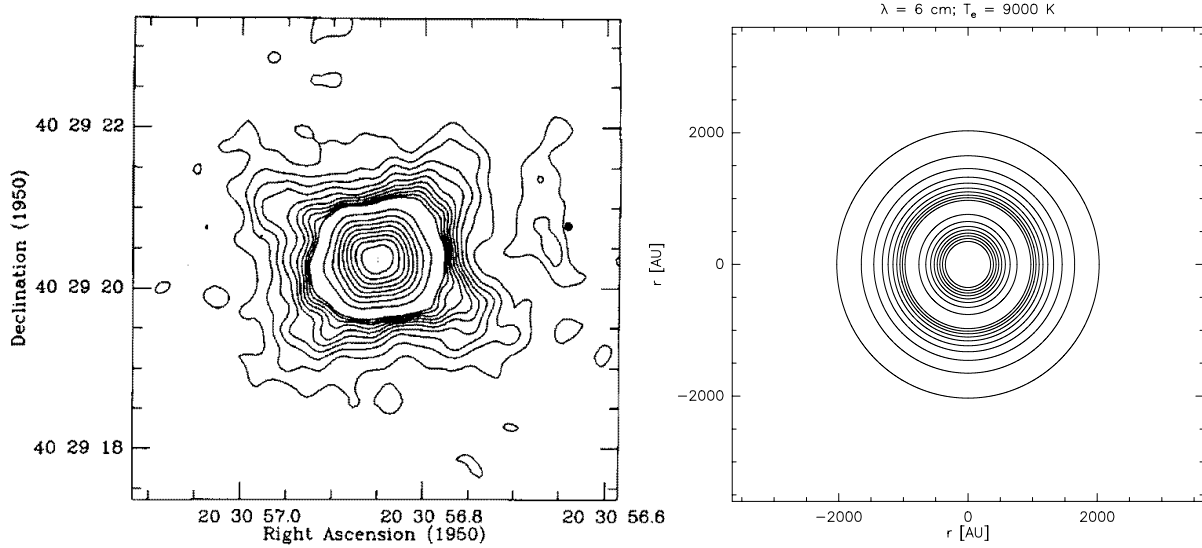


**Figure 3.9:** *Left panel:* The 6 cm radio map taken from Cohen et al. (1985). *Right panel:* The calculated 6 cm radio contour lines. Contours are in both cases at 1, 2, ..., 9, 10, 20, ..., 80, 90% of the peak flux.

west of the main component seem to be somewhat compressed which also speaks in favour of a disturbed wind. The angular distance of the contour lines is then converted into a linear distance, i.e. a radius, and listed in Table 3.2. The large errors result from taking into account the deviation from the hypothetical case of circular contour lines.

The model contour lines were calculated for electron temperatures between 8 000 and 10 000 K and the radii derived for the 10% and the 2% contour levels are also given in Table 3.2. The best agreement between the observations and the model is achieved for  $T_e \simeq 9\,000$  K. This electron temperature coincides quit well with the value of  $8\,700 \pm 300$  K derived by Cohen et al. (1985) and we plotted the model contour lines for comparison with the observational data in Figure 3.9.

Finally, we can compute the emission spectrum from the wind zone around MWC 349. The

**Table 3.2:** Radii of the 10% and the 2% contour levels at  $\lambda = 6$  cm. The second column gives the radii derived from the radio map of Cohen et al.; columns 3 to 5 contain the calculated ones for different electron temperatures.

flux in % of peak flux	$r_{\text{map}}$ [AU]	$r_{\text{model}}$ [AU] ( $T_e = 8\,000$ K)	$r_{\text{model}}$ [AU] ( $T_e = 9\,000$ K)	$r_{\text{model}}$ [AU] ( $T_e = 10\,000$ K)
10	$950 \pm 50$	1030	975	927
2	$1630 \pm 50$	1760	1650	1575

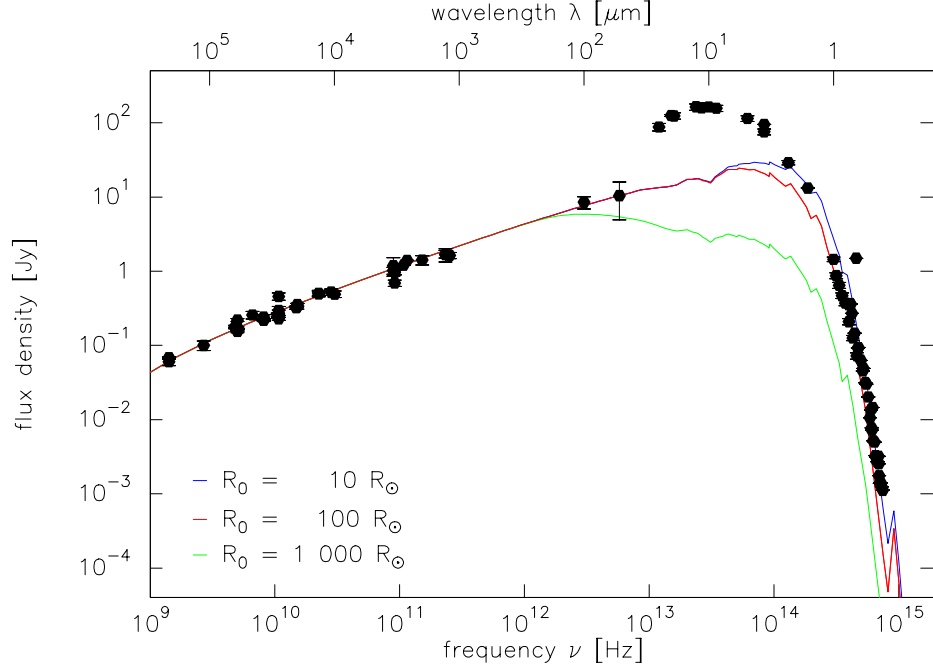


**Figure 3.10:** Free-free and free-bound emission originating in the wind zone around MWC 349 overlaid on the observations. The model parameters used are summarized in Table 3.3.

	$T_e$ [K]	$R_0$ [ $R_\odot$ ]	$N_e(R_0)$ [ $\text{cm}^{-3}$ ]	$R_{\text{max}}$ [AU]	$A_V^{\text{ISM}}$ [mag]
green curve	9 000	1 000	$1.34 \cdot 10^9$	3 000	8
red curve	9 000	100	$1.34 \cdot 10^{11}$	3 000	8
blue curve	9 000	10	$1.34 \cdot 10^{13}$	3 000	8

**Table 3.3:** Parameters for the free-free and free-bound emission from a spherical wind zone around MWC 349 presented in Figure 3.10.

parameters used are summarized in Table 3.3 and the continuum emission is plotted together with the observed data points in Figure 3.10. From these spectra we can conclude that the inner radius of the wind zone must be in the order of  $\sim 100 R_\odot$  to account for the visible and UV part of the data. This radius is about 20 times larger than in the case of a main sequence star and coincides with typical values of supergiant stars (see de Vaucouleurs 1970).

Although the wind zone around MWC 349 looks clearly bipolar at 2 cm (see White & Becker

1985), our simple spherical model can impart a rough impression of the physics of free–free and free–bound emission, and the continuum data in the wavelength ranges belonging to these processes can successfully be reproduced.

### 3.3 Emission from the dust disk

The free–free and free–bound processes cannot be responsible for the strong IR emission (see Figure 3.10). In this wavelength range, circumstellar dust is a good candidate for the so called IR excess. NIR observations using speckle interferometry could resolve a disk like structure of dust emission lying in east–west direction and seen nearly edge on (Leinert 1986; Mariotti et al. 1983). The inclination angle of the disk towards the line of sight was determined to  $15^\circ \pm 5^\circ$  (Rodríguez & Bastian 1994). In this section, the emission from this inclined dust disk is modeled.

The dust is assumed to consist of a mixture of carbon grains and silicates following a MRN grain size distribution, i.e.  $n(a) \sim a^{-3.5}$  (Mathis, Rumpl & Nordsieck 1977). The radius  $a$  of the spherical grains ranges in our model from  $7.5 \cdot 10^{-3} \mu\text{m}$  to about  $1 \mu\text{m}$ .

The first step is to determine the inner edge of the dust disk. Let  $r_{\text{evap}}$  denote the radial distance from the star at which an isolated dust grain reaches its evaporation temperature,  $T_{\text{evap}}$ , which is about 2000 K for carbon–rich grains and about 1500 K for silicate grains (Salpeter 1974).

If we assume that the absorption efficiency  $Q_\nu^{\text{abs}} \simeq 1$  with respect to absorption of photons from the star of luminosity  $L_*$ ,  $r_{\text{evap}}$  is roughly given by

$$r_{\text{evap}}(a) = \frac{1}{4\pi} \sqrt{\frac{L_*}{\int_0^\infty Q_\nu^{\text{abs}}(a) \cdot B_\nu(T_{\text{evap}}) d\nu}}. \quad (3.20)$$

where  $B_\nu(T_{\text{evap}})$  is the Planck function of the dust at the evaporation temperature  $T_{\text{evap}}$ . For a mid and far infrared absorbtivity,  $Q_\nu^{\text{abs}}(a) = 10^{-23} a \nu^2$  is a reasonable approximation for both silicates and carbon spheres of radius  $a$ . Then  $r_{\text{evap}}(a) \sim \sqrt{L_*/a}$ , which means that small grains have a larger evaporation radius than large ones. Therefore, the inner edge of the dust disk will be determined by the largest grains. For the maximum size of  $\sim 1 \mu\text{m}$  we find an evaporation radius for carbon grains of  $\sim 2.9 \text{ AU}$  and for silicates of  $\sim 9.2 \text{ AU}$ .

In reality, however, the grain density is highest at the inner edge of the disk. For a correct treatment, we should also take into account the influence from neighbouring grains, because one single particle not only absorbs radiation from the central source but also from its neighbours. The real grain temperature at a fixed distance from the star is therefore higher than in the case of an isolated particle and the evaporation radius of the grains is reached further out from the star.

A correct determination of the real inner edge is very difficult because many different chemical and physical facts which we are not aware of, would have to be taken into account. In the ongoing discussion we simply take the evaporation radius derived for an isolated carbon grain (Eq. 3.20) as the inner edge of the circumstellar dust disk but keep in mind that it can only represent a lower limit.

To model the emission of the dust disk we take the surface density and temperature distribution as power laws:  $\Sigma(r) = \Sigma_0 \cdot (r/r_{\text{evap}})^{-q}$  and  $T(r) = T_0 \cdot (r/r_{\text{evap}})^{-p}$  with  $\Sigma_0$  and  $T_0$  as the surface density and temperature at the inner edge  $r_i = r_{\text{evap}}$ . So  $T_0$  is already fixed at 2000 K, whereas  $\Sigma_0$  as well as the exponents  $p, q$  are still free parameters. In addition we assume the disk to be geometrically flat.

For an observer at the distance  $D$  whose line of sight makes an angle  $i$  to the disk plane the flux at frequency  $\nu$  from the disk is

$$F_\nu = \frac{2\pi \sin i}{D^2} \int_{r_{\text{evap}}}^{r_{\text{out}}} B_\nu(T(r)) \cdot (1 - e^{-\tau_\nu}) r dr \quad (3.21)$$



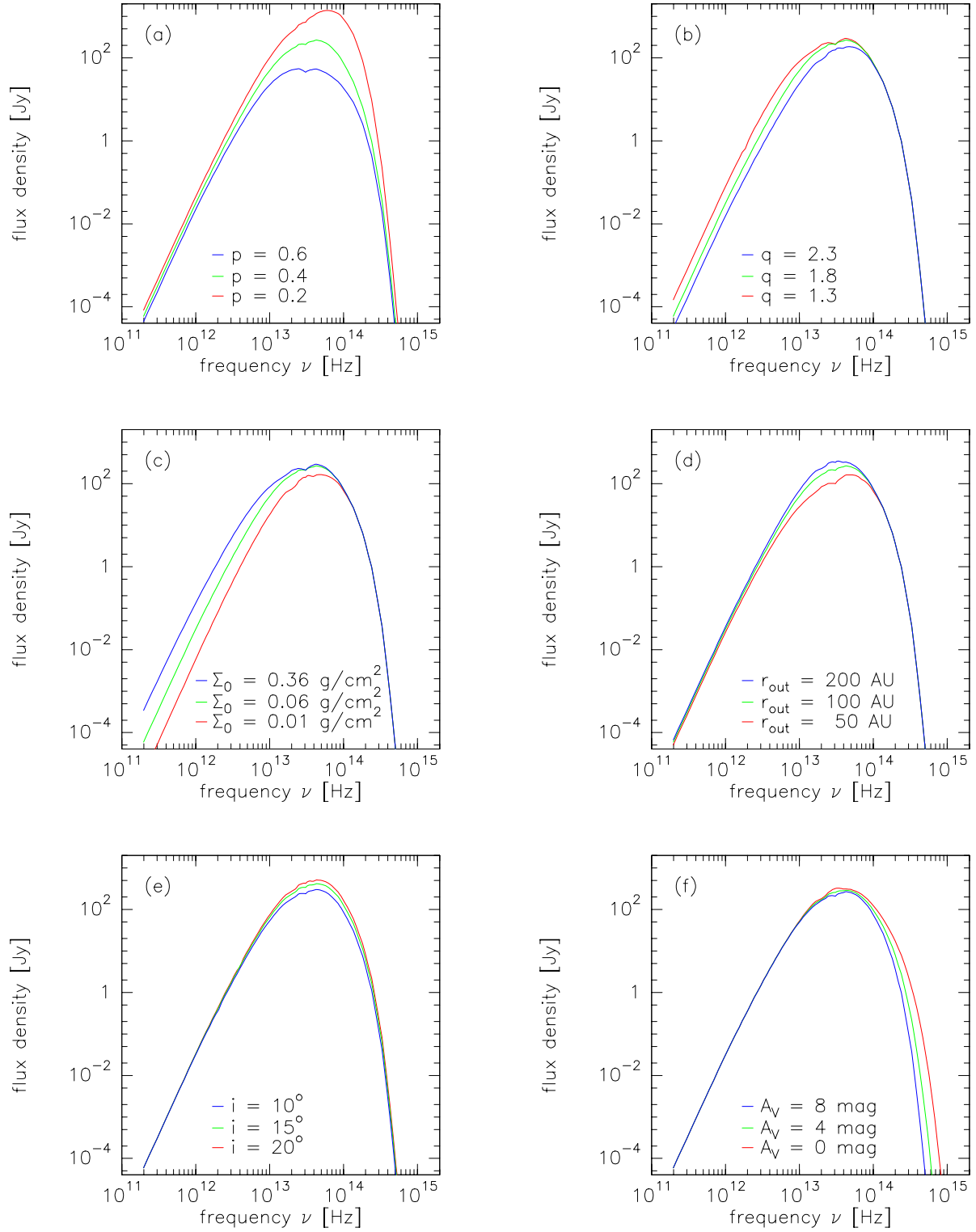


**Figure 3.11:** Calculated emission from different dust disks. To investigate the influence of the individual parameters, in each plot always only one parameter is varied whereas the others are fixed to the values given in the Tables 3.4 and 3.5. The free parameters discussed are: the exponents of the temperature and surface density distribution,  $p$  and  $q$ , respectively, the surface density at the evaporation radius,  $\Sigma_0$ , the outer radius of the disk,  $r_{\text{out}}$ , the inclination angle,  $i$ , and the interstellar visual extinction,  $A_V^{\text{ISM}}$  (see Table 3.5).

where  $r_{\text{out}}$  is the outer radius of the disk. The absorption coefficient has to be integrated over the grain size distribution

$$\kappa_\nu = \int n(a) \pi a^2 Q_\nu^{\text{abs}} da. \quad (3.22)$$

where the factor  $\pi a^2 Q_\nu^{\text{abs}}$  represents the absorption cross section of a dust grain of size  $a$ . Then the optical depth of the disk at the radial distance  $r$  from the star is given by

$$\tau_\nu = \frac{\kappa_\nu}{\sin i} \Sigma(r). \quad (3.23)$$

There are several free parameters in the calculations of the emission from the dust disk (see Table 3.5). To investigate their influence on the total emission spectrum we always vary one single parameter in each computation. The remaining ones are fixed to the values given in the Tables 3.4 and 3.5. The results are presented in Figure 3.11.

**Table 3.4:** Model parameters for the dust disk calculations shown in Figure 3.11. The stellar and disk parameters in this table are fixed for all models.

Parameters hold fixed in all models				
$L_*$	$T_{\text{eff}}$	$d$	$T_0$	$r_{\text{evap}}$
$[\text{L}_\odot]$	[K]	[kpc]	[K]	[AU]
$3 \cdot 10^4$	35 000	1.2	2 000	2.88

**Table 3.5:** Model parameters for the dust disk calculations shown in Figure 3.11. The disk parameters here are varied to investigate their influence to the overall emission spectrum. Therefore, in each computation we vary one single parameter as printed within each plot of Figure 3.11 holding the remaining ones fixed.

Parameters whose influence is investigated					
$p$	$\Sigma_0$	$q$	$r_{\text{out}}$	$i$	$A_V^{\text{ISM}}$
	$[\text{g cm}^{-2}]$		[AU]	[°]	[mag]
0.4	0.06	1.8	100	10	8

The emission is very sensitive to the temperature distribution along the disk radius (a). The faster the decrease in temperature, the lower becomes the total emission, especially in the IR part of the spectrum. Additional parameters that also play a role in the IR range are the inclination angle (e), that results only in small variations within the spectrum for the angles choosen, and the outer radius of the dust disk (d). The latter mainly determines the mid IR part where the emission decreases with smaller disk sizes. In the far IR the surface density distribution becomes important. For a high surface density at the inner edge of the disk (c) as well as for a flat radial distribution (b), the emission in the FIR and submm range increases by orders of magnitude, which leads to a broadening of the total emission shape to longer wavelengths. On the opposite site of the spectrum, i.e. in the visible range, only the interstellar visual extinction (f) causes the emission to decrease (as discussed in the previous section).

Our best fit of the continuum emission from the dust disk around MWC 349 is shown by the dashed line in Fig. 3.12. The parameters used are displayed in Table 3.6. The dotted line shows the contribution of the central star of luminosity  $3 \cdot 10^4 \text{ L}_\odot$  and effective temperature  $3.5 \cdot 10^4 \text{ K}$ . To

calculate the flux density of the star we made the assumption that the star exhibits an additional extinction caused by the dense circumstellar disk which is orientated nearly edge on so that the flux from the star has to pass through the disk. This circumstellar extinction has been estimated by Cohen et al. (1985) to be in the order of 2 mag. Finally we added the contribution from the wind zone for which we choose the fit for  $R_0 \simeq 100 R_\odot$ . The resulting total emission that fits the data quite well is drawn as the solid line in Fig. 3.12. Using the standard conversion factor for dust, i.e.  $\Sigma_{\text{dust}} : \Sigma_{\text{H}} \simeq 10^{-2}$ , we find for the dust and the gas masses of the disk  $M_{\text{dust}} \simeq 1.65 \cdot 10^{-6} M_\odot$  and  $M_{\text{gas}} \simeq 1.65 \cdot 10^{-4} M_\odot$ , respectively.

**Table 3.6:** Parameters for the emission from the dust disk around MWC 349.

$r_{\text{evap}}$	$r_{\text{out}}$	$T_0$	$p$	$\Sigma_0$	$q$	$i$	$A_V^{\text{ISM}}$
[AU]	[AU]	[K]		[g cm $^{-2}$ ]		[ $^\circ$ ]	[mag]
2.88	100	2000	0.44	0.06	1.8	10	8

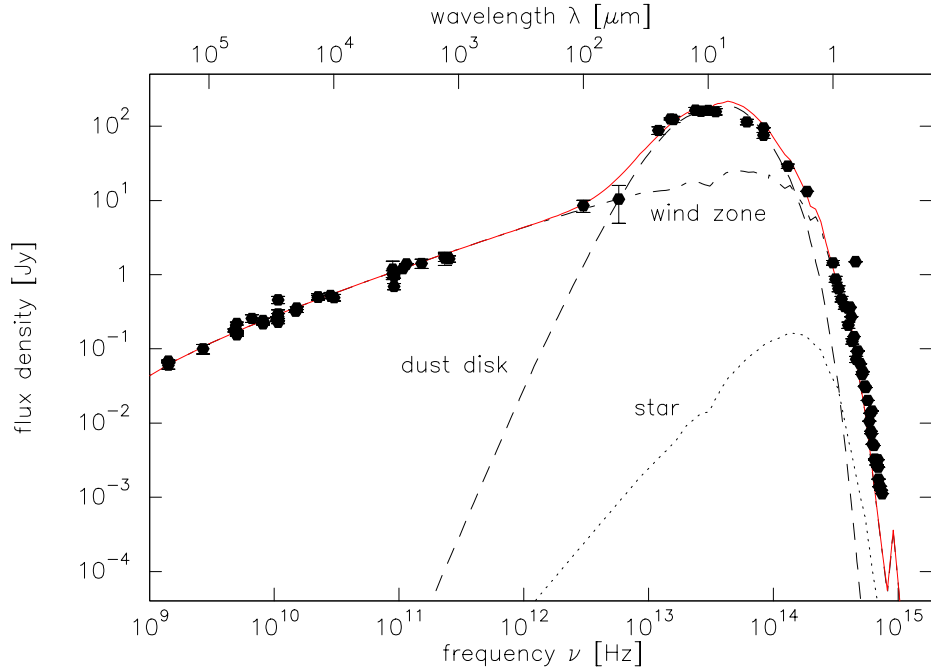


**Figure 3.12:** Best fit (solid line) to the continuum emission (black dots). Also shown are the individual contributions from the dust disk (dashed line), from the central star (dotted line), and from the free-free and free-bound emission of the wind zone (dashed-dotted line). The parameters for the disk are displayed in Table 3.6.

The model calculation indicates a temperature index of  $\sim 0.44$ . This is not an unusual value, since also most of the disks around T Tauri stars are found to have a temperature index of  $\sim 0.5$  (Adams, Lada & Shu 1988; Beckwith et al. 1990). The disk radius of  $\sim 100$  AU seems to be in a reasonable range, for it is in the same order as the value derived by Leinert (1986). Finally, we can conclude that we are *not* dealing with a *geometrically flat accretion disk*. If that would be the case, the exponent of the temperature distribution should be  $q = 3/4$  (see e.g. Pringle 1981).

With the help of the continuum emission we are now in the position to get the pure line emission spectrum by subtracting the continuum from the high resolution spectrum (Fig. 2.6). The result

is presented in Figure 3.13. This spectrum which mainly consists of the CO first overtone bands and the Pfund lines of the hydrogen atom is now the basis for the further investigations.

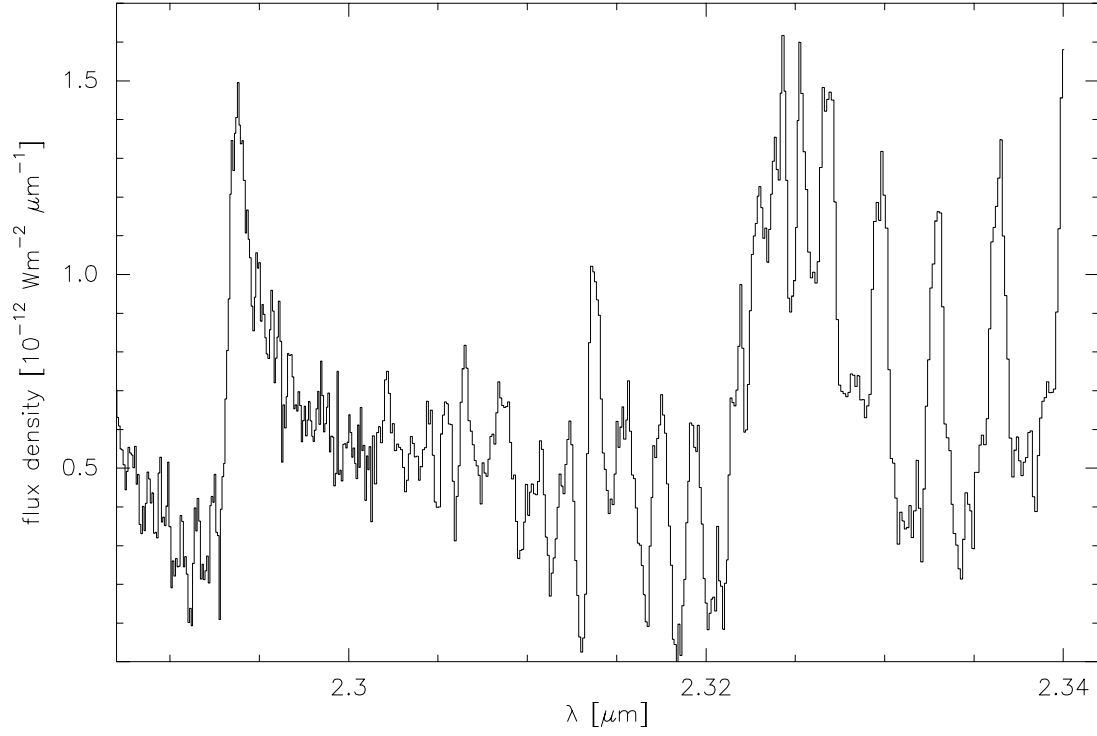


**Figure 3.13:** NIR emission line spectrum after subtraction of the continuum emission. It consists mainly of the CO first overtone bands and the Pfund lines of the hydrogen atom.

# Chapter 4

## Hydrogen recombination lines

The environment of MWC 349 is famous for its numerous, very prominent hydrogen recombination lines (HRLs,  $n \rightarrow n'$ ;  $n - n' = 1, 2, \dots, \infty$ ) which all appear in emission. The most prominent ones observed up to now (Andrillat & Swings 1976; Thompson & Reed 1976; Allen & Swings 1976; Andrillat, Ciatti & Swings 1982; McGregor, Persson & Cohen 1984; Hamann & Simon 1986; 1988; Kelly, Rieke & Campbell 1994; Andrillat, Jaschek & Jaschek 1996) belong to the first six series ( $n' = 1 \dots 6$ ), which are called Lyman, Balmer, Paschen, Brackett, Pfund, and Humphreys.

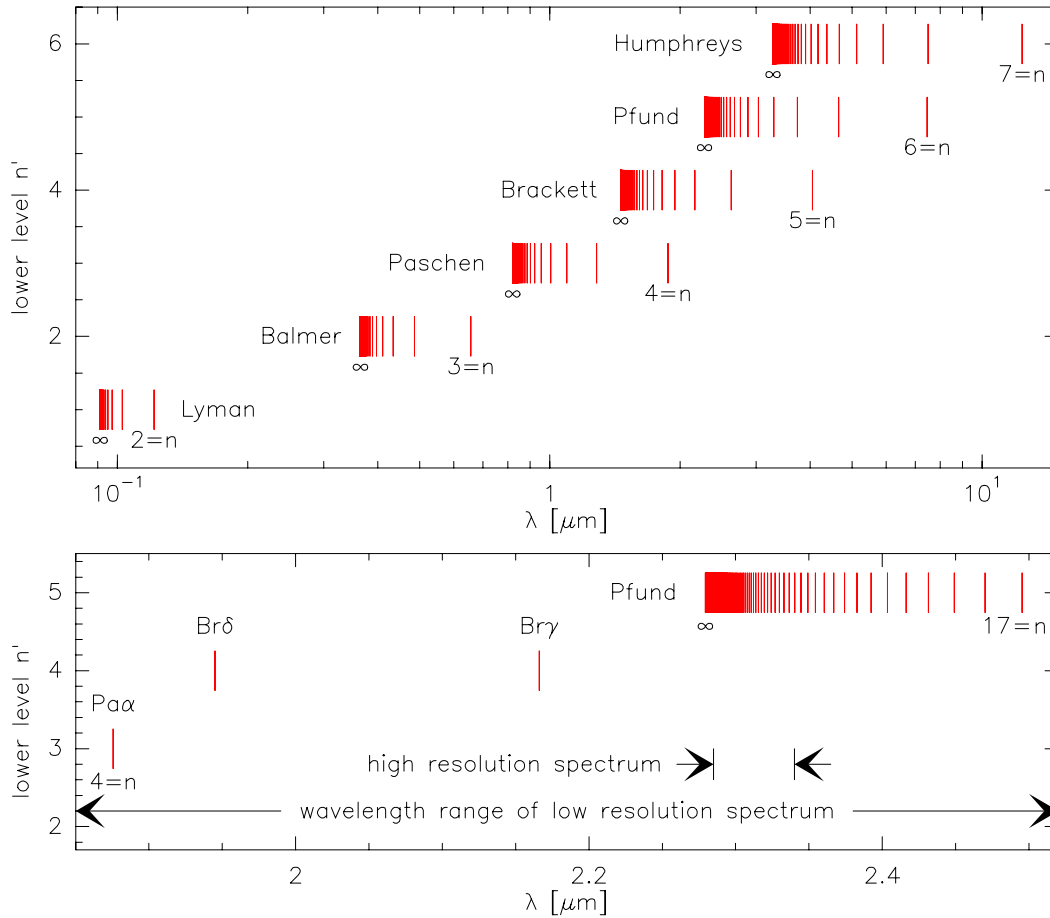


**Figure 4.1:** *Upper panel:* Wavelengths of the members of the hydrogen series. *Lower panel:* Transitions that lie in our low and high resolution spectra.

In the upper panel of Figure 4.1 we indicate the wavelengths of transitions within these series, and the lower panel covers the wavelength range of our low resolution NIR spectrum and shows which HRLs are expected to appear in the spectrum. While the high resolution spectrum contains transitions solely from the Pfund series ( $n \rightarrow n' = 5$ , denoted as Pf(n)), there are also some additional lines from neighbouring series present in the low resolution spectrum (for comparison see Table 2.2).

The emission from several Pfund lines has also been observed before. For example, Hamann & Simon (1986) already identified some Pfund lines in their velocity-resolved infrared spectroscopy of MWC 349, but their resolution of  $\sim 20$  km/s was lower than ours, so they could only resolve lines up to Pf(34), whereas our high resolution spectrum points out the existence or the presence of some more Pfund emission lines. In order to determine the contamination of the CO bands with hydrogen recombination lines we have to take care of a detailed modeling of the Pfund line emission spectrum, which is the subject of the present chapter.

The recombination line spectrum of H I is emitted by H atoms that have been formed by captures of electrons into excited levels and that are cascading by downward radiative transitions to the ground level. The total energy emitted per  $\text{cm}^3$  per second by an assembly containing  $N_n$  atoms per  $\text{cm}^3$  in state  $n$  is, by definition

$$E_\nu = N_n A_{nn'} h \nu_{nn'}, \quad (4.1)$$

where  $A_{nn'}$  is the Einstein probability coefficient of spontaneous transition, and  $\nu_{nn'}$  is the transition frequency between the levels  $n$  and  $n'$ . Before we can continue calculating the recombination spectrum we first have to determine the level population and the Einstein coefficients.

## 4.1 Level population of recombined hydrogen atoms

Let's start with a neutral gas in local thermodynamic equilibrium (LTE) at temperature  $T$  that is composed of only one atomic species. The number density,  $N_n$ , of atoms in level  $n$  is given by the Boltzman distribution

$$\frac{N_n}{N_0} = \frac{g_n}{g_0} e^{-\chi_n/kT} \quad (4.2)$$

where  $N_0$  is the number density of atoms in the ground level 0,  $\chi_n$  is the excitation energy,  $g_n$  and  $g_0$  are the statistical weights of the corresponding levels. If we relate  $N_n$  to the total number density,  $N$ , Equation (4.2) can be written as

$$\frac{N_n}{N} = \frac{g_n e^{-\chi_n/kT}}{\sum_m g_m e^{-\chi_m/kT}} = \frac{g_n}{Q} e^{-\chi_n/kT} \quad (4.3)$$

with the partition function  $Q$  that is defined in the following way

$$Q \equiv \sum_m g_m e^{-\chi_m/kT}. \quad (4.4)$$

In the case of a partially ionized gas the ratio of the number densities of singly ionized (index 1) and neutral atoms (index 0), each of them in the corresponding ground level 0 (second index), is formulated by *Saha's Equation*

$$\frac{N_{1,0}}{N_{0,0}} N_e = \frac{g_{1,0}}{g_{0,0}} \cdot 2 \frac{(2\pi m_e kT)^{3/2}}{h^3} e^{-\chi_i/kT}. \quad (4.5)$$

Here,  $\chi_i$  means the ionization energy, and the product

$$g_{1,0} \cdot 2 \frac{(2\pi m_e kT)^{3/2}}{h^3 N_e} \quad (4.6)$$

represents the combination of (i) the statistical weight of the ionized atom in its ground level, and (ii) the statistical weight of the free electron. So we can determine the total number density of ionized and neutral atoms, i.e.  $N_1$  and  $N_0$ , using Saha's Equation (4.5) and the definition of the partition function (Eq. (4.4))

$$\begin{aligned}
N_1 &= \sum_l N_{1,l} \\
&= \sum_l \frac{N_{0,0}}{N_e} \cdot \frac{g_{1,l}}{g_{0,0}} \cdot 2 \frac{(2\pi m_e kT)^{3/2}}{h^3} e^{-\frac{\chi_i + \chi_{1,l}}{kT}} \\
&= \frac{N_{0,0}}{N_e} \cdot \frac{Q_1}{g_{0,0}} \cdot 2 \frac{(2\pi m_e kT)^{3/2}}{h^3} e^{-\chi_i/kT}
\end{aligned} \tag{4.7}$$

$$\begin{aligned}
N_0 &= \sum_n N_{0,n} \\
&= \sum_n N_{1,0} N_e \cdot \frac{g_{0,n}}{g_{1,0}} \cdot \frac{h^3}{2 (2\pi m_e kT)^{3/2}} e^{\frac{\chi_i - \chi_{0,n}}{kT}} \\
&= N_{1,0} N_e \cdot \frac{Q_0}{g_{1,0}} \cdot \frac{h^3}{2 (2\pi m_e kT)^{3/2}} e^{\chi_i/kT}
\end{aligned} \tag{4.8}$$

The ratio of these two number densities has the same form as the Saha Equation

$$\frac{N_1}{N_0} N_e = \frac{Q_1}{Q_0} \cdot 2 \frac{(2\pi m_e kT)^{3/2}}{h^3} e^{-\chi_i/kT} \tag{4.9}$$

but with the partition functions instead of the statistical weights.

Now,  $N_0$  can be derived from Equation (4.9) and identified with the total number density  $N$ . By inserting  $N$  into the Boltzmann distribution (Eq. (4.3)) and omitting the index 0 we finally end up with the level population,  $N_n$ , of the recombining neutral atoms

$$N_n = N_1 N_e \cdot \frac{g_n}{Q_1} \cdot \frac{h^3}{2 (2\pi m_e kT)^{3/2}} e^{-\frac{\chi_i - \chi_n}{kT}}, \tag{4.10}$$

or, with regard to hydrogen where  $Q_1 = 1$ ,  $N_1 = N_i$ ,  $g_n = 2n^2$ ,  $\chi_i = h \cdot Ry$ , and  $\chi_n = h \cdot Ry \left(1 - \frac{1}{n^2}\right)$  where  $Ry = 2\pi^2 m_e e^4 / h^3 \simeq 3.29 \cdot 10^{15} \text{ Hz}$  is the Rydberg constant,

$$N_n = N_i N_e \cdot n^2 \cdot \frac{h^3}{(2\pi m_e kT)^{3/2}} e^{-\frac{h \cdot Ry}{n^2 kT}}. \tag{4.11}$$

This relation of course holds only in the case of LTE.

Because of the numerous processes that take place within the circumstellar environment (for example in an H II region) the assumption of LTE condition will be met only very rarely. The most important processes affecting the level population are

- radiative capture and cascade,
- collisional excitations and de-excitations induced by electrons and protons, and
- collisional ionization and three-body recombination.

It is convenient to express  $N_n$  in terms of the dimensionless factors  $b_n$  that measure the deviation from local thermodynamic equilibrium

$$N_n = b_n N_i N_e \cdot n^2 \cdot \frac{h^3}{(2\pi m_e kT)^{3/2}} e^{-\frac{h \cdot Ry}{n^2 kT}} \tag{4.12}$$

and it follows immediately that  $b_n = 1$  in the case of LTE.

An exact calculation of the  $b_n$  factors cannot be carried out because when we insert the level population given by Equation (4.12) into the equation of statistical equilibrium, which contains all the processes listed above that populate or depopulate the level  $n$ , we end up with an infinite set of linear equations for the  $b_n$ . Many effort has been made to find an approximation method for this infinite dimensional matrix equation, at least for a small density and temperature range (see e.g. Brocklehurst 1970; Hummer & Storey 1987; Walmsley 1990). Recently, Storey & Hummer (1995) presented new and more complete computations of their earlier results. Their improved  $b_n$  factors cover a broad electron temperature and density range and have been published for hydrogenic ions with  $Z \leq 8$  in form of electronic tables.

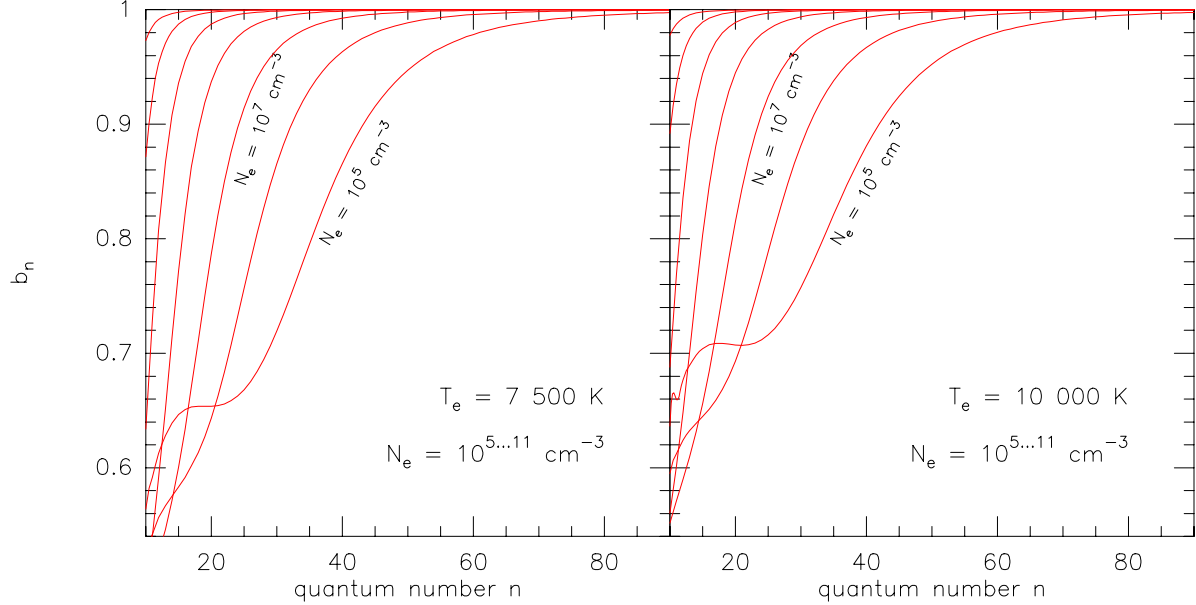


**Figure 4.2:** The curves from the left to the right represent the  $b_n$ -factors of the hydrogen atom after Storey & Hummer (1995) for a decreasing electron density and an isothermal gas of  $T_e = 7.5 \cdot 10^3 \text{ K}$  (left panel) and  $T_e = 10^4 \text{ K}$  (right panel).

For our purpose we take the  $b_n$  factors for hydrogen given by Storey & Hummer (1995) that were calculated for case B recombination theory, because this seems to be more accurate than case A for most nebulae. The classification into two categories (case A and case B) is based on the Lyman lines that are assumed to be optically thin in case A and optically thick in case B, whereas all the other recombination lines are in both cases taken as optically thin (Baker & Menzel 1938).

To demonstrate the behaviour of the  $b_n$  factors we have plotted some of them in Figure 4.2 for electron temperatures of  $T_e = 7.5 \cdot 10^3 \text{ K}$  (left panel) and  $T_e = 10^4 \text{ K}$  (right panel). The electron density in both plots ranges from  $10^5 \text{ cm}^{-3}$  to  $10^{11} \text{ cm}^{-3}$ . Even for densities as low as  $10^5 \text{ cm}^{-3}$  the values of  $b_n$  approaches 1 which means that the levels lying higher than  $n \simeq 70$  are nearly populated according to LTE conditions. The higher the electron density, the lower is the quantum number of the level at which thermalization is achieved. The general effect of a higher electron temperature results in a higher value of the  $b_n$  factor, but the temperature influences especially the low lying levels ( $n \leq 30$ ).

From the Eqs. (4.11) and (4.12) we see that as for higher quantum states  $n$  the exponential term approaches unity, the level population,  $N_n$ , increases with  $n^2$  which means that it is divergent. This can also be seen in Figure 4.3 where we displayed the level population of the recombining hydrogen atoms for different temperatures.



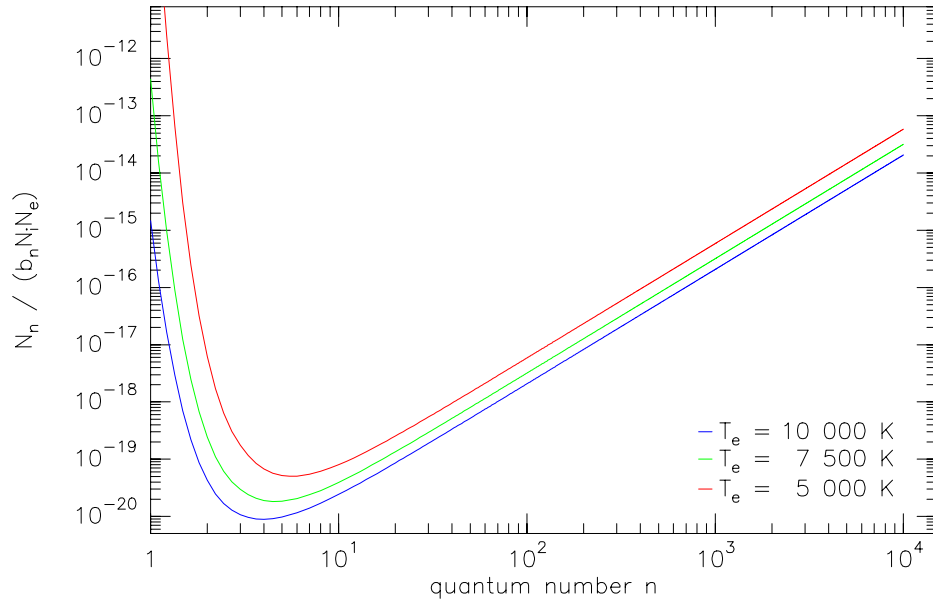


**Figure 4.3:** Divergent level population of the recombining hydrogen atoms calculated according to Eq. (4.11). The electron temperature varies between 5 000 and 10 000 K.

The problem we have to solve is, how the population of the highest levels in the hydrogen atom can be prevented. Or, by speaking the other way round: What kind of physical condition do we need to prevent the highest quantum states in the hydrogen atom to exist at all?

Here, we mention two physical effects that might play an important role in reducing the bound levels to a finite number: the Debye–shielding and the pressure ionization.

#### 4.1.1 Debye–shielding

Consider a pure electron proton plasma. For overall charge neutrality we require

$$N_i = N_e. \quad (4.13)$$

If we place for convenience one proton at the origin of our coordinate system, it attracts electrons towards itself and repels protons. In a steady state, the process will set up an electrostatic potential  $\Phi$  that satisfies Coulomb’s law:

$$\nabla^2 \Phi = -4\pi \rho_e \quad (4.14)$$

where  $\rho_e$  equals the charge–density distribution. This distribution includes the proton at the origin as well as a Boltzmann (spatial) distribution of surrounding electrons and protons:

$$\rho_e = e \delta(\vec{r}) - N_e e \cdot e^{\frac{e\Phi}{kT}} + N_i e \cdot e^{-\frac{e\Phi}{kT}}. \quad (4.15)$$

For simplicity, it is assumed that the electrons and protons have the same temperature.

The electrostatic energies  $\pm e \Phi$  are assumed to be small in comparison with  $kT$  so that the exponential functions can be expanded. When we make use of Equation (4.13) and by taking account of the spherical symmetry, Coulomb’s law can be written as

$$\frac{1}{r^2} \frac{d}{dr} \left( r^2 \frac{d\Phi}{dr} \right) = -4\pi e \delta(\vec{r}) + \frac{8\pi N_e e^2}{kT} \Phi \equiv -4\pi e \delta(\vec{r}) + L_D^{-2} \Phi. \quad (4.16)$$

The quantity  $L_D$  is called the *Debye length* and it is in our case of an electron proton plasma given by

$$L_D = \sqrt{\frac{kT}{8\pi N_e e^2}} \simeq 4.88 \cdot \sqrt{\frac{T}{N_e}}. \quad (4.17)$$

The solution of Equation (4.16) that satisfies  $\Phi \rightarrow e/r$  as  $r \rightarrow 0$ , and  $\Phi \rightarrow 0$  as  $r \rightarrow \infty$ , reads

$$\Phi = \frac{e}{r} e^{-r/L_D}. \quad (4.18)$$

From this behaviour we can conclude that the statistical attraction of electrons and repulsion of protons shield the potential of any proton, reducing the Coulomb value at large  $r$  by an exponential factor.

If we now expand the exponential in Equation (4.18) for small  $r/L_D$ , we obtain the physical picture that the potential surrounding a proton has the approximation  $\Phi \simeq e(r^{-1} - L_D^{-1})$ ; consequently, the continuum energy level of an electron behaves as if it had been lowered by a constant amount  $e^2/L_D$ . So the high-lying energy states are removed. For hydrogen,  $E_n = -h \cdot Ry/n^2 = -e^2/2a_0 n^2$  where  $a_0 \equiv \hbar^2/m_e e^2$  is the Bohr radius, and the energy of maximum possible quantum state  $n_{\max,D}$  is now fixed by the Debye length:  $E_{n_{\max,D}} = -e^2/2a_0 n_{\max,D}^2 = -e^2/L_D$ , which results in

$$n_{\max,D} = \sqrt{L_D/2a_0} \simeq 2.1472 \cdot 10^4 \left(\frac{T}{N_e}\right)^{\frac{1}{4}}. \quad (4.19)$$

For the right hand side we inserted the expression of the Debye length (Equation (4.17)). The dependence of  $n_{\max,D}$  on the electron density is shown for different temperatures in the left panel of Figure 4.4, whereas in the right panel the variation of  $n_{\max,D}$  with temperature is plotted for fixed electron densities. The electron temperature in an ionized wind zone must be near  $10^4$  K. So the weak temperature dependence of only  $T^{0.25}$  does not much affect the maximum quantum number: if the temperature is twice as much,  $n_{\max,D}$  is only  $2^{0.25} = 1.19$  times larger.

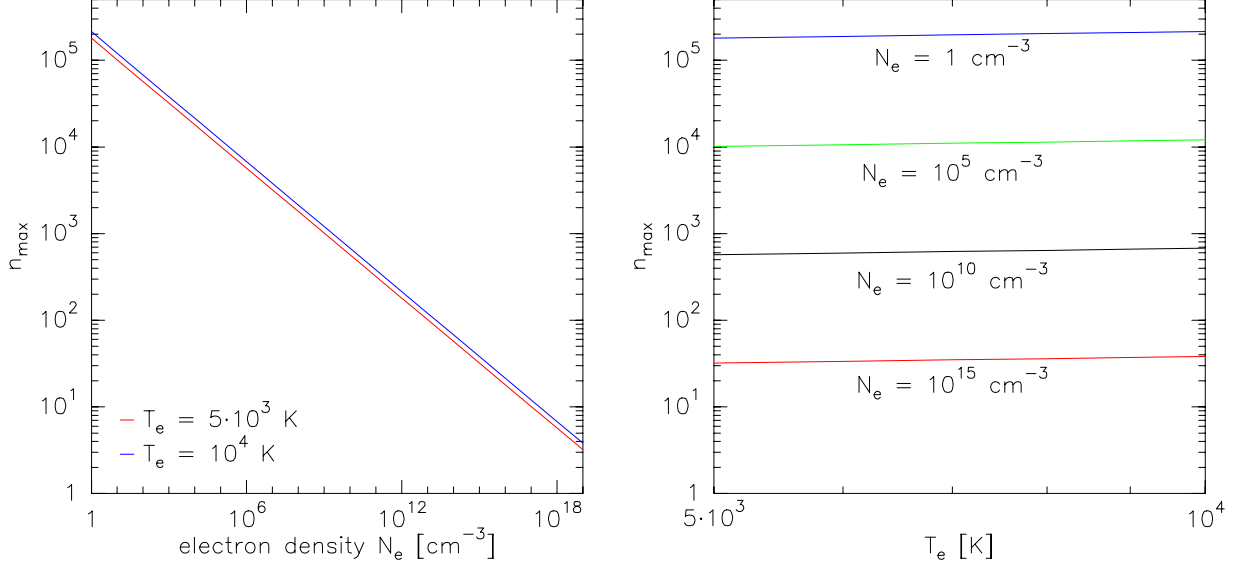


**Figure 4.4:** The number of the maximum bound quantum states of the hydrogen atom  $n_{\max,D}$  in the case of Debye-shielding. *Left panel:* The variation with electron density for a fixed electron temperature; *right panel:* The variation with electron temperature for a fixed electron density.

The electron density within the wind zone, however, can change by several orders of magnitude;  $n_{\max,D}$  is therefore strongly dependened on the local density. For example, for the electron densities

being present in the wind zone around MWC 349 of  $1.3 \cdot 10^{11} \text{ cm}^{-3}$  at  $r = 100 R_{\odot}$  and  $3.2 \cdot 10^3 \text{ cm}^{-3}$  at  $r = 3000 \text{ AU}$ , the maximum number of quantum states for a constant electron temperature of  $T_e = 9000 \text{ K}$  is  $n_{\text{max,D}} = 345$  and  $27764$ , respectively.

#### 4.1.2 The effect of pressure ionization

We consider a pure hydrogen gas. If the mean distance between two atoms is  $d$ , then there will be no bound states  $n$  if the orbital radius  $a$  of the electron, that is given as  $a_0 n^2$  where  $a_0$  is again the Bohr radius, is comparable with or larger than  $d/2$ . With

$$d \approx \left( \frac{3}{4\pi N_{\text{H}}} \right)^{\frac{1}{3}} \quad (4.20)$$

where  $N_{\text{H}}$  means the hydrogen density, the maximum bound level  $n_{\text{max,P}}$  of the hydrogen atom becomes

$$n^2 < \frac{d}{2a_0} = \left( \frac{3}{4\pi N_{\text{H}}} \right)^{\frac{1}{3}} \frac{1}{2a_0} \quad \Rightarrow \quad n \leq n_{\text{max,P}} = 7656 \cdot N_{\text{H}}^{-\frac{1}{6}} \quad (4.21)$$

and this drop in  $n_{\text{max,P}}$  with increasing hydrogen density is plotted in Figure 4.5.

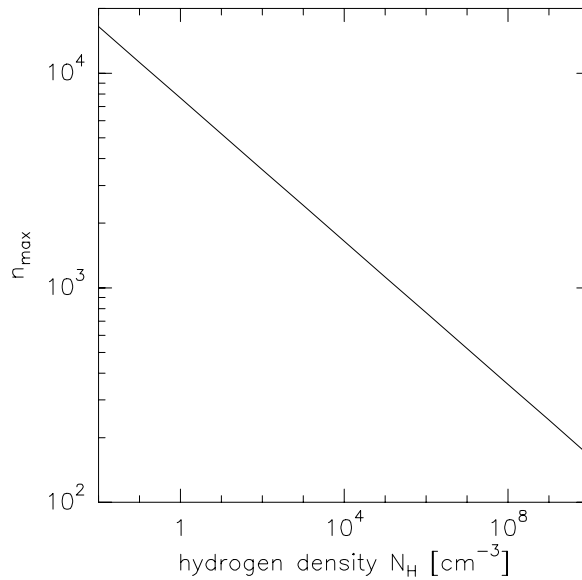


**Figure 4.5:** Dependence of the maximum bound quantum state of the hydrogen atom  $n_{\text{max,P}}$  on the hydrogen density in the case of pressure ionization.

For this so-called *pressure ionization* no good theory is at hand. The picture we have is a static one, since it does not take into account that the ions move relative to each other. So the maximum quantum number we get from Equation (4.21) can only be a rough estimate. Nevertheless, we will use this picture to get an impression of the importance of the pressure ionization compared to the effect of Debye-shielding.

In the case of an ionized gas, the level population of the recombining hydrogen (when neglecting additional ions) is given by the Equations (4.11) and (4.12), depending on whether there are LTE or NLTE conditions. The total number density of neutral hydrogen then calculates

$$N_{\text{H}} = \sum_n N_n \quad \longrightarrow \quad \sum_n^{n_{\text{max}}} N_n \quad (4.22)$$

where the infinite sum on the left is reduced via the effect of Debye–shielding to a finite sum with the maximum level  $n_{\max,D}$  as the summation limit. We carried out calculations for the conditions predominating in the wind zone of MWC 349, starting at  $r = 4.7R_{\odot}$  which would be the stellar radius in the case of a main sequence star. The corresponding electron density, which is decreasing in outward direction, is plotted on the  $x$ -axis in both panels of Figure 4.6 whereas the radial distance from the star is shown by the scale on top of the plots.

In the left panel we displayed the hydrogen column density resulting from the summation of the level populations (Equation (4.22)) from  $n = 1$  to  $n = n_{\max,D}$ . Because of the large number of contributing levels, the influences of levels being in NLTE is negligible; calculations performed for both cases led to (in good approximation) the same results. The right panel contains the comparison of the maximum quantum numbers calculated in the case of Debye–shielding (blue line) and of pressure ionization (red line). Interestingly, the curve for  $n_{\max,P}$  is always below the one for  $n_{\max,D}$ . This means that the Debye–shielding provides only an *upper* limit of existing bound levels. This leads also to an upper limit of the hydrogen density that can be calculated according to Eq. (4.22). If this hydrogen density is then inserted into Eq. (4.21) to evaluate  $n_{\max,P}$ , we find that  $n_{\max,P} < n_{\max,D}$  and that the hydrogen density that can now be evaluated by summation of the level populations up to  $n_{\max,P}$  is smaller than the value inserted. So we can draw the conclusion, that the number of bound levels we get from the effect of pressure ionization can only be a *lower* limit to the real number  $n_{\max}$  which must then lie between the two limiting values, i.e.  $n_{\max,P} < n_{\max,\text{real}} < n_{\max,D}$ .

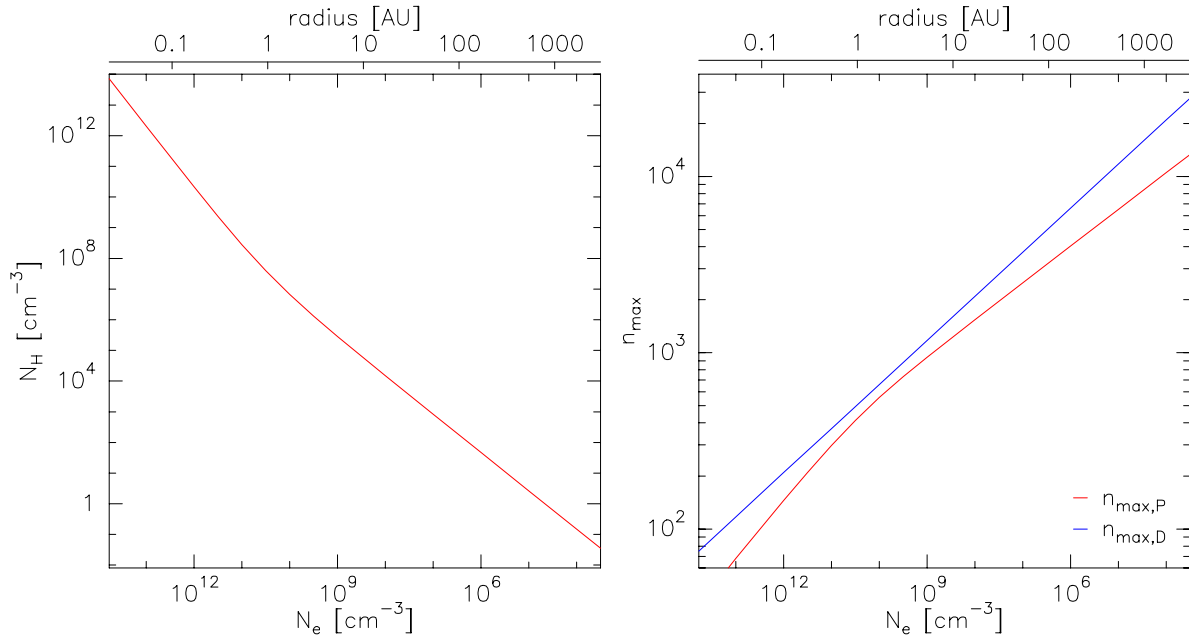


**Figure 4.6:** *Left panel:* Hydrogen density calculated with the help of Equation (4.22). The summation extends to the maximum level  $n = n_{\max,D}$  which is determined at each corresponding electron density. *Right panel:* Comparison between the maximum bound levels possible in the case of Debye–shielding (blue line) and of pressure ionization (red line). Debye–shielding leads to an upper limit, and pressure ionization to a lower limit of  $n_{\max}$ . The real value must lie somewhere in between. For the calculations presented in both plots we inserted the conditions existing in the wind zone around MWC 349.

Since we do not know the real hydrogen density that should be inserted for determining the maximum bound level of the hydrogen atom, and because of the still undeveloped theory of the pressure ionization, we will use the values we get from the Debye–shielding,  $n_{\max} \equiv n_{\max,D}$  in the following discussion.

## 4.2 Einstein coefficients of the neutral hydrogen atom

During a transition from an upper state  $n$  to a lower state  $n'$  of the hydrogen atom, a photon of frequency  $\nu_{nn'} = Ry \left( \frac{1}{n'^2} - \frac{1}{n^2} \right)$  is emitted, and the Einstein coefficient of spontaneous emission,  $A_{nn'}$ , for such a transition is given by

$$A_{nn'} = \frac{g_{n'}}{g_n} \frac{8\pi^2 e^2 \nu_{nn'}^2}{mc^3} f_{nn'} \quad (4.23)$$

where  $g_n$  and  $g_{n'}$  are the statistical weights of the upper and lower level  $n$  and  $n'$ , respectively;  $e, m_e$  are the charge of the electron and its mass, and the function  $f_{nn'}$  is called the oscillator strength whose computation is performed in Appendix B.

The dependence of  $A_{nn'}$  on the quantum number  $n$  is demonstrated for the first six hydrogen series in Figure 4.7. As can be seen, in all cases the Einstein coefficients can be approximated by a power law, at least for the levels with high quantum numbers. Since the oscillator strength is (if  $n$  is large enough) roughly proportional to  $n^{-3}$ , it follows that  $A_{nn'} \sim n^{-5}$  (a detailed calculation provides  $\sim n^{-5.005}$ ).

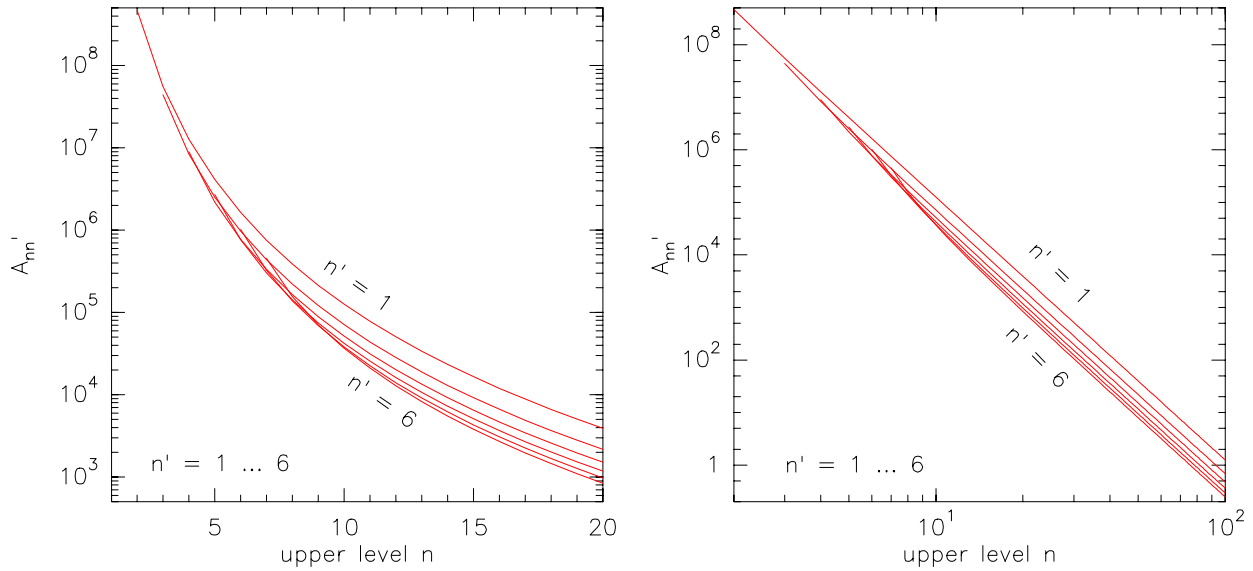


**Figure 4.7:** Einstein coefficients of spontaneous emission for the first six hydrogen series.

In the following discussion we will concentrate on the Pfund series, for it is the only series whose transitions occur in the wavelength region of the CO first overtone bands. In the low resolution spectrum the individual Pfund lines from Pf(17) up to the Pfund decrement are present whereas the wavelength range of the high resolution spectrum ( $\lambda = 2.285 \dots 2.340 \mu\text{m}$ ) contains only Pf(32) to Pf(100). The quantum number  $n = 32$  is high enough so that we can approximate the Einstein coefficients by

$$A_{n,5} \simeq 3.023 \cdot 10^9 n^{-5}. \quad (4.24)$$

## 4.3 Emission of the Pfund series

As we are dealing with case B recombination theory, the emission of the Pfund lines is optically thin. We can therefore easily calculate the intensity at every wavelength of the spectrum by folding

the energy given by Equation (4.1) with the local profile function of the hydrogen gas,  $\Phi_{\text{H}}(\nu)$ , and integrating over the emitting space

$$I_{\nu_0} = \iint E_{\nu_0} \Phi_{\text{H}}(\nu) d\nu dV = \iint N_n A_{n,5} h\nu_0 \Phi_{\text{H}}(\nu) d\nu dV . \quad (4.25)$$

The level population,  $N_n$ , follows from Equation (4.12), and for the Einstein coefficients we use the approximation (4.24).

Having smoothed the resulting spectrum to the spectral resolution by folding the intensity  $I_{\nu_0}$  of Eq. (4.25) with the profil function of the spectrometer,  $\Phi_{\text{res}}(\nu)$ , we end up with the flux density that is measured at earth after division with  $4\pi d^2$  where  $d$  is the distance of MWC 349 which is  $\sim 1.2$  kpc

$$F_{\nu_0} = \frac{1}{4\pi d^2} \int I_{\nu_0} \Phi_{\text{res}}(\nu) d\nu . \quad (4.26)$$

To get a first impression of the shape of the Pfund line emission spectrum, we use a simplified model: We assume a partially ionized hydrogen gas of constant electron temperature and density, and for the profile function of the gas as well as of the spectrometer we take a gaussian one which is of the form

$$\Phi(\nu) = \frac{1}{\sqrt{\pi} \frac{\nu_0}{c} v} \exp \left[ - \left( \frac{\nu - \nu_0}{\frac{\nu_0}{c} v} \right)^2 \right] . \quad (4.27)$$

Here,  $v$  is the most probable velocity and will be referred to as the ‘gaussian velocity’ which is in the case of the thermal velocity given by  $v = v_{\text{th}} = \sqrt{2kT/m}$  for particles having a Maxwellian velocity distribution, while in the presence of an additional turbulence it becomes  $v = \sqrt{v_{\text{th}}^2 + v_{\text{turb}}^2}$ . In the profile function of the spectrometer  $v$  means its velocity resolution which is for our high resolution spectrum about 15 km/s.

The influences of the different parameters on the Pfund line emission spectrum are summarized in Figure 4.8. Because a decrease in density by a factor of 10 leads to a drop in the intensity by a factor of 100 ( $N_n \sim N_e^2$ , see Eq. (4.12)), we have overlaid the diverse curves in the panels for a better visualization by plotting them on different scales.

There are some general aspects of the Pfund line spectrum, being worth to be discussed first: (i) a decrease in intensity with increasing quantum number  $n$  of the Pfund lines, and (ii) the formation of a ‘quasi-continuum’. To understand the behaviour of decreasing intensity we take a look at the intensity ratio of two neighbouring Pfund lines. This ratio is according to Eq. (4.1) independent of the electron density and is for large  $n$  of course smaller than 1, because essentially it can be formulated

$$\frac{I_{\text{Pf}(n+1)}}{I_{\text{Pf}(n)}} \sim \left( \frac{n}{n+1} \right)^5 . \quad (4.28)$$

Decisive for the second characteristic feature is the decreasing wavelength difference between neighbouring Pfund lines with increasing quantum number  $n$  which leads to a blend of the individual lines. So the higher order Pfund lines seem to form a ‘quasi-continuum’ which ends in an intensity cut-off near the edge of band of the Pfund series, known as the Pfund *discontinuity* or Pfund *decrement* and occuring at  $\lambda \simeq 2.2794 \mu\text{m}$  where the number of bound levels approaches infinity (indicated in the Figure as  $\text{Pf}(\infty)$ ).

A necessary condition for the formation of this ‘quasi-continuum’ that extends up to the Pfund decrement is, however, that the electron density is low enough to allow the highest bound levels to exist. Else, as shown in the upper left panel of Figure 4.8, the Pfund spectrum ends at much lower quantum number and its ‘continuum’ formation is restricted to only a few lines.

For electron densities  $N_e \leq 10^6 \text{ cm}^{-3}$  non LTE effects become obvious (upper right panel): the intensity drops with decreasing  $N_e$  below its LTE value. This decrease in intensity becomes

apparent especially for smaller quantum numbers where the  $b_n$  factors strongest deviate from 1 (see Figure 4.2).

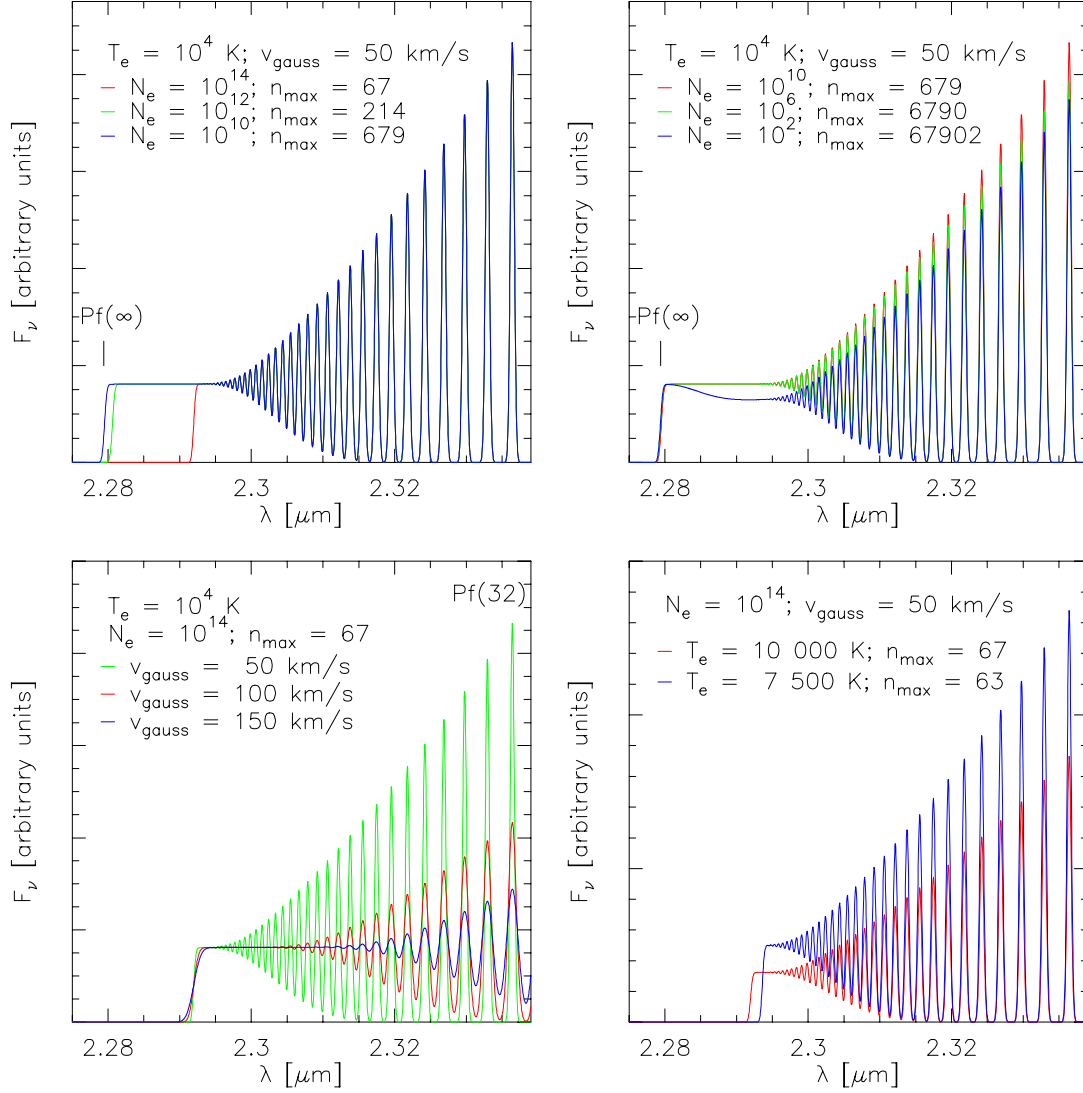


**Figure 4.8:** Synthetic Pfund spectra showing the influences of the various parameters: the maximum bound level for electron densities guaranteeing LTE conditions (upper left); NLTE contributions with decreasing  $N_e$  (upper right); broadening of the individual lines and the change in the onset of the quasi continuum caused by different gaussian velocities (lower left); and the influence of the electron temperature (lower right).

In the third panel (lower left) the gaussian velocity that determines the width of the individual Pfund lines is varied. Since the profile function is normalized,  $\int \Phi(\nu) d\nu = 1$ , the higher the velocity, the smaller is the intensity of the lines and the broader become the lines. Because of this broadening the ‘quasi-continuum’ of the spectrum begins at much higher wavelength, i.e. for Pfund lines with much smaller quantum number.

The last plot finally demonstrates the influence of the electron temperature that was set to 7 500 K and 10 000 K, respectively. Two consequences of the higher temperature are obvious: a lower intensity of the lines, and a higher number of bound states (lower right panel).

The real profile of the Pfund lines cannot be a gaussian one because the thermal velocity of the hydrogen gas at  $T_e \simeq 10\,000$  K is only about 12 km/s whereas the individual lines seem to have a width of  $\sim 50$  km/s. Such a velocity component from the environment of MWC 349 is not a

surprising feature. Several of the atomic and ionic emission lines (Hamann & Simon 1986), the cm and mid IR hydrogen recombination lines, as well as the ‘pedestal’ feature of the double-peaked mm recombination maser lines show such a velocity component (Smith et al. 1997 ; Thum, Martín-Pintado & Bachiller 1992). It is often ascribed to the wind of MWC 349. For this reason we next calculate the profile of a recombination line whose emission comes from a spherical wind with a terminal velocity of  $v_{\text{wind}} \simeq 50 \text{ km/s}$ .

Only the local line of sight component of the wind velocity is decisive. It shifts the line according to the Doppler law to higher or lower frequencies so that  $\nu_0$  in Equation (4.27) has to be replaced by  $\nu_0(1 \pm v_{\text{los}}/c)$  with  $v_{\text{los}} = v_{\text{wind}} \sin \theta \cos \phi$  (see Figure 4.9 for the coordinate system used).

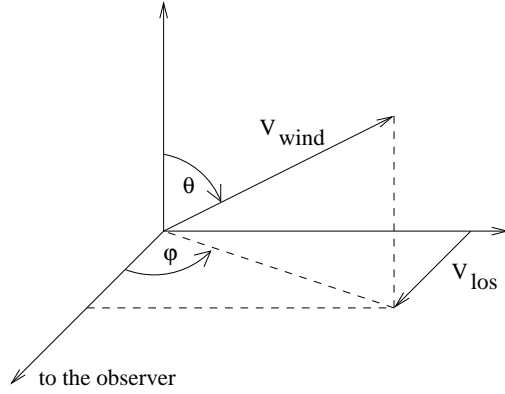


**Figure 4.9:** Sketch of the coordinate system used for the wind profile calculations.  $v_{\text{los}}$  means the line of sight component of the spherically symmetric wind velocity;  $\theta$  and  $\phi$  are spherical coordinates.

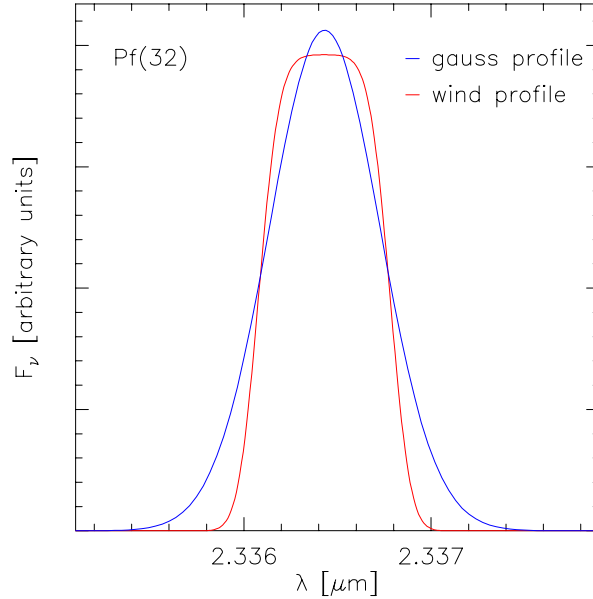


**Figure 4.10:** Comparison of the Pf(32) line with a pure gaussian line profile and with a profile resulting from a spherical stellar wind of constant velocity.

The difference between a gaussian profile and a profile from a spherical wind can be seen in Figure 4.10: the shape of the wind profile looks more or less like a box with a flat top and steep wings. The softening of the box follows from taking into account the thermal velocity of the recombined hydrogen gas and from the folding with the profile of the spectral resolution of  $\sim 15 \text{ km/s}$ . Compared with the wind profile, the gauss profile has broader wings and a narrower rounded top. But the full width at half maximum is for both curves the same.

For the calculations of the total Pfund line spectrum emitted from a spherical wind of constant velocity we split the wind zone into  $N$  distinct shells, each having an average electron density which is kept constant over the shell. The outer radius of each shell is defined as the radius where the real density has dropped to one tenth of its value at the inner edge of the shell. Then, according to the electron density distribution given by Equation (3.6), the outer radius can be written as  $r_{\text{out}} = \sqrt{10} \cdot r_{\text{in}}$ , and the volume of such a shell calculates as  $V = \frac{4\pi}{3}(r_{\text{out}}^3 - r_{\text{in}}^3) \simeq 128.27 r_{\text{in}}^3$ . The volume of the neighbouring shell connected to larger radii is about 32 times larger, but because the density in this shell dropped to one tenth, the level population and therefore also the intensity is a hundred times lower than for the first shell. This leads to an intensity of the second shell which is only about 32 per cent of the value emitted from the first one, and the total flux,  $F_\nu$ , which is



added up for all shells is given by

$$F_\nu = F_{\nu_0} + 0.32F_{\nu_0} + (0.32)^2 F_{\nu_0} + \dots = \sum_{i=0}^{N-1} (0.32)^i F_{\nu_0} \xrightarrow{N \rightarrow \infty} \frac{F_{\nu_0}}{1 - 0.32} \simeq 1.47 F_{\nu_0} \quad (4.29)$$

which means that the first shell already produces  $\sim 68\%$  of the total emission, whereas the net contribution of shells with larger radii, i.e. with a much smaller electron density, rapidly becomes negligible. Consequently, the major part of the total Pfund line emission is produced in the inner regions where the density is highest. In addition, since the emission of a shell is proportional  $N_e^2 r_{\text{in}}^3$  with  $r_{\text{in}} \sim N_e^{-3/2}$  it follows that

$$F_\nu = 1.47 \cdot F_{\nu_0} \sim \sqrt{N_{e,0}} \quad (4.30)$$

where  $\sqrt{N_{e,0}}$  is the maximum electron density that exists within the innermost shell which contributes to the Pfund line emission.

We start at  $r \simeq 100 R_\odot$  which was found from the modeling of the continuum emission to be a reasonable choice for the inner radius of the wind zone (see Chapter 3.2). There, the electron density is about  $10^{11} \text{ cm}^{-3}$ . Then we calculate the emission from several shells taking into account the interstellar visual extinction of  $\sim 8$  mag and also the local standard of rest velocity of  $\sim 8 \text{ km/s}$  (Thum, Martín-Pintado & Bachiller 1992; Thum et al. 1995). The emission of the first four shells as well as the total Pfund line emission arising in the wind zone is plotted in Figure 4.11.

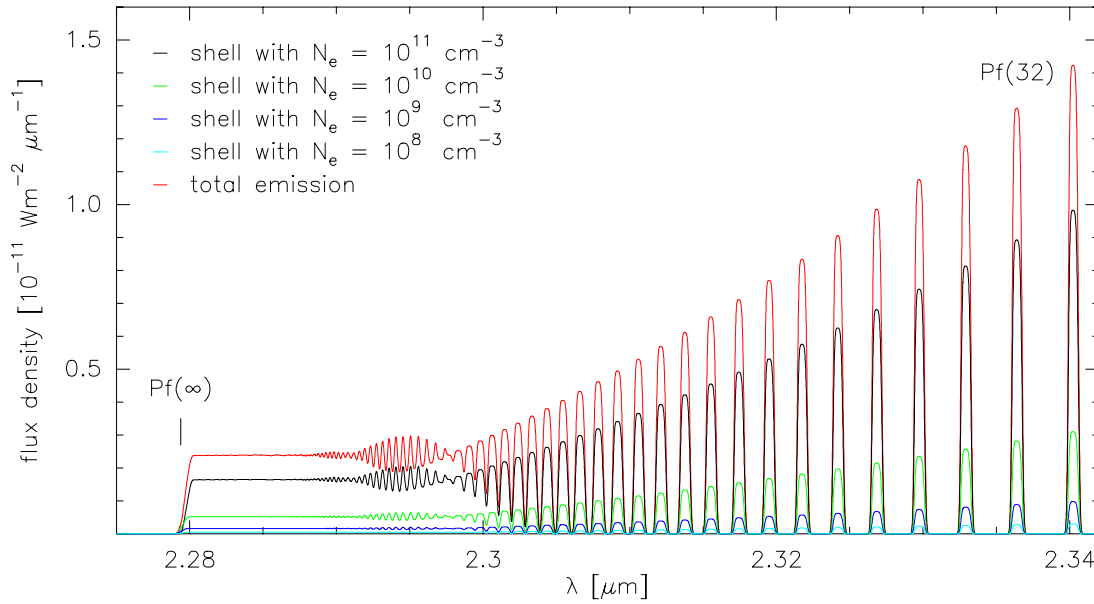


**Figure 4.11:** Emission of the Pfund series from several spherical wind shells of constant electron density. Shown are four neighbouring shells and the total Pfund line emission (red line) which is mainly determined by the first three shells.

If we compare the total emission produced by the wind zone with the emission of the observed high resolution spectrum (Figure 3.13) we find that our model calculations provide a flux density which is at least ten times larger than the observed one. A precise determination of the real strength of the Pfund line emission from the observations is not possible because the CO band spectrum extends from about  $2.293 \mu\text{m}$  up to  $\sim 2.5 \mu\text{m}$  (see Chapter 5). At each wavelength that corresponds to one Pfund line there is also a contribution from the CO bands to the total flux density. But since the strength of the CO contribution at each wavelength strongly depends on the conditions

under which the CO lines are emitted, the Pfund line emission cannot be modeled independently but has to be fit to the observations together with the CO bands.

We can, however, draw some conclusions from this model spectrum: First of all, the real emission ought to be some ten times smaller which means according to Equation (4.30) that the highest electron density that can take part of the emission must be in the order of  $N_{e,0} \leq 10^9 \text{ cm}^{-3}$ . On the other hand, the Pf(32) line for example, which is an isolated line in the pure Pfund spectrum, clearly rises above a low ‘quasi-continuum’ that is formed from the CO bands. The Pfund contribution at this wavelength should therefore be more than about 60 % of the total emission, leading to an electron density of the innermost shell of at least  $N_{e,0} \geq 3.6 \cdot 10^8 \text{ cm}^{-3}$ . So the maximum possible electron density of the innermost shell that is found to contribute to the Pfund line emission can be restricted to  $3.6 \cdot 10^8 \text{ cm}^{-3} \leq N_{e,0} \leq 10^9 \text{ cm}^{-3}$ . This range in electron density coincides to a certain extent with the value needed for the hydrogen maser line emission for which Streltinski et al. (1996) and Thum et al. (1998) found electron densities as high as  $10^8 \text{ cm}^{-3}$ . But it does *not* coincide with the maximum electron density derived from the modeling of the continuum emission where we found  $N_e(R_0) \simeq 1.34 \cdot 10^{11} \text{ cm}^{-3}$  (see Table 3.3 in Chapter 3.2). Here, an electron density of  $10^9 \text{ cm}^{-3}$  at the inner edge of the wind zone would underestimate the continuum emission by orders of magnitude (green curve in Figure 3.10).

How can we eliminate this inconsistency? A possible starting-point for solving this problem is the question whether in the regions of highest density the recombined hydrogen atoms have a realistic chance to deexcite their populated levels via spontaneous emission, or whether collisions can depopulate the levels without any or with only very little production of radiational emission.

To get an idea of how important collisions are, we have to compare the timescale for spontaneous emission with the mean collision time. For spontaneous emission to be suppressed, the collision time must be smaller than the decay time of the level  $n$ . This leads to the following inequality

$$\tau_{\text{rad}} = \frac{1}{A_{n,5}} > \tau_{\text{coll}} = \frac{1}{\sigma \langle v \rangle N}. \quad (4.31)$$

$A_{n,5}$  is the Einstein coefficient for spontaneous emission of a Pfund line,  $\sigma$  is the collision cross section,  $\langle v \rangle = \sqrt{8kT/\pi\mu}$  is the mean relative speed between the colliding partners with the reduced mass  $\mu = m_1 m_2 / (m_1 + m_2)$ , and  $N$  is the mean density of the perturbing particles which can be electrons and protons. But because of the  $\sim 1000$  times higher mass of the protons that leads to a mean collision energy which is about 30 times lower than for the electrons, collisions of protons with hydrogen are neglected.

The collision cross section is subject to some uncertainties. Unfortunately, there are no extensive tables at hand so that we decided to take the geometric cross section of the hydrogen atom in the state  $n$  given by  $\sigma = \pi a_n^2 = \pi n^4 a_0^2$  to get a rough estimate of the collision time. Here,  $a_n$  is the radius of the  $n$ -th level, and  $a_0$  is the Bohr radius. With this simplification and with the approximation made in Equation (4.24) for the Einstein coefficients, we can derive the following relation between the electron density and the level  $n$

$$n > \left( \frac{3.023 \cdot 10^9}{\pi a_0^2} \sqrt{\frac{\pi\mu}{8kT}} \frac{1}{N_e} \right)^{\frac{1}{9}} \simeq 93.94 \cdot N_e^{-\frac{1}{9}}. \quad (4.32)$$

We inserted the value of 9000 K for the electron temperature as found from the continuum calculations. For all levels  $n'$  having a higher quantum number than the one given by Equation (4.32) no spontaneous emission into the Pfund lines can occur. The regions where spontaneous emission and collisional depopulation occurs are shown in Figure 4.12.

According to these calculations, for electron densities  $N_e > 2.17 \cdot 10^4 \text{ cm}^{-3}$  no Pfund line emission at all should be observable in the wavelength range of our high resolution spectrum. The geometric collision cross section can therefore be only an upper limit to the real one. In addition we did not

take into account the influences caused by the presence of free protons. Since for the overall charge neutrality the number densities of electrons and protons are equal, much more collisions between electrons and protons instead of collisions between electrons and hydrogen atoms should take place leading to a retarded collision time and therefore to a more efficient spontaneous emission at the densities derived from the model calculations.

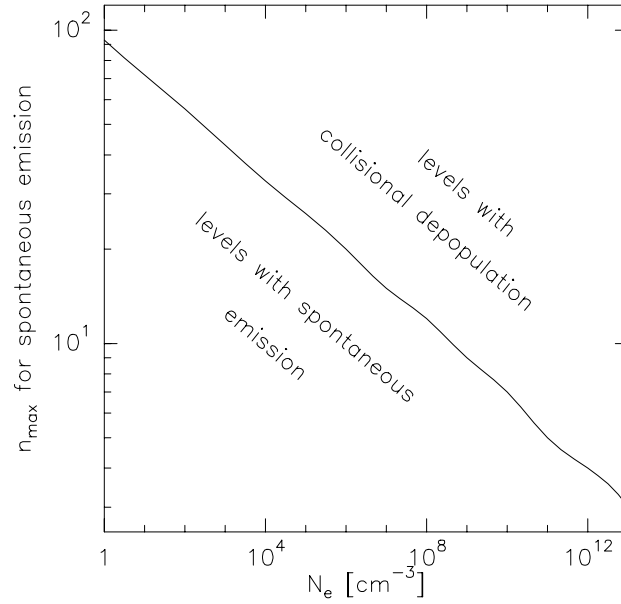


**Figure 4.12:** Demonstration of the maximum level  $n$  at a given electron density that can emit the Pfund line via spontaneous emission. The collision cross section used is the geometric one, and the electron temperature was fixed to 9 000 K, the same value is for the continuum calculations.

Although these computations by no means lay claim to completeness, they nevertheless seem to go into the right direction, namely the suppression of Pfund line emission in the regions of extreme high density ( $N_e > 10^9 \text{ cm}^{-3}$ ) by depopulating the quantum states via collisions. Such a physical picture is quite promising in explaining the existence of an electron density as high as  $10^{11} \text{ cm}^{-3}$  that is responsible for the continuum emission in the visible and UV range of the spectrum while the Pfund line spectrum reflects only electron densities which must be lower than  $10^9 \text{ cm}^{-3}$  to not come into a conflict with the measured flux density.

An additional aspect has also to be taken into account. Since we are dealing with recombination theory, we assumed the emission lines to be optically thin throughout, but at these high densities also optical depth effects might play a significant role leading to a reduced flux density (see e.g. Osterbrock 1989). A detailed radiation transport calculation for the hydrogen recombination lines is, however, beyond the scope of this thesis.

Finally, we calculated the total Pfund line spectrum (1) in LTE with a gaussian line profile where  $v_{\text{gauss}}$  was set to 50 km/s, and (2) coming from a spherical symmetric wind of constant velocity  $v_{\text{wind}} = 50 \text{ km/s}$  with an electron density distribution of the form  $N_e \sim r^{-2}$  where  $N_{e,0} \simeq 10^9 \text{ cm}^{-3}$  is chosen as the density at the inner radius. Both spectra are compared in Figure 4.13.

As a first result, we find that the wind spectrum shows no deviation from LTE conditions. This is, however, not surprising because for quantum numbers  $n \geq 32$  the  $b_n$  factors are in the order of 1 for electron densities  $\geq 10^7 \text{ cm}^{-3}$ . So, we expect deviations only for the outermost parts of the wind zone to occur, but as we have shown above, these parts hardly contribute to the total flux density.

In addition, in both cases the shape of the Pfund line spectrum looks very similar in most wave-

length parts. Only in the wavelength range where the individual Pfund lines start to superimpose themselves, the flux between the lines in the gauss profile spectrum is somewhat larger because of the broader wings of the individual lines that start to overlay first.

Since the calculations with pure gaussian line profile need much less computation time, and since the spectra calculated with a gaussian and with a wind profile look rather similar, we decided to restrict the subsequent calculations of the Pfund line spectrum to this simple case, keeping however in mind, that there might be some uncertainties in the wavelength range between  $2.298 \mu\text{m}$  and  $2.31 \mu\text{m}$ .

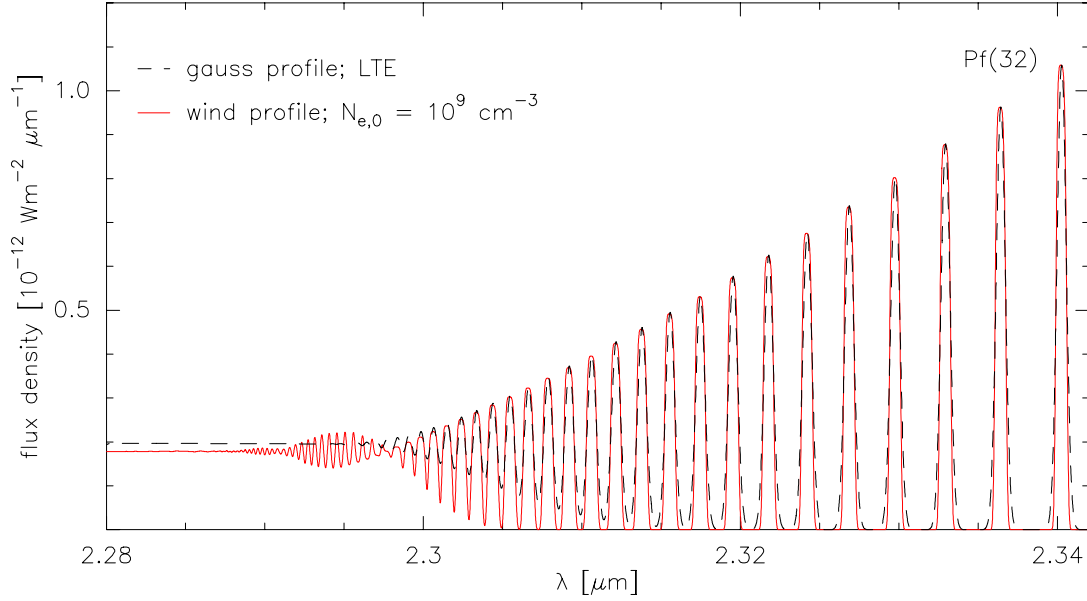


**Figure 4.13:** Comparison between the Pfund spectrum calculated with gaussian velocity under LTE conditions and the Pfund spectrum calculated for a wind scenario.

## Chapter 5

# Modeling of the CO band emission

### 5.1 The physics of CO molecules

The energy of a diatomic molecule in the rotational level  $J$  of the vibrational level  $v$  is given, in the model of a vibrating rotator (Dunham 1932a, 1932b), by

$$E(v, J) = hc \sum_{k,l} Y_{k,l} \left( v + \frac{1}{2} \right)^k (J^2 + J)^l \quad k, l \geq 0 . \quad (5.1)$$

The parameters  $Y_{k,l}$  are constants. Their values for the CO molecule are published by Farrenq et al. (1991).

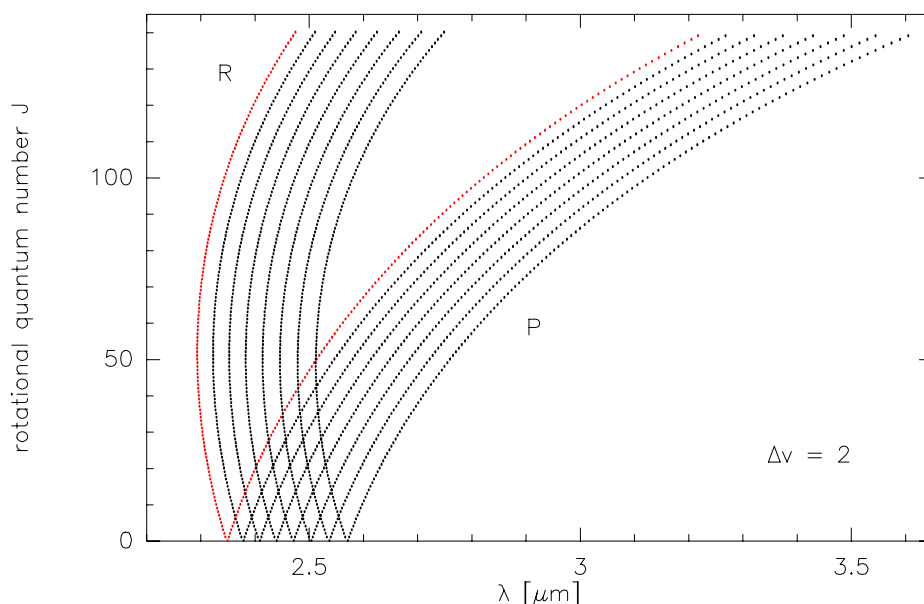


**Figure 5.1:** Wavelengths of vibrational-rotational transitions of the form  $(v, J) \rightarrow (v - 2, J \pm 1)$  that lead to the first-overtone bands of the CO molecule. Transitions of the  $(2 \rightarrow 0)$  band are plotted red.

The first overtone bands result from coupled vibrational-rotational transitions in the ground electronic state of the CO molecule, according to the selection rules  $\Delta v = 2$  and  $\Delta J = \pm 1$  (the ‘+’ sign marks transitions of the R-branch, the ‘-’ sign those of the P-branch). The wavelengths of the transitions are plotted in Figure 5.1 for  $v_{\text{upper}} = 2 \dots 9$  and  $J_{\text{upper}} = 1 \dots 140$ . Within each R-branch the wavelengths of the transitions with increasing rotational quantum number decrease

and reach a minimum for  $J = 51$ ; for higher  $J$ , they increase again, so that each band has a well-defined lower wavelength limit called *band head*.

In Figure 5.2 we display the wavelengths of vibrational-rotational transitions which fall into the wavelength range of our spectrum. Because of the small wavelength interval these are only transitions of the R-branches, namely transitions with  $J_{\text{upper}} = 3 \dots 99$  within the  $(2 \rightarrow 0)$  band, and  $J_{\text{upper}} = 21 \dots 81$  within the  $(3 \rightarrow 1)$  band.

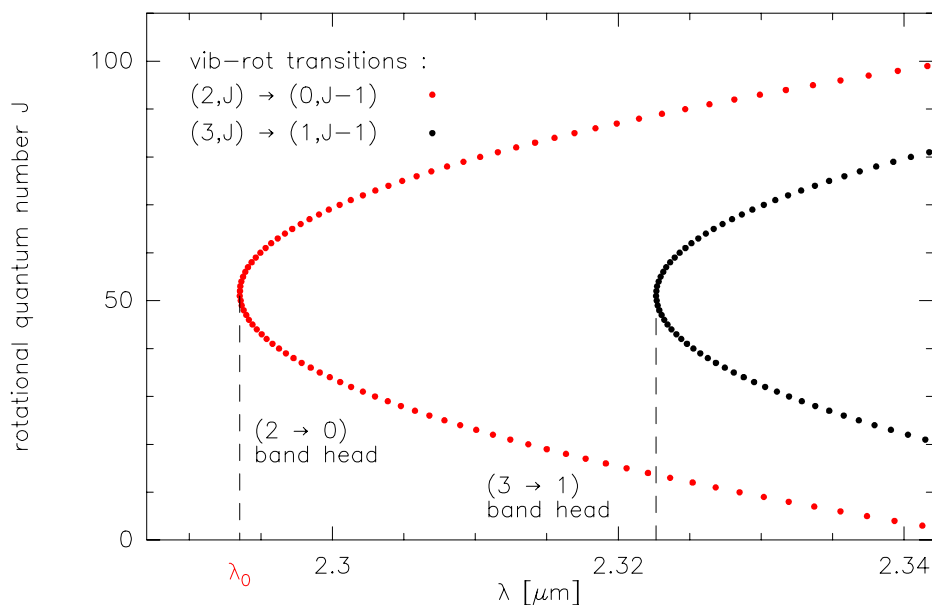


**Figure 5.2:** As Figure 5.1 but restricted to the wavelength range of our high resolution observations. Indicated are the wavelengths of the  $(2 \rightarrow 0)$  (denoted as  $\lambda_0$ ) and the  $(3 \rightarrow 1)$  band heads.

The difference between the wavelength of the band head and the wavelengths of the neighbouring transitions is rather small, so that even a narrow profile of the individual vibrational-rotational lines leads to a superposition; the result of this superposition is known as the band head structure<sup>1</sup> because if the temperature is high enough to excite the corresponding vibrational-rotational levels a maximum in intensity is achieved in this wavelength range that clearly dominates the CO spectrum. A detailed investigation of the formation of CO bands and bandheads has been given in an earlier work (Kraus 1997).

The shape of such a CO band can be seen in Figure 5.3 where, we plotted the optically thin emission calculated for the  $(2 \rightarrow 0)$  band overlaid on the observations. The lines are only thermally broadened with  $T_{\text{CO}} = 5\,000$  K, and the spectrum is smoothed to the spectral resolution of 15 km/s. The resulting band head structure is much too narrow compared to the observed one so that we have to look for additional broadening mechanisms.

The  $(2, 51) \rightarrow (0, 50)$  transition marks the lowest wavelength in the total CO first-overtone band spectrum. It is located at  $2.29353\,\mu\text{m}$  which will in the following be referred to as  $\lambda_0$ . Although some additional transitions contribute to the overall shape of the  $(2 \rightarrow 0)$  band head structure, the *rise* on the low wavelength side of the  $(2, 51) \rightarrow (0, 50)$  line, whose profile is of course strongly dependent on the broadening mechanisms, mainly determines the *rise*, or the onset of the total  $(2 \rightarrow 0)$  band head structure. If the emission at the low wavelength end of the spectrum is found

<sup>1</sup>In the literature the expression *band head* is used in two different ways: (i) in quantum mechanics it means the wavelength of the turn-over vib-rot transition, and (ii) in spectroscopy it denotes the location of maximum intensity occurring at the high frequency band edge because of the numerous superimposing lines. Our notation follows the spectroscopic one.

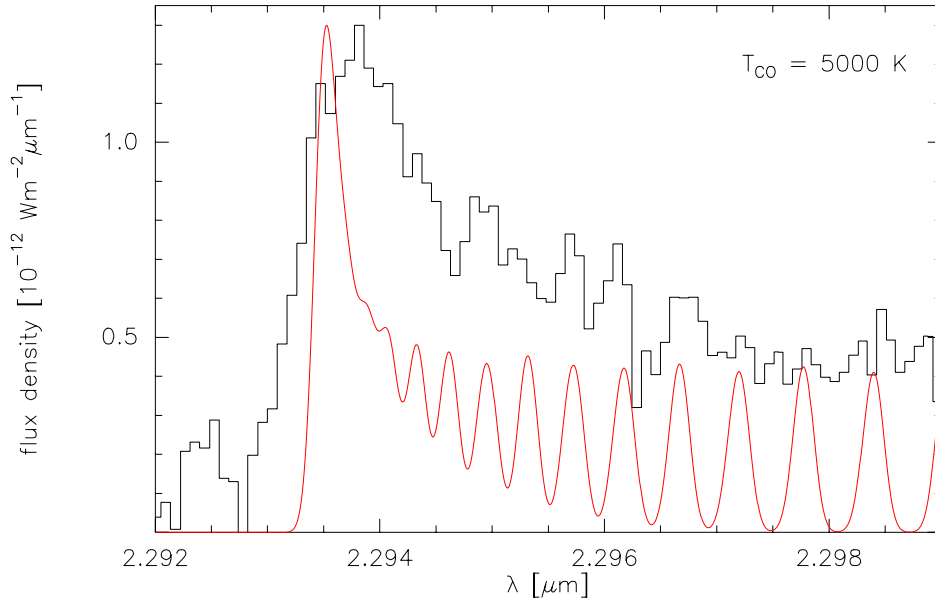


**Figure 5.3:** Comparison of a theoretical CO first overtone band spectrum calculated for optically thin emission with the observations. The lines are thermally broadened with  $T_{\text{CO}} = 5000$  K, and the spectrum is smoothed to the spectral resolution of 15 km/s.

to be optically thin, we can derive the *complete velocity information* of the CO gas from the wing of the  $(2, 51) \rightarrow (0, 50)$  line by determining the minimum wavelength,  $\lambda_{\text{min}}$ , at which the CO band apparently arises.

To quantify this statement we need to know the profile function,  $\Phi_{(2,51) \rightarrow (0,50)}(\nu)$ . Most processes that result in a line broadening lead to a gaussian or nearly gaussian profile (given by Equation (4.27)), like the thermal,  $v_{\text{th}}$ , and the turbulent motion,  $v_{\text{turb}}$ , the detector resolution,  $v_{\text{res}}$ , and as shown in Section 4.3 to first approximation also the motion within an expanding spherical wind of constant velocity,  $v_{\text{wind}}$ . Their superposition results again in a gaussian line profile but now with the combined most probable velocity

$$v_{\text{gauss}} = \sqrt{v_{\text{th}}^2 + v_{\text{turb}}^2 + v_{\text{res}}^2 + v_{\text{wind}}^2}. \quad (5.2)$$

Disk rotation, on the other hand, produces a double-peaked line profile (see e.g. Carr 1995; Kraus 1997), as long as the rotation axis is inclined with respect to the line of sight. When we assume the disk to rotate in a Keplerian fashion, the maximum rotational velocity  $v_{\text{rot,max}}$  arises at its inner edge. Therefore, a line with laboratory frequency  $\nu_0$  is shifted to

$$\nu \longrightarrow \nu_0 \cdot \left(1 + \frac{v_{\text{lsr}} + v_{\text{rot,los}}}{c}\right) \quad (5.3)$$

where  $v_{\text{rot,los}} = v_{\text{rot,max}} \cdot \cos i$  is the line of sight component of the maximum rotational velocity, and  $i$  means the inclination angle between the disk and the line of sight. The local standard of rest velocity,  $v_{\text{lsr}}$ , which causes an additional frequency shift has also been added<sup>2</sup>.

If we replace the frequency  $\nu_0$  in the original gauss profile (Equation (4.27)) by the shifted one (Eq. (5.3)), and the velocity  $v$  by  $v_{\text{gauss}}$  (Eq. (5.2)), we end up with the following profile function of the  $(2, 51) \rightarrow (0, 50)$  line

<sup>2</sup>This makes, of course, only sense because MWC 349 has a positive local standard of rest velocity.

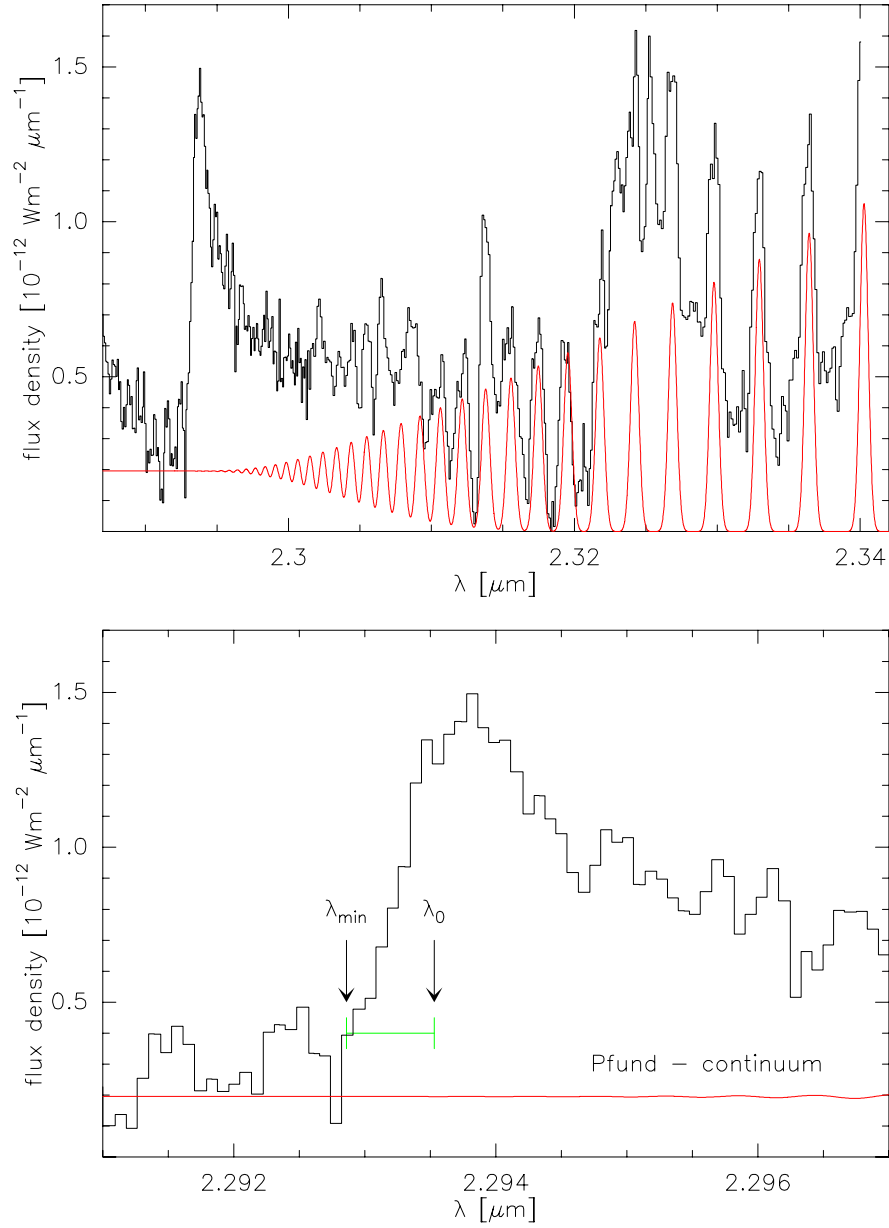


**Figure 5.4:** *Upper panel:* Pfund line spectrum together with the observed emission spectrum of Figure 3.13. In the wavelength region of the  $(2 \rightarrow 0)$  band head the Pfund emission forms a continuum of constant flux density which only leads to an offset of the CO band spectrum. *Lower panel:* Wavelength part containing the  $(2 \rightarrow 0)$  band head. Also indicated are the wavelengths  $\lambda_0$  and  $\lambda_{\min}$ .

$$\Phi(\nu) = \frac{1}{\sqrt{\pi} \frac{\nu_0}{c} \left(1 + \frac{v_{\text{lsr}} + v_{\text{rot,los}}}{c}\right) v_{\text{gauss}}} \cdot \exp \left[ - \left( \frac{\nu - \nu_0 \left(1 + \frac{v_{\text{lsr}} + v_{\text{rot,los}}}{c}\right)}{\frac{\nu_0}{c} \left(1 + \frac{v_{\text{lsr}} + v_{\text{rot,los}}}{c}\right) v_{\text{gauss}}} \right)^2 \right]. \quad (5.4)$$

For we are mainly interested in the *wing* of the profile, we define a parameter  $x$  that describes the fraction to which the intensity at the line center has dropped at frequency  $\nu = c/\lambda$ , i.e.

$$\frac{1}{x} \Phi(\nu = \nu_0) = \Phi(\nu = \nu_{\max} = \frac{c}{\lambda_{\min}}). \quad (5.5)$$



Combination of the Equations (5.4) and (5.5) leads to the following relation for  $\lambda_{\min}$

$$\frac{1}{\lambda_{\min}} = \frac{1}{\lambda_0} \left[ 1 + \frac{v_{\text{lsr}} + v_{\text{rot,los}}}{c} \right] \left[ \frac{v_{\text{gauss}}}{c} \sqrt{\ln x + 1} \right]. \quad (5.6)$$

The value of  $x$  must be larger than 2 to guarantee that the wavelength is indeed in the wing of the line. On the other hand, it cannot be chosen too high, because the uncertainties in the observations prevent an exact determination of the minimum wavelength. We find that  $x$  must be in the range of 5 – 10 (in this range the exact value of  $x$  is not of great interest since it hardly influences the result).

The contamination of the CO spectrum with the Pfund lines turns out to be no hindrance because as shown in Figure 5.4 in this wavelength range the Pfund lines form a continuum emission of constant flux density. From this Figure we can therefore read off  $\lambda_{\min} = 2.29285 \pm 0.00005 \mu\text{m}$ .

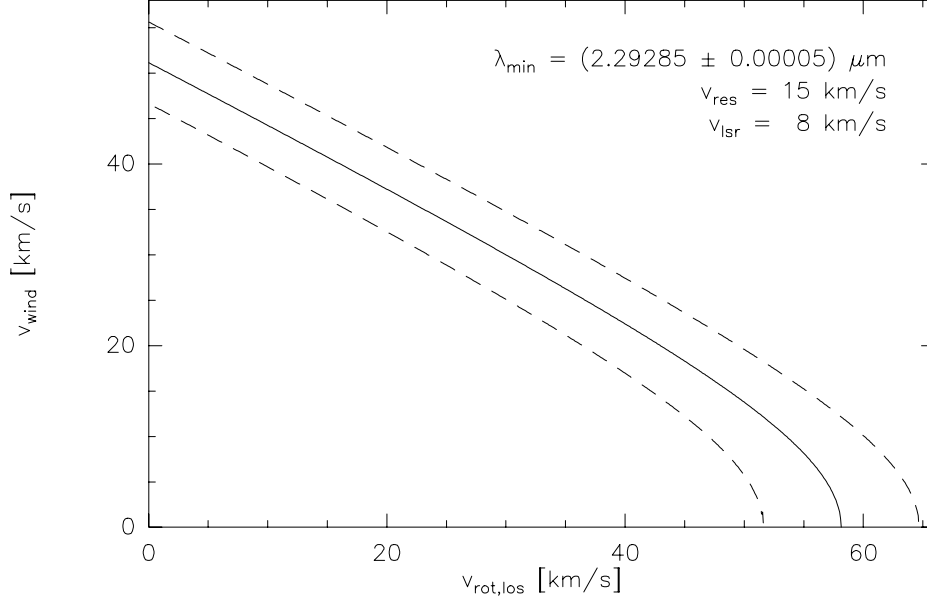


**Figure 5.5:** The dependence of  $v_{\text{wind}}$  on  $v_{\text{rot,los}}$  after Eq. 5.6 is shown. The solid line is for  $\lambda_{\min} = 2.29285 \mu\text{m}$ , the dashed line above (below) is for the lower (upper) limit of  $\lambda_{\min}$ .

Once  $\lambda_{\min}$  is fixed, Equation (5.6) relates the different velocity components. The thermal velocity,  $v_{\text{th}}$ , of CO molecules at a temperature of about 3500 K is less than  $\sim 1 \text{ km/s}$  and can be neglected in comparison with a spectral resolution of  $v_{\text{res}} = 10 \dots 15 \text{ km/s}$ . The same can be said about the turbulent velocity which is not likely to exceed the speed of sound. The main components of the gaussian velocity are therefore the spectral resolution and the wind velocity,  $v_{\text{gauss}} \simeq \sqrt{v_{\text{res}}^2 + v_{\text{wind}}^2}$ . Since the velocity resolution and the local standard of rest velocity have known values, Equation (5.6) can now be used to relate the remaining yet undetermined velocities, namely  $v_{\text{wind}}$  and  $v_{\text{rot}}$

$$v_{\text{wind}} \simeq \left[ \frac{c^2}{\ln x} \left( \frac{\lambda_0}{\lambda_{\min}} \frac{c}{c + v_{\text{lsr}} + v_{\text{rot,los}}} - 1 \right)^2 - v_{\text{res}}^2 \right]^{\frac{1}{2}}. \quad (5.7)$$

This result is shown by the solid line in Figure 5.5; the dashed lines above and below are for the lower and upper limit of  $\lambda_{\min}$ .

If the CO gas performs no rotation, its wind velocity is  $\sim 50 \text{ km/s}$ , which is the same as for the Pfund lines. On the other hand, without a wind one derives a rotational velocity projected to the

line of sight of  $\sim 58 \pm 7$  km/s. This value is larger than any other known rotational velocity around MWC 349, the highest being 42.5 km/s for He I (see Table 2.1 and Figure 2.1).

Up to now, only a statement about the maximum possible velocity components has been made. This enables us *not* to make any prediction about the *shape* of the total band head which is discussed next. But before we can continue with the CO band emission calculations we have to make clear how we handle the Pfund line spectrum. To fit the sum of CO and Pfund line emission to the observations we have to solve a two dimensional set of linear equations, i.e.

$$F_{\nu,i}(\text{Observation}) = A \cdot F_{\nu,i}(\text{CO}) + B \cdot F_{\nu,i}(\text{Pfund}) \quad i = 1, 2 \quad (5.8)$$

where  $A$  and  $B$  are the fitting parameters for the CO and the Pfund spectrum, respectively. Since the Pfund line emission seems already to be of right order,  $B$  will only little deviate from 1. After their determination, we can multiply the synthetic spectra with the fitting factors and subtract the Pfund line spectrum from the observations (Figure 3.13) to end up with the pure CO band spectrum. In each plot in the following sections, the Pfund line emission has been subtracted in this way and only the CO band emission is shown together with our calculated fits.

## 5.2 CO band emission under various circumstellar conditions

In the following, we assume the CO gas to be in LTE. Then the levels are populated following a Boltzmann distribution

$$N_{vJ} = \frac{N}{Z} (2J+1) e^{\frac{-E(v,J)}{kT}} \quad (5.9)$$

where  $N$  and  $T$  are the total number density and the temperature of CO molecules and  $Z$  is the total partition function, given as the product of the vibrational and the rotational partition function

$$Z = Z_v \cdot Z_J = \sum_v e^{\frac{-E_v}{kT}} \cdot \sum_J (2J+1) e^{\frac{-E_J}{kT}}. \quad (5.10)$$

In order to generalize earlier investigations (Kraus 1997) we now also take into account optical depth effects and compute the line intensities from the transfer equation

$$I_\nu = B_\nu(T) (1 - e^{-\tau_\nu}). \quad (5.11)$$

The optical depth is defined as  $\tau_\nu = \int \kappa_\nu ds$ , and  $\kappa_\nu$  is the absorption coefficient per cm of the discrete transitions. It is given by

$$\kappa_\nu = \frac{c^2 N_{vJ} A_{vJ;v'J'}}{8\pi\nu^2} \left( \frac{2j+1}{2j'+1} \cdot \frac{N_{v'J'}}{N_{vJ}} - 1 \right) \Phi_{\text{CO}}(\nu) \quad (5.12)$$

where  $\Phi_{\text{CO}}(\nu)$  is the profile function of the CO gas. The Einstein coefficients for the CO molecule,  $A_{vJ;v'J'}$ , are from Chandra, Maheshwari & Sharma (1996).

In the remaining part of this chapter we discuss the influence of individual profile functions, i.e. different velocity components of the CO gas, since the profile  $\Phi(\nu)$  is the most crucial parameter concerning the shape of the  $(2 \rightarrow 0)$  band head. For this, we investigate three different regions of band head formation whose corresponding velocity range can be concluded from Equation (5.7) (Figure 5.5):

- a spherical wind with a pure gaussian velocity of  $\sim 50$  km/s,
- a circumstellar Keplerian rotating disk with the maximum rotational velocity of  $\sim 60$  km/s, and

- a rotating medium with an additional gaussian velocity component, presumably a (disk-) wind.

Here, only the theoretical aspects of these scenarios are presented. The discussion whether the observed first overtone CO band emission from MWC 349 can really be described by one of these models, upon closer consideration of the real stellar and circumstellar conditions, follows in Chapter 6.

### 5.2.1 A gaussian line profile for the CO gas

In this first model we neglect rotation and assume a pure gaussian line profile. The velocity of the CO gas that follows from Eq. (5.7) is  $v_{\text{gauss}} \approx 50 \text{ km/s}$ .

For the calculation of the optical depth we assume the absorption coefficient to be constant along the line of sight. Then  $\tau_\nu$  is simply given as the product of the absorption coefficient per CO molecule times the CO column density,  $\tau_\nu = \kappa_\nu \cdot N_{\text{CO}}$ .

In Fig. 5.6 we plotted the absorption coefficient per CO molecule for temperatures,  $T_{\text{CO}}$ , between 3000 K and 5000 K, and a gaussian velocity of the gas of 50 km/s. In the wavelength range around the  $(3 \rightarrow 1)$  band head ( $2.322 - 2.325 \mu\text{m}$ ) the absorption coefficient is higher than in the region around the  $(2 \rightarrow 0)$  band head ( $2.293 - 2.295 \mu\text{m}$ ), and this effect becomes stronger with increasing temperature. Thus, the turn-over from optically thin to optically thick emission depends not only on the column density but also on the temperature of the gas: the  $(3 \rightarrow 1)$  band head becomes optically thick at lower temperature and lower column density than the  $(2 \rightarrow 0)$  band head.

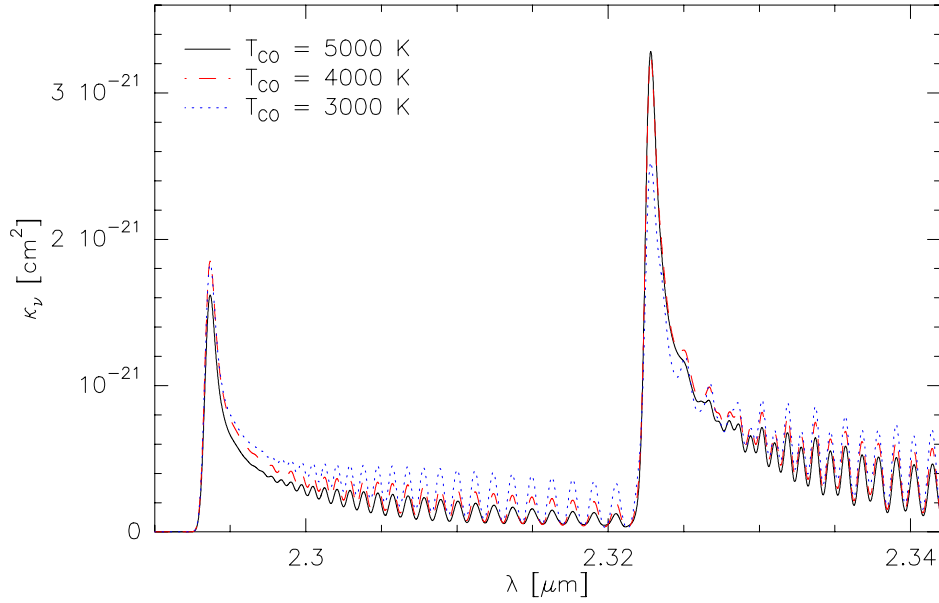


**Figure 5.6:** Absorption coefficient per CO molecule,  $\kappa_\nu$ , for temperatures of 3000 K (dotted line), 4000 K (dashed line), and 5000 K (solid line). The gaussian velocity of the CO gas is 50 km/s.

Next, we vary the CO column density and fix  $T_{\text{CO}}$  at 4000 K. The synthetic spectra in Figure 5.7 are calculated for the case of extreme optical depth (black line) and for CO column densities (from bottom to top) of  $10^{20}$ ,  $5 \cdot 10^{20}$ ,  $10^{21}$  and  $2 \cdot 10^{21} \text{ cm}^{-2}$ . With increasing column density the optical depth enlarges and the intensity tends towards its limiting blackbody value. In addition, the spectra show two characteristic features: a varying intensity ratio of the two band heads and a broadening of the band head structure.

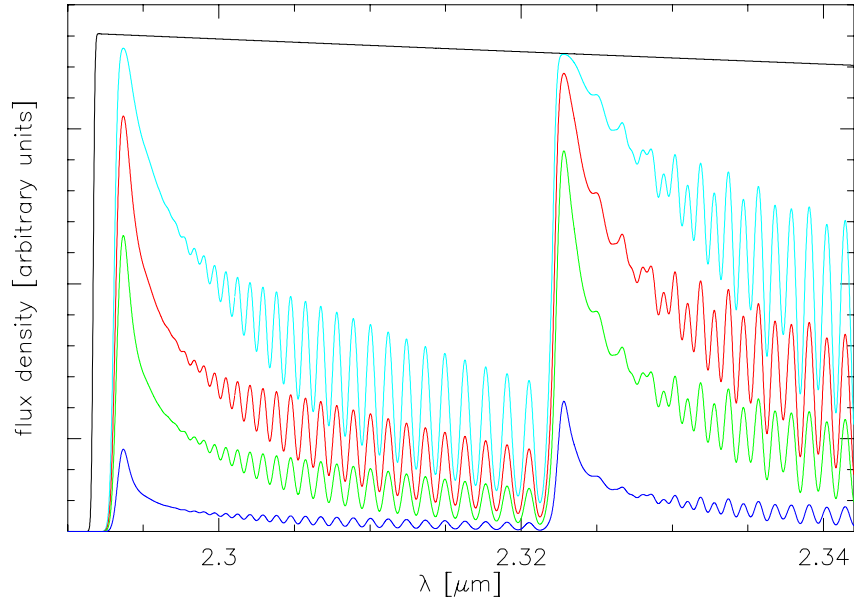


**Figure 5.7:** Calculated CO band emission spectra for a temperature of the CO gas of 4000 K, a gaussian velocity of  $\sim 50$  km/s, and a CO column density increasing from bottom to top:  $10^{20}$ ,  $5 \cdot 10^{20}$ ,  $10^{21}$ , and  $2 \cdot 10^{21}$   $\text{cm}^{-2}$ . The upper line represents the case for  $\tau \rightarrow \infty$ .

The first property can better be seen in Figure 5.8 where we plotted the flux density ratio of the  $(3 \rightarrow 1)$  and  $(2 \rightarrow 0)$  band head with temperature for different column densities. This ratio decreases with increasing column density, i.e. increasing  $\tau$ , and approaches 0.96 for  $\tau \rightarrow \infty$ . The determination of the column density with only the help of this ratio is, however, not unambiguous because the flux density ratio also depends on temperature. From our observations the flux density

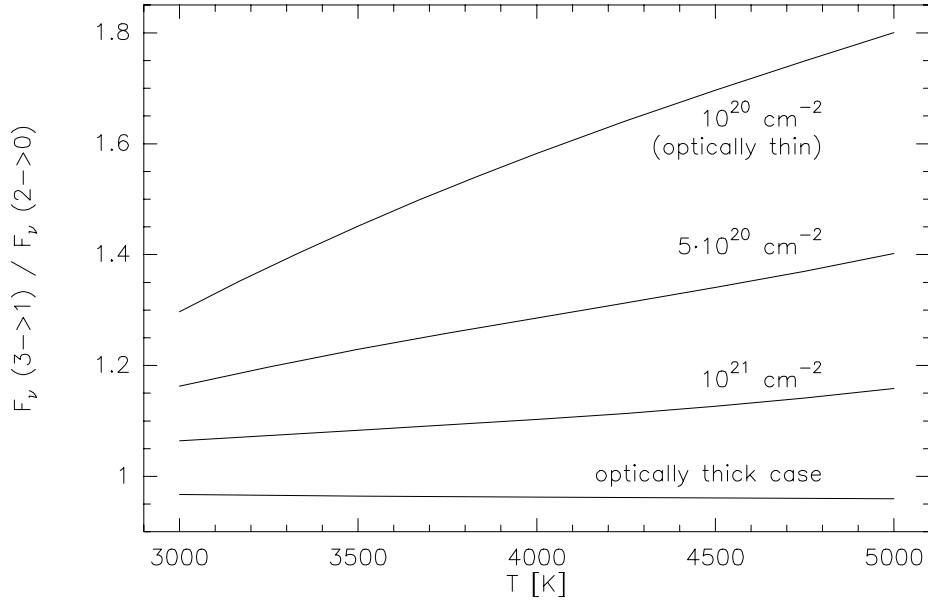


**Figure 5.8:** The flux density ratio of the  $(3 \rightarrow 1)$  and  $(2 \rightarrow 0)$  band heads as a function of temperature and column density. The ratio is highest in the optically thin case ( $N_{\text{CO}} \leq 10^{20} \text{ cm}^{-2}$ ) and approaches  $\simeq 0.96$  for  $\tau \rightarrow \infty$ .

ratio is not sufficient to derive a definite column density because the observed strength of the  $(3 \rightarrow 1)$  band head is subject to some uncertainty as discussed in Chapter 2.2.

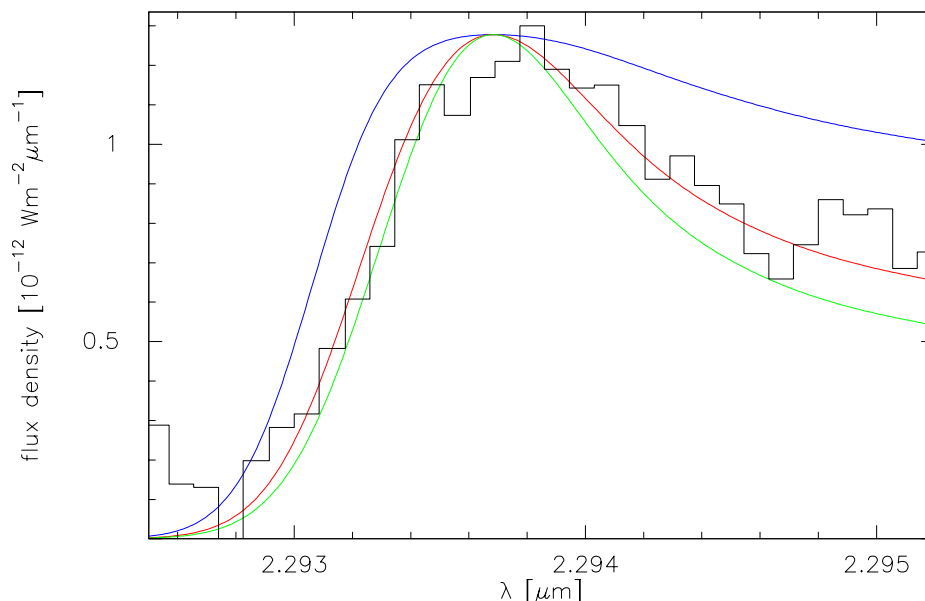


**Figure 5.9:** Calculated CO band emission spectra for a gaussian line profile with  $v_{\text{gauss}} \sim 50$  km/s. The CO column density used for the different spectra is  $2 \cdot 10^{21} \text{ cm}^{-2}$  (blue line),  $5 \cdot 10^{20} \text{ cm}^{-2}$  (red line) and  $10^{20} \text{ cm}^{-2}$  (green line).

The second characteristic feature is the broadening of the band head structure with increasing column density, especially at the long wavelength side. In Figure 5.9 the observed  $(2 \rightarrow 0)$  band head region (histogram) is overlaid on the normalized theoretical spectra with column densities of  $2 \cdot 10^{21} \text{ cm}^{-2}$  (blue line),  $5 \cdot 10^{20} \text{ cm}^{-2}$  (red line), and  $10^{20} \text{ cm}^{-2}$  (optically thin case, green line).

The spectrum with  $N_{\text{CO}} = 2 \cdot 10^{21} \text{ cm}^{-2}$  can immediately be excluded, but at first glance, it seems that the observations might also be fitted by optically thin emission. To make a decision whether the CO bands are really optically thin we can take a look at a somewhat larger wavelength interval. The upper panel of Figure 5.10 contains the synthetic spectrum of optically thin emission which does no more seem to fit the data over this larger wavelength range, whereas a good agreement between calculation and observation is achieved for a CO column density of  $\sim 5 \cdot 10^{20} \text{ cm}^{-2}$  indicating a marginally optical thickness as can be seen in the lower panel of Figure 5.10. An additional point speaking against optically thin emission is that the flux density ratio of the bandheads is highest for the optical thin case. Although the observations in the region around the  $(3 \rightarrow 1)$  band head are not excellent, a big mistake can almost certainly be excluded, so that such a large flux density ratio cannot be confirmed by the observations.

We therefore take  $N_{\text{CO}} = 5 \cdot 10^{20} \text{ cm}^{-2}$  as the best fit CO column density. The synthetic spectra of the  $(2 \rightarrow 0)$  band head we get, look very similar for temperatures in the range of 3000 – 5000 K. For a more sensitive limitation of the temperature range we must take into account the  $(3 \rightarrow 1)$  band head (see Fig. 5.6). This leads to the conclusion that  $T_{\text{CO}} = 3500 - 4000$  K. Unfortunately, an exact determination of the CO temperature fails because the higher band heads are not available within our high resolution spectrum.

With the derived values for column density and temperature we model the synthetic CO band spectrum for the complete wavelength range of the high resolution spectrum, taking into account the foreground extinction,  $A_V^{\text{ISM}}$ . Table 5.1 summarizes the parameters used, and our best fit is shown in the upper panel of Figure 5.11. The small box contains a blow-up of the  $(2 \rightarrow 0)$  band

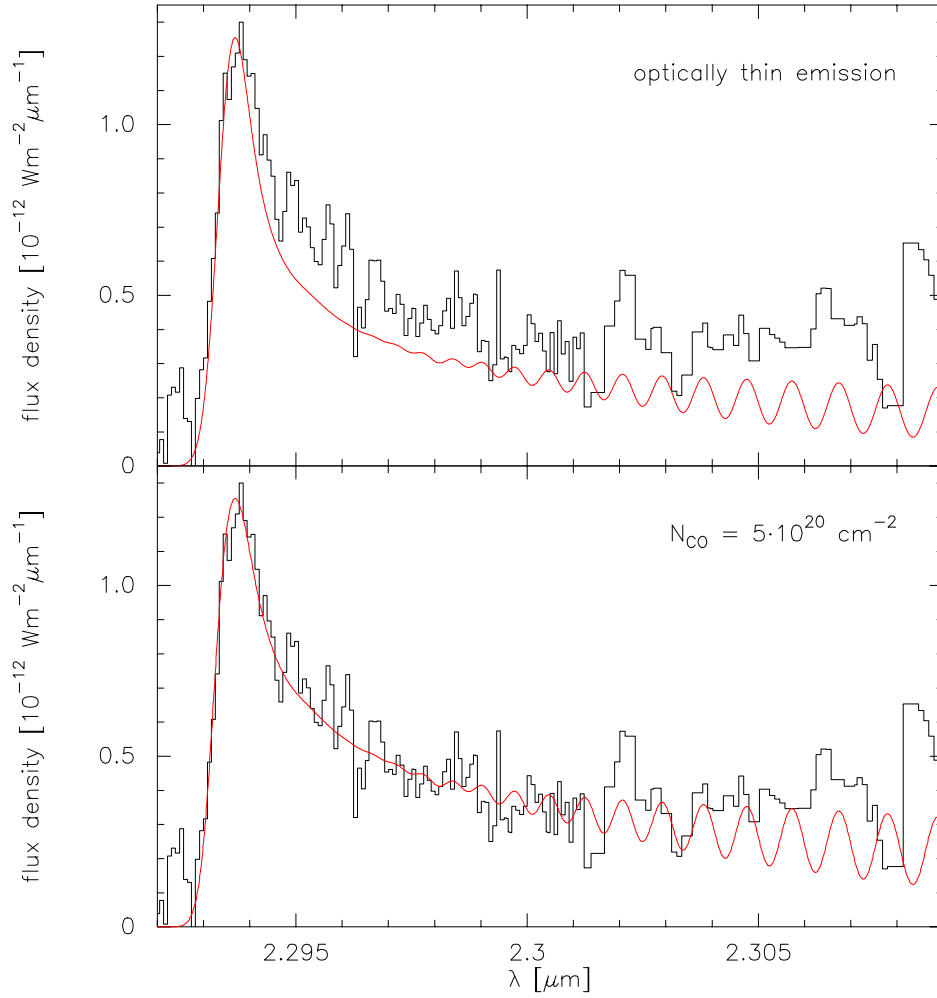


**Figure 5.10:** Comparison between theoretical ( $2 \rightarrow 0$ ) band head spectra of optically thin (upper panel) and marginally optically thick emission (lower panel). In both cases, the temperature is 3500 K. The theoretical spectrum obtained in the optically thin case clearly underestimates the emission at wavelengths longwards of the ( $2 \rightarrow 0$ ) band head.

head region pointing out the good agreement between observation and model.

The lower panel of Fig. 5.11 shows the residue of observed minus calculated spectrum. Some remaining features may result from observational uncertainties (indicated as dashed parts), for example the dip around  $2.3225 \mu\text{m}$  and the region around  $2.314 \mu\text{m}$ , whereas the features at  $2.3253$  and  $2.3084 \mu\text{m}$  seem to be yet unidentified emission lines.

For a distance to MWC 349 of 1.2 kpc we find a CO emission area projected on the sky of

**Table 5.1:** Parameters for CO used for the calculations shown in Fig. 5.11.  $A_{\text{V}}^{\text{ISM}}$  denotes the foreground extinction,  $A_{\text{CO}}$  and  $M_{\text{CO}}$  are the emitting CO area projected to the sky and the mass of CO derived from the fit, respectively.

$N_{\text{CO}}$ [ $\text{cm}^{-2}$ ]	$T_{\text{CO}}$ [K]	$v_{\text{gauss}}$ [km/s]	$A_{\text{V}}^{\text{ISM}}$ [mag]	$A_{\text{CO}}$ [ $\text{cm}^2$ ]	$M_{\text{CO}}$ [g]
$5 \cdot 10^{20}$	3500	$\sim 50$	8	$1.13 \cdot 10^{26}$	$2.6 \cdot 10^{24}$

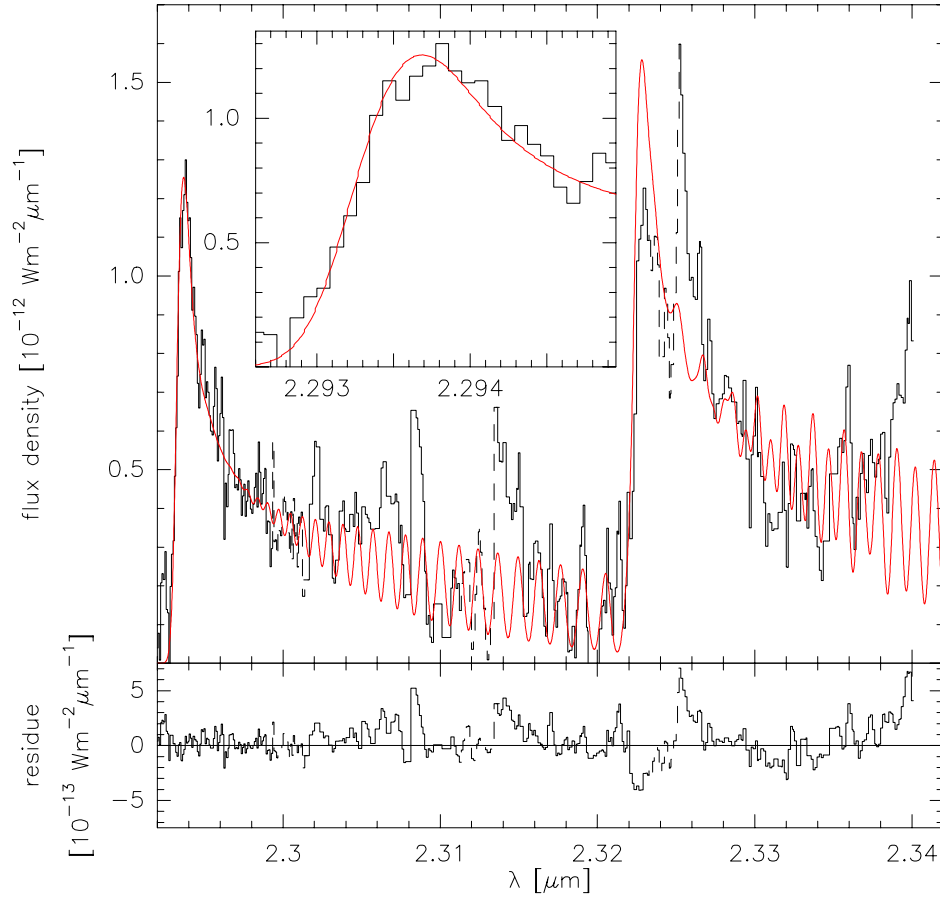


**Figure 5.11:** *Upper panel:* Modeled CO band emission (red line) for a temperature of  $T_{\text{CO}} = 3500$  K and a gaussian velocity of  $\sim 50$  km/s overlaid on the observations (histogram). The model parameters are given in Table 5.1. The insert shows a blow-up of the  $(2 \rightarrow 0)$  band head region pointing out the good agreement between observation and model. *Lower panel:* Residue of observations minus model. Some yet unidentified emission lines seem to be present.

$A_{\text{CO}} \simeq 1.13 \cdot 10^{26} \text{ cm}^2$  and a mass of  $M_{\text{CO}} \simeq 2.6 \cdot 10^{24} \text{ g}$ . Our  $A_{\text{CO}}$  is about 4.5 times larger than the value of  $2.5 \cdot 10^{25} \text{ cm}^2$  found by Geballe & Persson (1987) who could only derive a lower limit.

### 5.2.2 CO bands from a Keplerian rotating disk

As we have already mentioned in an earlier chapter, the existence of a circumstellar disk around MWC 349 is quite sure. Therefore we next investigate whether the CO bands can alternatively be explained by emission from this disk.

The disk around MWC 349 is assumed to rotate in a Keplerian fashion (see Chapter 2.1), therefore the rotational velocity at radial distance  $r$  from the star of mass  $M_*$  is given by

$$v_{\text{rot}} = \sqrt{\frac{GM_*}{r}} \quad (5.13)$$

where  $G$  is the gravitational constant. The line of sight velocity,  $v_{\text{los}}$ , i.e. the velocity component in the direction to the observer, for a disk with an inclination angle  $i$  towards the line of sight, and in the presence of a radial velocity of the star plus disk system,  $v_{\text{lsr}}$ , is

$$v_{\text{los}} = v_{\text{rot}} \cdot \sin \varphi \cdot \cos i + v_{\text{lsr}} . \quad (5.14)$$

For demonstration we first neglect any inclination and local standard of rest velocity. Then,  $v_{\text{lsr}}$  reduces to  $v_{\text{rot}} \cdot \sin \varphi$  (see Figure 5.12).

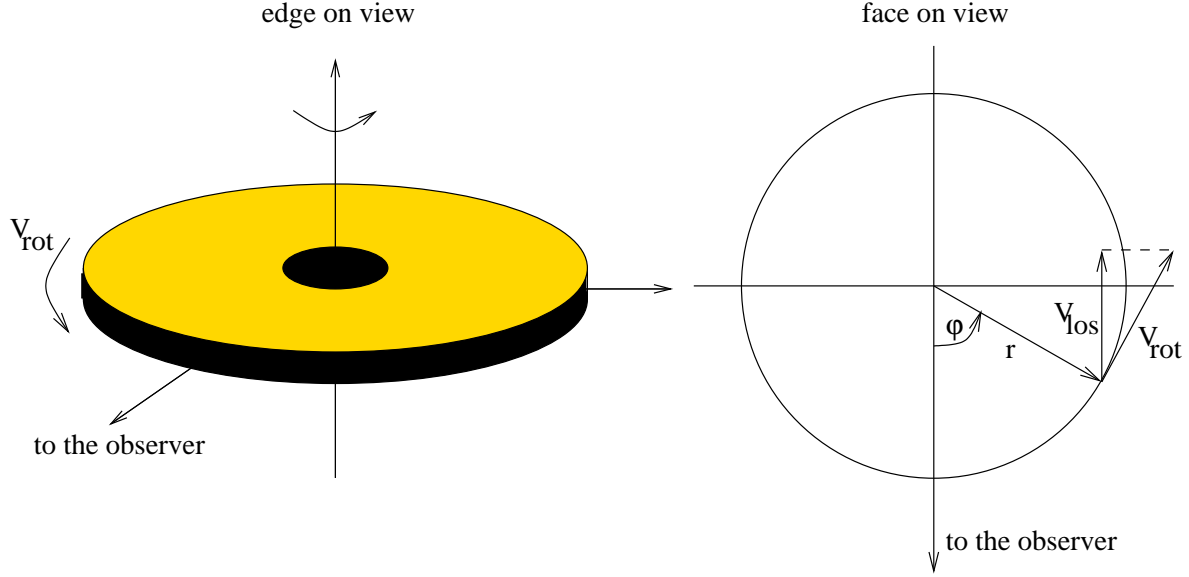


**Figure 5.12:** Sketch of the rotating disk seen edge on (left panel) and face on (right panel). Also indicated is the resulting line of sight velocity,  $v_{\text{los}}$ .

In addition we start by calculating the optically thin emission from infinitesimal narrow rings. The resulting profile of the band head emission smoothed to the spectral resolution of 15 km/s is plotted in Figure 5.13. The orbital velocity of the individual rings thereby drops from 60 km/s which is the maximum rotational velocity component we could derive from Figure 5.5 to 0 km/s.

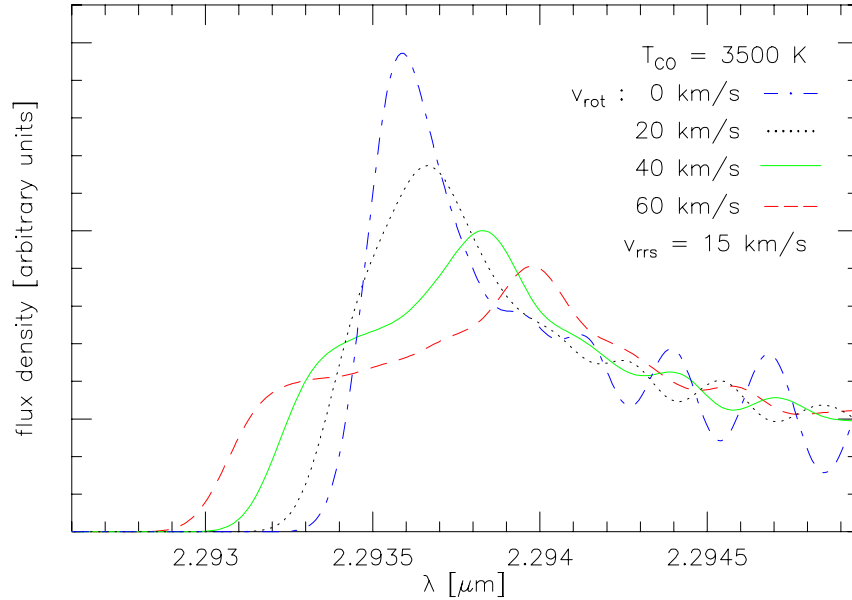


**Figure 5.13:** Optically thin CO band emission from rings of constant rotational velocity,  $v_{\text{rot}} = 60, 40, 20$  and 0 km/s and for an inclination angle of  $i = 0^\circ$ .



With increasing orbital velocity two characteristic features appear in the band head spectrum: a ‘shoulder’ to shorter and a maximum to longer wavelengths than the one of the unbroadened band head. The distance between shoulder and maximum increases with increasing  $v_{\text{rot}}$  because their wavelengths reflect the maximum and minimum shift of  $\lambda_0$  (see Equation (5.3)). The observed band head spectrum shows no characteristic shoulder, and we next try to let this shoulder disappear by integrating over a disk, using the radiation transfer equation (Eq. (5.11)) to take into account optical depth effects. Since the rotation strongly influences the shape of the band head, we mainly restrict our investigations of rotational broadening to the band head region.

To calculate the emission from the nearly edge on gaseous disk, we choose the maximum rotational velocity of  $v_{\text{rot}} \simeq 60$  km/s, which we get from Figure 5.5 for a vanishing wind velocity, as the velocity at the inner radius,  $r_i$ , of the disk. For the temperature and surface density along the disk radius we take power laws of the form

$$T(r) = T_i \cdot \left(\frac{r}{r_i}\right)^{-p} = T_i \cdot \left(\frac{v}{v_i}\right)^{2p} \quad (5.15)$$

and

$$\Sigma(r) = \Sigma_i \cdot \left(\frac{r}{r_i}\right)^{-q} = \Sigma_i \cdot \left(\frac{v}{v_i}\right)^{2q}, \quad (5.16)$$

respectively. For the right hand sides of the Eqs. (5.15) and (5.16) we used the Kepler law (Eq. (5.13)). We further fix the constant  $T_i$  to 5000 K which is the dissociation limit for CO molecules, and the inclination angle of the disk,  $i$ , to the observed value of about  $10^\circ$  which was also found from the dust disk modeling (see Table 3.6 in Chapter 3.3). Then, our free parameters are  $\Sigma_i$ , the exponents  $p$  and  $q$ , and the velocity at the outer radius. In addition we assume the CO disk to be geometrically flat, so that along each line of sight through the inclined disk, the density and temperature can be taken as constant; Eq. (5.16) therefore reflects the column density distribution  $N_{\text{CO}}(r) = \Sigma(r)/\sin i$ .

The emission from Keplerian rotating disks with regard to the influences of the free parameters on the band head structure are presented in Figure 5.14. The spectra are normalized to emphasize the differences. The first panel shows the theoretical band head spectra for disks with different column densities at the inner edge,  $N_i$ , and of constant disk size, which is fixed by the velocities at the inner and outer edge. The emission at the long wavelength side increases with column density because of the increasing optical depth. At wavelengths shorter than the band head the emission slowly decreases and the characteristic shoulder vanishes. The onset of the spectrum, however, happens at the same minimum wavelength which guarantees the broad band head structure.

When we keep the column density at the inner edge fixed, as shown in the second panel, and enlarge the size of the disk, the shape of the band head structure becomes narrower and loses its characteristic shoulder because of the influence of the larger emitting area for the smaller rotational velocity components. At the same time the onset of the spectrum slowly shifts to longer wavelengths which also shows that the highest rotational components become less significant. Our criterion of the minimum wavelength (Eq. 5.6) can therefore only hold for small disks, i.e. disks whose maximum rotational component is still significant in forming the band head shape.

In the third panel the exponent of the column density distribution is varied. Although with increasing  $q$  the column density drops drastically from the inner to the outer edge, the shape of the band head changes only slightly. The same can be said about the exponent  $p$  of the temperature distribution (last panel). Here, the band head maintains its shape; a deviation is hardly visible.

From the discussion of the free parameters we can conclude that the most important changes in the band head shape can be expected from the choice of the column density at the inner edge and from the disk size (for a fixed velocity  $v_i$ ), i.e. the velocity at the outer edge,  $v_o$ , whereas the total intensity that also has to be fitted depends on all free parameters. So we now have to care about the flux density emitted from these Keplerian disks.

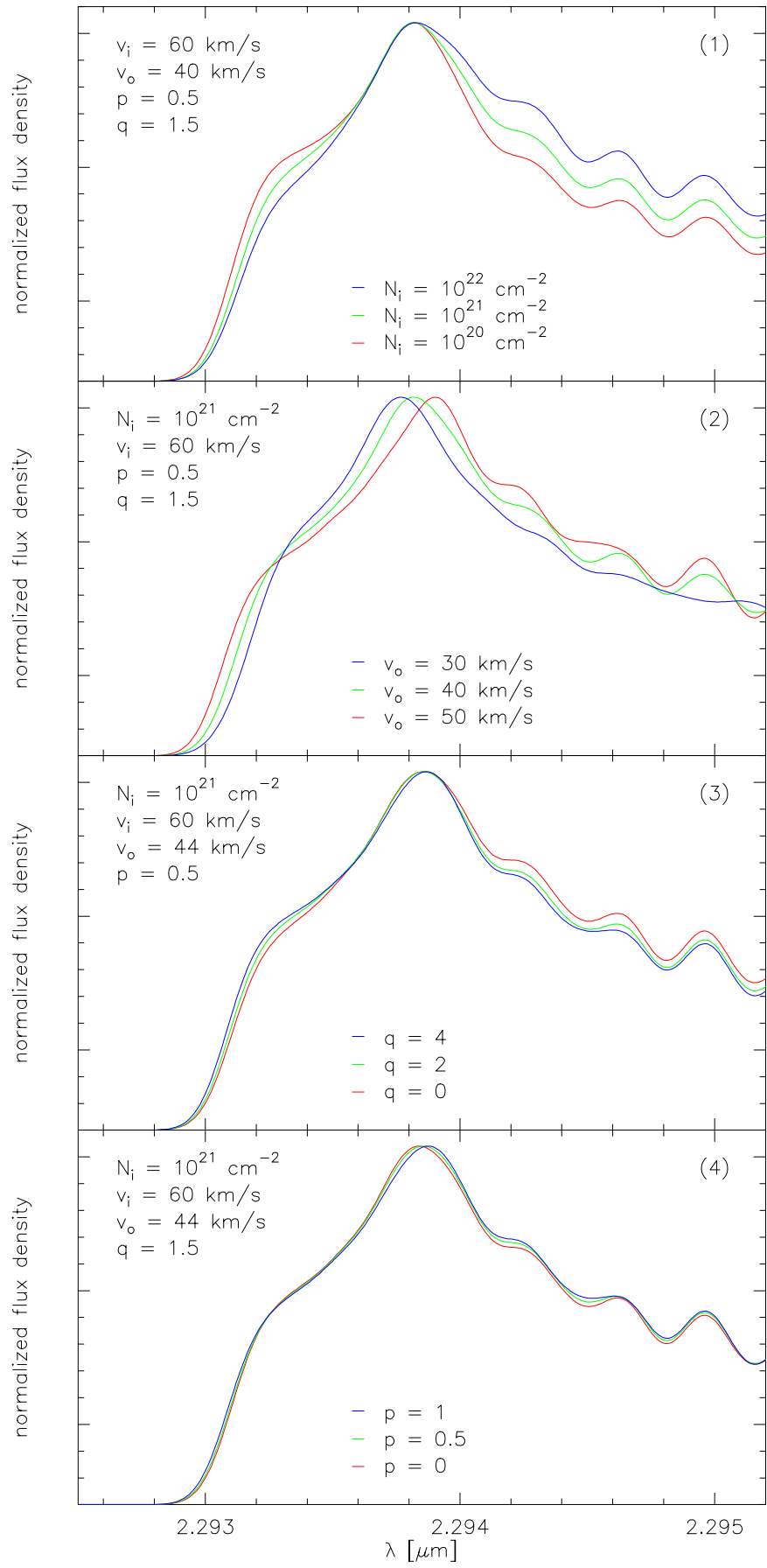


**Figure 5.14:** Emission from Keplerian rotating CO disks. The parameters for the velocities, the temperature and the density distribution for the model calculations are written within each panel.

For the integration along the disk radius we divide the disk in several rings of constant temperature and column density. The area of each ring is parametrized using the relation between radius and velocity given by Equation (5.13) for the Keplerian rotation. Each ring area can then be calculated by the following expression

$$A_n^{\text{ring}} = \sin i \cdot \pi r_i^2 \left( \frac{v_i}{v_{o,n-1}} \right)^4 \left[ \left( \frac{v_{i,n}}{v_{o,n}} \right)^4 - 1 \right], \quad (5.17)$$

and these ring areas are *independent of the stellar mass*. Here,  $v_{i,n}$  and  $v_{o,n}$  are the velocities at the inner and outer edge of the  $n$ -th ring, and  $v_i$  is the velocity at the inner edge of the first ring which is also the inner edge of the disk,  $r_i$ . For a given velocity interval from the inner to the outer edge of the disk, we find from Eq. (5.17) that the fitting parameter for the total CO emission is simply  $r_i^2$ . This information, together with the velocity at the inner edge,  $v_i$ , which is the input parameter, results in the determination of the stellar mass  $M_*$  according to the Kepler law. Since we already know the mass of MWC 349 which should be about  $26 M_\odot$ , we can choose the other way round and try to determine the outer radius of the disk.

In the ongoing calculations we make the following assumptions. Since the exponents of the temperature and column density distributions play only a minor role for the band head shape, we fix them following Hayashi (1981) at  $p = 0.5$  and  $q = 1.5$ . These numbers coincide on the whole with the values we found for the dust disk (see Table 3.6 of Chapter 3.3). The disk models then contain only two free parameters: the velocity at the outer radius,  $v_o = v(r_o)$ , and the column density at the inner edge,  $N_i$ . From the parameter discussion (Figure 5.14) we know that for the explanation of the observed band head profile one needs a large spread in the rotational velocity because otherwise one cannot suppress the shoulder. The large velocity spread implies a large emitting area, and therefore a low column density. In our test calculations it turned out that the velocity at the outer edge must lie in the range between 30 km/s and 40 km/s. If  $v_o$  is higher, the shoulder of the band head becomes too broad, if it is smaller, the profile gets too narrow.

Our best models of a rotating disk are presented in Figure 5.15 and the parameters used are summarized in Table 5.2. These fits are, however, not at all satisfactory. All the synthetic disks we

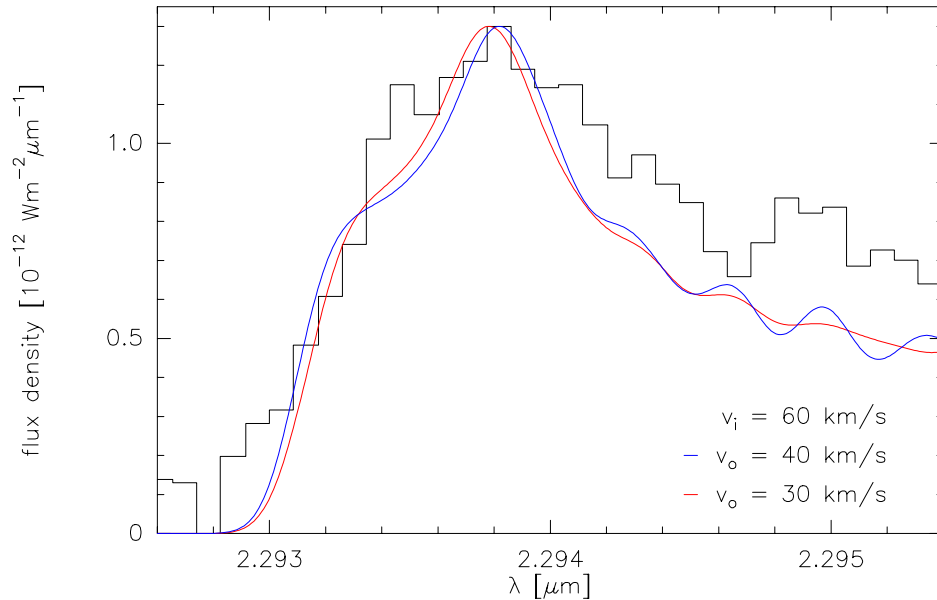


**Figure 5.15:** Best fit of Keplerian rotating disks to the observed ( $2 \rightarrow 0$ ) band head. The model parameters are summarized in Table 5.2.

**Table 5.2:** Parameters for the fit of the CO disk calculations shown in Fig. 5.15. Fixed parameters are the mass of  $26 M_{\odot}$ ,  $T_i = 5000$  K,  $p = 0.5$ ,  $q = 1.5$ ,  $i = 10^\circ$ , and  $v_i = 60$  km/s which leads to  $r_i \simeq 6.4$  AU.

$v_o$ [km/s]	$r_o$ [AU]	$T(r_o)$ [K]	$N_{\text{CO}}(r_i)$ [cm $^{-2}$ ]	$N_{\text{CO}}(r_o)$ [cm $^{-2}$ ]
40	14.4	3333	$8.5 \cdot 10^{16}$	$2.5 \cdot 10^{16}$
30	25.6	2500	$5.8 \cdot 10^{16}$	$7.3 \cdot 10^{15}$

calculated show a common feature: The rise of the band head structure at the short wavelength side is much steeper in the calculated spectra than in the observations. This wavelength part can therefore not be fitted well. In addition, on the long wavelength end of the spectrum, the model calculations clearly *underestimate* the observed flux density. This fact follows from the very low column density at the inner edge of the disk,  $N_{\text{CO}}(r_i)$ , (see Table 5.2) which is needed to not *overestimate* the total observed flux density. Therefore, the emission of these theoretical Kepler disks is optically thin, which was found in Chapter 5.2.1 not to be true.

### 5.2.3 Keplerian rotation plus gaussian component

Up to now we have only looked at the two extreme cases, namely pure gaussian line profile and pure rotation. From Figure 5.5 it follows, however, that each combination of the two broadening mechanisms that falls into the indicated range which is determined by  $\lambda_{\text{min}}$ , is allowed. So we now turn to this intermediate case: We combine a constant rotational velocity,  $v_{\text{rot}}$ , with a gaussian velocity component,  $v_{\text{gauss}}$ . For a given rotational velocity, the gaussian one is calculated according to Eq. (5.6). The CO column density,  $N_{\text{CO}}$ , we keep constant and fix it at  $5 \cdot 10^{20} \text{ cm}^{-2}$  which was the best value found from the pure gaussian fit (Table 5.1). Figure 5.16 contains synthetic

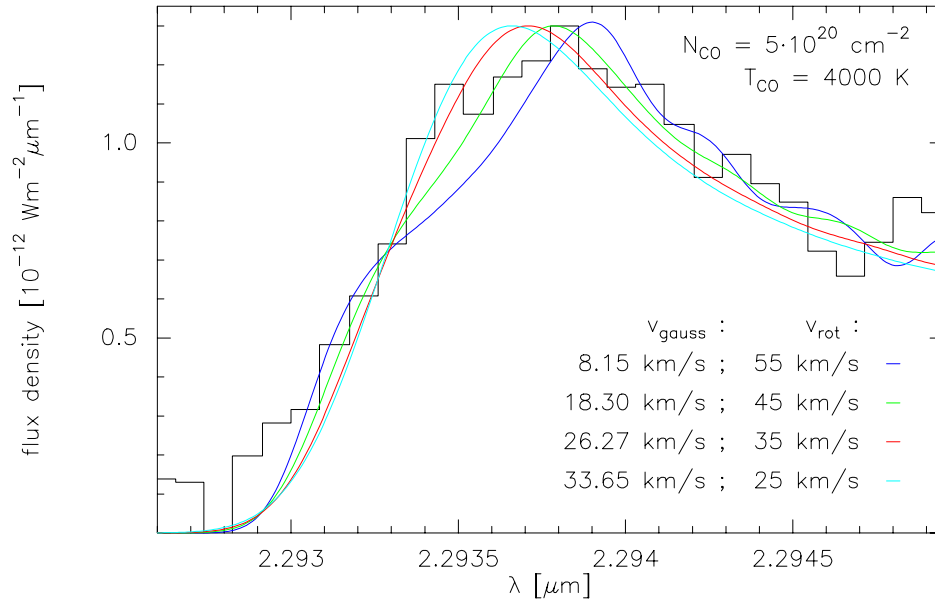


**Figure 5.16:** Combination of rotation and a gaussian velocity component. The respective velocities are listed within the Figure.

spectra calculated for profile functions of the CO gas that consist of a constant rotational velocity (decreasing from 55 km/s to 25 km/s) and the corresponding gaussian velocity, overlaid on the observed ( $2 \rightarrow 0$ ) band head.

As the rotational velocity approaches the value of the gaussian one, the characteristics of the band head which are caused by the rotation (especially the blue-shifted shoulder) disappear in favour of the pure gaussian shape of the band head spectrum. Thus, one single rotational component of the medium with a velocity smaller than  $\sim 35$  km/s can hardly be recognized in these data and for the moment cannot be excluded.

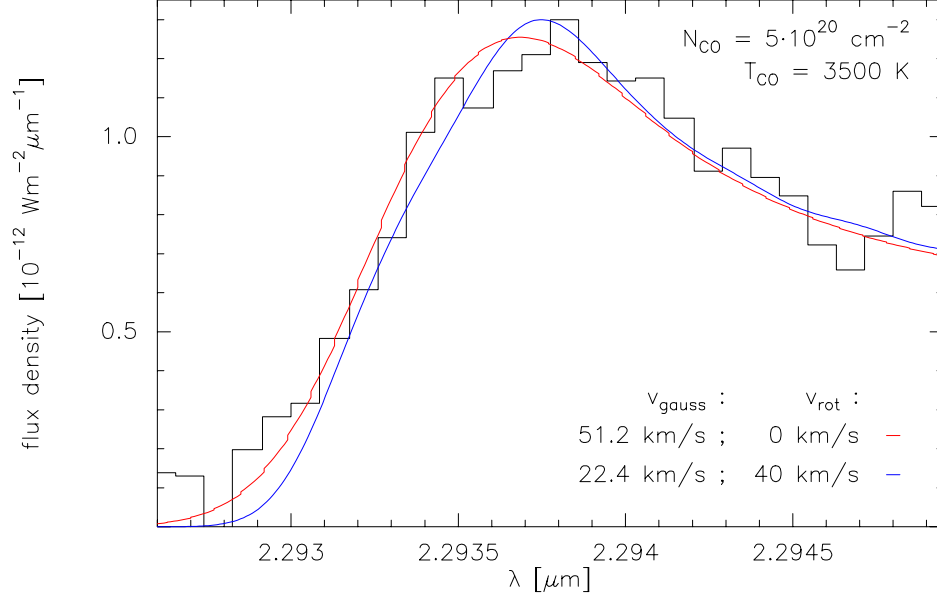


**Figure 5.17:** Best fits to the observed ( $2 \rightarrow 0$ ) band head. The red line represents the pure gaussian fit of Figure 5.11 and the blue line shows the combination of a rotational and a gaussian velocity component whose velocities are determined according to Eq. 5.6.

**Table 5.3:** Parameters for CO used for the calculations shown in Fig. 5.17.  $A_V^{\text{ISM}}$  denotes the foreground extinction,  $A_{\text{CO}}$  and  $M_{\text{CO}}$  are the emitting CO area projected to the sky and the mass of CO derived from the fit. For comparison, the first row repeats the old results of the fit with a pure gaussian velocity component.

$N_{\text{CO}}$ [cm <sup>-2</sup> ]	$T_{\text{CO}}$ [K]	$v_{\text{gauss}}$ [km/s]	$v_{\text{rot}}$ [km/s]	$A_V^{\text{ISM}}$ [mag]	$A_{\text{CO}}$ [cm <sup>2</sup> ]	$M_{\text{CO}}$ [g]
$5 \cdot 10^{20}$	3500	51.2	—	8	$1.13 \cdot 10^{26}$	$2.63 \cdot 10^{24}$
$5 \cdot 10^{20}$	3500	22.4	40	8	$1.07 \cdot 10^{26}$	$2.49 \cdot 10^{24}$

Nevertheless we get a reasonable fit for a rotational velocity of  $\sim 40$  km/s which is shown as the blue curve of Figure 5.17. In the same Figure we also plotted for comparison our best fit for a pure gaussian velocity component (red curve) taken from Figure 5.11. The parameters for both models are summarized in Table 5.3. At this state we are not able to decide which of these curves best fits the data.



# Chapter 6

## Discussion

By modeling the observations we found that the CO gas emitting the first overtone bands has to have the following properties:

- it is in LTE
- it has a velocity dispersion of 50 – 60 km/s
- its column density is of order  $\sim 5 \cdot 10^{20} \text{ cm}^{-2}$
- it possesses a temperature of 3500 – 4000 K.

Without investigating the astronomical plausibility, we presented two mathematically possible scenarios (see Fig. 5.17) that led to reasonable fits of the observational data: a) The combination of rotation with fairly constant velocity plus a gaussian component; and b) a pure gaussian velocity component. Whether we find for one of these models a reasonable circumstellar region within which the hot and dense CO gas might be located is subject to the following discussion.

### a) The disk and its emanating wind

For the first model we assume the following scenario which is shown as a sketch in Figure 6.1: The CO gas takes part of the Keplerian rotation of the disk, thereby emanating from the disk as a disk wind. Such a theoretical scenario has recently been discussed in more detail by Hollenbach et al. (1994). In addition, in the case of MWC 349 we know from the observations of the H92 $\alpha$  line that the observed kinematical signature of this line can also only be explained by a combination of bipolar outflow and rotation (Rodríguez & Bastian 1994). But when we want to explain the CO emission by such a scenario, we are immediately confronted with the following inconsistencies:

The maximum possible rotational velocity of  $v_{\text{rot}} \simeq 40 \text{ km/s}$  we found for the CO gas implies for a stellar mass of  $26 M_{\odot}$  a distance of about 14.4 AU. It is, however, very unlikely that the gas can achieve the required temperature of  $\sim 3500 \text{ K}$  so far from the star. Our model of the dust disk indicates that at 14.4 AU the grains are at 985 K. In view of the high densities, gas and dust should be thermally coupled.

Another problem is the CO column density of  $5 \cdot 10^{20} \text{ cm}^{-2}$  needed for the optical depth effects. Using standard conversion factors ( $\Sigma_{\text{dust}} : \Sigma_{\text{H}} \simeq 10^{-2}$ ,  $N_{\text{CO}} : N_{\text{H}} \simeq 10^{-4}$ ), the surface density of the dust disk model implies at 14.4 AU a CO column density  $N_{\text{CO}} \simeq 2 \cdot 10^{19} \text{ cm}^{-2}$  which is 25 times too small.

But the most striking disagreement with this model is the CO emitting area of only  $1.07 \cdot 10^{26} \text{ cm}^2$  (see Table 5.3). It implies that the radial extension of the CO gas, i.e. the thickness of the CO ring must be smaller than  $\Delta r = A_{\text{CO}} / (2\pi r \sin i) \simeq 4.55 \cdot 10^{11} \text{ cm} = 0.03 \text{ AU}$ . The existence of only a narrow ring of hot and dense CO gas seems, however, not to be realistically, for one might ask

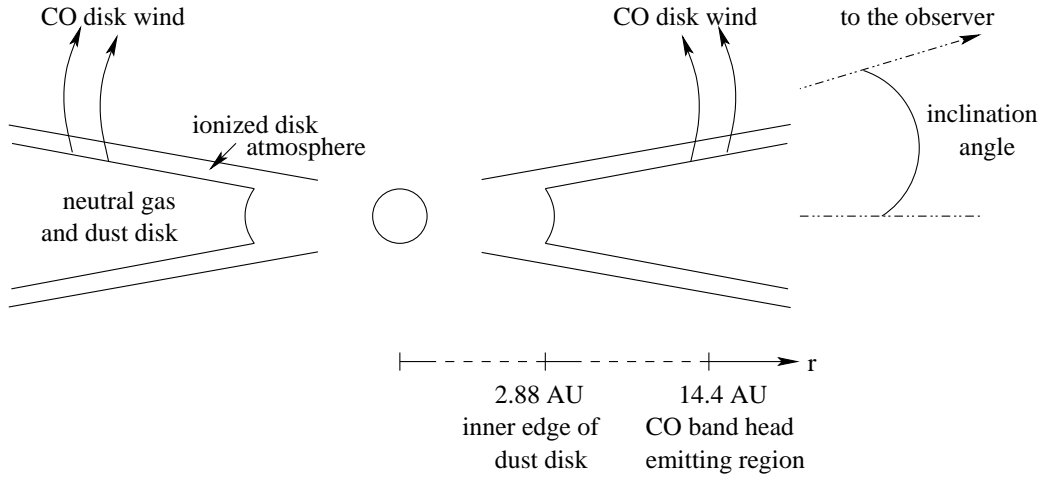


**Figure 6.1:** Sketch of the location of the CO first overtone band emitting gas. The CO is assumed to take part on the rotation within the Keplerian disk, thereby emanating from the disk as a disk wind.

why the neighbouring regions of comparable conditions do not emit the CO bands, or, the other way round, why should there be no CO at comparable temperature and density conditions in the neighbouring regions.

We have only taken into account the maximum possible rotational velocity. The choice of a lower  $v_{\text{rot}}$  would make things even worse. We conclude that this first model can almost certainly be discarded.

## b) The wind model

For the second model, a pure gaussian line profile with  $v \simeq 50$  km/s, we use the results found from modeling the Pfund line emission, and assume that the CO gas is also located within the spherical wind zone (Figure 6.2). Then, with the emission area of  $1.13 \cdot 10^{26} \text{ cm}^2$  we get from the CO fit (Table 5.3), the radius of the ‘CO wind’ can be determined; it is of order  $r_{\text{CO}} = \sqrt{A_{\text{CO}}/\pi} \simeq 6 \cdot 10^{12} \text{ cm} = 86 R_{\odot}$  which roughly coincides with the inner radius of the ionized wind. The latter was found to be  $\sim 100 R_{\odot}$  to account for the continuum emission in the visible and UV range of the total spectrum (see Figure 3.10). There, the gas temperature is  $\sim 9000 \text{ K}$  which is about twice the

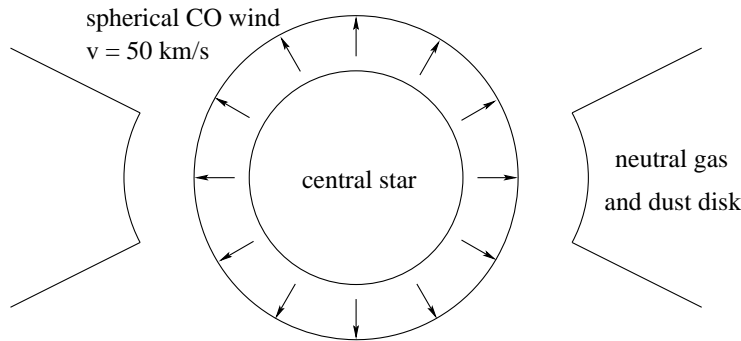


**Figure 6.2:** Sketch of the location of the CO first overtone band emitting gas. The CO emission is assumed to arise in the spherical symmetric stellar wind with constant wind velocity of  $v_{\text{wind}} \simeq 50$  km/s leading to a nearly gaussian shape of the individual lines.



dissociation temperature of CO! Therefore, we are quite sure that no CO molecules can exist within this region. Although the probability that the CO bands arise in the stellar wind tends to be zero, it is remarkable that gaussian line profiles of the same width as the Pfund lines give the best fit.

It seems that we are able to reproduce the shape of the band head, but we still lack the physical interpretation of the model calculations. A possible expedient might be the scenario recently proposed by Mitskevich (1995a,b). He suggests that the dust within the circumstellar environment around young stars is concentrated in clouds rather than in a homogeneous thin dust disk, and that these clouds are arranged in a disk-like structure. If we assume the CO gas to be also concentrated in several high density clumps that are distributed in such a cloudy dust structure, the disagreement between our model calculations and the physical interpretation might become less strange. But this scenario is rather speculative and detailed calculations should be carried out first before one can draw any conclusions.

There exists, however, another alternative we have not yet mentioned and which finally will be discussed:

### c) The partially hidden inner edge of the Keplerian rotating disk

Since the existence of the circumstellar gas and dust disk is well established by the observations and since we know from other objects that the CO band emission is a good tracer of the inner edge

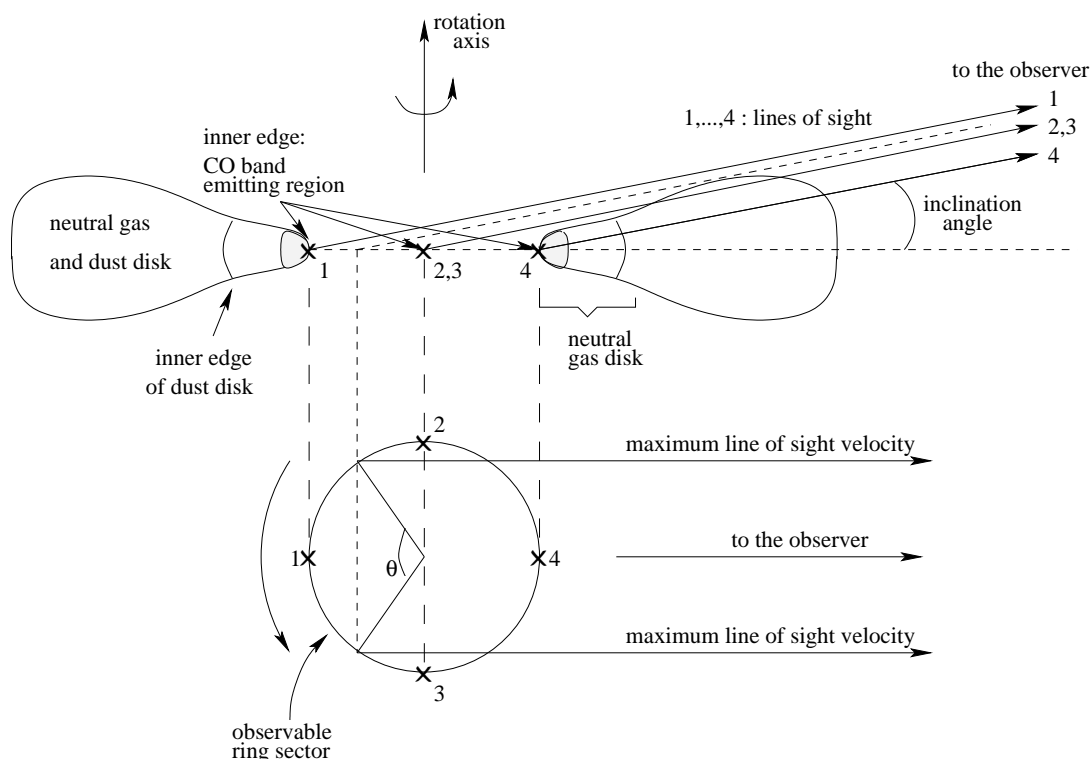


**Figure 6.3:** Sketch of the disk around MWC 349 seen edge on. Because of the small inclination angle, only emission from sector 1 where the radial velocity is small will reach the observer. Light from other places, for example, from the points marked 2, 3, and 4 is absorbed by the bulge.

of the circumstellar disk (see Table 1.2 and Kraus 1997), we come back to the disk as the most probable location of the hot and dense CO gas.

If the CO band emission arises in this disk, it must come from regions where the temperature can reach  $\sim 3500$  K, so the dust is already evaporated and only the neutral gas disk extends to smaller radii. Furthermore, the CO column density has to be about  $5 \cdot 10^{20} \text{ cm}^{-2}$ . Using again our model of the dust disk as a guide, the distance to the star is then  $\sim 2.4$  AU and the associated Kepler velocity  $v_{\text{rot}} \sim 98$  km/s. To avoid the problems with the line profile in case of such a high rotational velocity, as discussed in Chapter 5.2.2 and demonstrated in Figure 5.13, we tentatively propose a configuration as depicted in Figure 6.3. The disk has a bulge and because of its small inclination angle  $i \sim 10^\circ$ , it blocks the light from the inner edge of the disk on the near side to the observer. We therefore receive emission only from sector 1 in Figure 6.3 where the *radial* velocity is low.

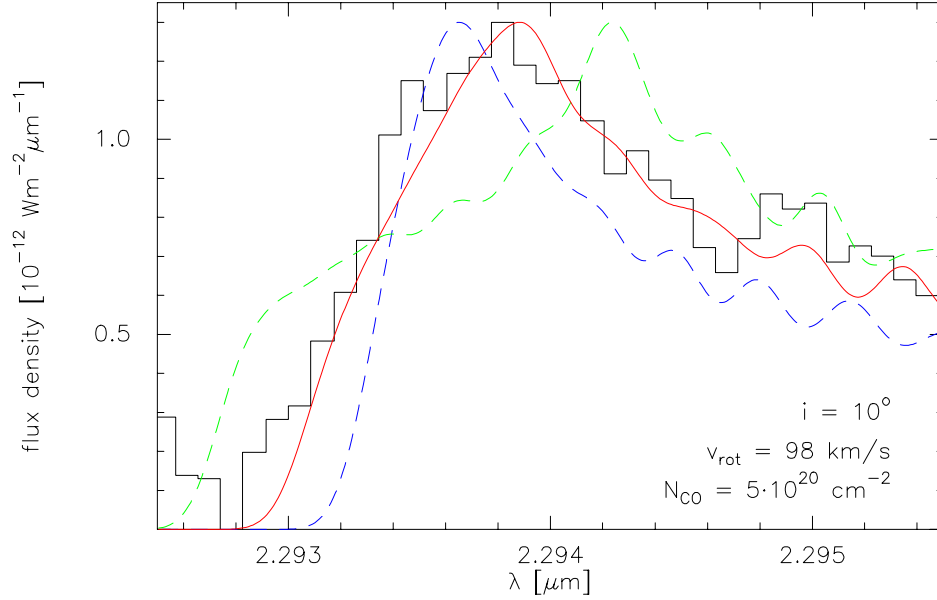


**Figure 6.4:** Fit to the observed  $(2 \rightarrow 0)$  band head for ring segments with a Keplerian velocity of  $v_{\text{rot}} = 98$  km/s. The angles and the corresponding velocity ranges are given in Table 6.1 and the best fit is shown by the solid red line.

**Table 6.1:** Angles  $\theta$  and velocity ranges  $v_{\text{rot,los}}$  for the calculated sectors shown in Figure 6.4. The inclination angle was taken as  $10^\circ$  and the rotational velocity is 98 km/s.

	$\theta [^\circ]$	$v_{\text{rot,los}} [\text{km/s}]$
green curve	180	$-96.5 \dots 96.5$
red curve	75	$-59.0 \dots 59.0$
blue curve	33	$-27.6 \dots 27.6$

We performed several test calculations keeping the column density constant  $N_{\text{CO}} = 5 \cdot 10^{20} \text{ cm}^{-2}$ , and the CO temperature fixed at 3 500 K. Only the emission from sector 1 is calculated which means that the remaining CO emission must be totally absorbed by the veiling disk bulge. This is, however, only a rough approximation to the possibly real absorbing behaviour of the disk, since normally

the density within the disk atmosphere is drastically decreased with scale height.

In Figure 6.4 we show computations of the flux received from sector 1 for different opening angles  $\theta$ . The ranges of radial velocities in the sectors are summarized in Table 6.1. Of course, the existence of the bulge is hypothetical as we have no information on the density structure of the circumstellar disk in  $z$ -direction, but it is suggestive that such a simple model gives an acceptable fit.

The only limitation of this picture we are aware of is the dissociation: if the CO molecules are located at the inner edge of the neutral gas disk, they are directly exposed to the Lyman continuum photons from the star and can therefore easily be dissociated. One possible mechanism to prevent CO from dissociation is the shielding by dust grains. This mechanism, however, can only work if enough dust is situated between the Lyman continuum photons and the CO molecules which is not the case at distances smaller than the evaporation radius of dust ( $r_{\text{evap}} \simeq 2.88 \text{ AU}$ ). The other possibility is self-shielding of the CO. This effect depends on the CO column density in direction to the destroying UV photons, and on the velocity dispersion of the CO gas (e.g. Bally & Langer 1982) and has to be checked more accurately during future more detailed calculations.



# Chapter 7

## Conclusions

In this thesis, new low and the first high resolution near infrared spectra of the peculiar B[e] star MWC 349 are presented. The wavelength interval  $2.285 - 2.342 \mu\text{m}$  of the high resolution spectrum contains mainly emission of the first overtone bands of the CO molecule as well as emission from several recombination lines of the Pfund series of atomic hydrogen.

For the discussion of the continuum emission, not only the wavelength range of the observations is taken into account, but the complete data that can be found in the literature. In each wavelength range a dominating emission mechanism can be modeled: In the radio part the continuum is produced by free-free emission from the electron-proton plasma in the ionized wind, whereas free-bound processes dominate the emission in the visible and ultraviolet spectral range, and a dust disk is responsible for the strong infrared excess.

The model calculations for the ionized wind zone indicate an overall temperature of  $\sim 9\,000\text{ K}$  which agrees with the value of  $8\,700 \pm 300\text{ K}$  derived from radio maps. The spectral index of  $\sim 0.6$  in the radio range is a hint for an electron density distribution of the form  $N_e \sim r^{-2}$ . Under the assumption of a spherical symmetric wind with constant mass loss rate, i.e. with constant wind velocity, the maximum electron density around MWC 349 is found to be  $\sim 10^{11}\text{ cm}^{-3}$ . This density corresponds to an inner radius of the wind zone of about  $100\text{ R}_\odot$ ; the outer radius must be larger than  $3\,000\text{ AU}$ .

For the dust emission, a MRN grain size distribution is assumed for the mixture of carbon grains and silicates. The emission from the nearly edge on ( $i \simeq 10^\circ$ ) dust disk is calculated with the following model parameters: At the inner radius,  $r_i = 2.88\text{ AU}$ , given as the evaporation distance of the dust particles, the temperature is fixed at  $2\,000\text{ K}$ . The temperature distribution along the disk radius as well as the surface density distribution are taken as power laws. They are found to behave as  $T(r) = 2\,000 \cdot (r/r_i)^{-0.44}\text{ K}$  and  $\Sigma(r) = 0.06 \cdot (r/r_i)^{-1.8}\text{ g cm}^{-2}$ . The outer radius of the dust disk is found to be about  $100\text{ AU}$  which also agrees with what has been observed. With these parameters a dust mass of  $\sim 1.65 \cdot 10^{-6}\text{ M}_\odot$  is derived.

Next, the level population of the recombining hydrogen atom is calculated and several mechanisms are presented which allow the number of the bound levels to be finite. For the computation of the Einstein coefficients of spontaneous emission, several approximational methods are presented. The values  $A_{n,5}$  of the Pfund series are found to follow a potential law for the Pfund lines of interest. The emission of the Pfund lines is modeled using Menzel's case B recombination theory, i.e. the emission is assumed to be optically thin. In addition, no deviation from LTE is found. The width of about  $50\text{ km/s}$  and the shape of their line profile agree well with what is expected from a spherical symmetric wind. But in contrast to the highest electron density of  $\sim 10^{11}\text{ cm}^{-3}$  found from the continuum emission, the Pfund lines indicate a maximum electron density of only  $\sim 10^9\text{ cm}^{-3}$ . This disagreement can, however, be eliminated by taking into account collisional depopulation of the hydrogen levels for densities larger than  $\sim 10^9\text{ cm}^{-3}$ .

Finally the first overtone band emission of the CO molecules is discussed. Because of the

suspected disk of the system, the kinematic information is of particular value. The width of the ( $2 \rightarrow 0$ ) band head indicates a velocity broadening of the order of  $50 - 60$  km/s, depending on the broadening mechanism. As rotation produces characteristic line profiles (see Figure 5.13), our detailed modeling rules out a purely Keplerian rotating CO disk. However, a rotational velocity component up to  $40$  km/s cannot be excluded.

The location of the hot CO gas producing the band emission is still uncertain. As well as the Pfund lines, the CO can best be fitted with a gaussian velocity component of  $\sim 50$  km/s. Further, the CO molecules are at a temperature of  $3500 - 4000$  K, the population of the vibrational levels must be close to LTE, and the CO column density equals about  $5 \cdot 10^{20} \text{ cm}^{-2}$ . The resulting CO lines are marginally optically thick, and the derived mass of the hot CO gas is  $\sim 3 \cdot 10^{24}$  g.

Several physical interpretations are discussed: (i) The CO gas might take part on the Keplerian rotation and emanating from the disk as a disk wind, and (ii) the CO might be located within the wind zone. Both models were found to show up to many inconsistencies. As an alternative it is proposed that the CO band emission might come from the inner edge of the circumstellar disk. Because of the high temperature and column density, the CO gas must be located closer to the star than the inner edge of the dust disk. If one extrapolates the model of the dust disk, which successfully explains the continuum emission from MWC349, towards the star, one finds that a column density of  $\sim 5 \cdot 10^{20} \text{ cm}^{-2}$  is achieved at a distance of  $2.4$  AU, corresponding to a Keplerian velocity of  $\sim 100$  km/s. If the disk has a bulge which absorbs the CO emission from its near part, as depicted in Figure 6.3, the observer sees only a sector on the far side of the rotating inner disk edge where the radial velocities are all smaller than  $\sim 60$  km/s. With such a geometrical configuration, a satisfactory fit is also possible (see Figure 6.4).

Instead of finding some answers to the open questions concerning the circumstellar conditions of MWC 349, we added one more unsolved problem to the list of peculiarities, namely the question where within its circumstellar environment the CO first overtone band emitting gas is located. Future observations and model calculations will hopefully help to come closer to the nature of the puzzling environment of this peculiar B[e] star MWC 349.

# Appendix A

## Calculation of the gaunt factors $g_{\text{ff}}$ and $g_{\text{fb}}$

To calculate the free-bound gaunt factors we used the formulae given by Brussard & van de Hulst (1962)

$$g_{\text{fb}}(\nu, T) = 2\Theta \sum_{n=m}^{\infty} g_n(\nu) \frac{e^{\Theta/n^2}}{n^3} \quad (\text{A.1})$$

with

$$\Theta = \frac{h\nu_0 Z^2}{kT} \quad \text{and} \quad m = Z \cdot \text{int} \left[ \sqrt{\frac{\nu_0}{\nu}} \right] + 1. \quad (\text{A.2})$$

$\nu_0$  is the ionization frequency of hydrogen from the ground level. The  $g_n(\nu)$  are the gaunt factors for transitions from the free levels  $E = -h\nu_0 Z^2/n^2 + h\nu$  to the bound levels  $E' = -h\nu_0 Z^2/n^2$ . We can derive from Fig. 8 of Brussard & van de Hulst (1962) that their values vary in the frequency range of our interest ( $10^9 - 10^{15}$  Hz) between 0.91 and 1.08 for frequencies in the visible and tend to converge against 1 for frequencies  $\nu < 0.04\nu_0 Z^2$ , i.e. for  $\lambda > 2.281 \mu\text{m}$  ( $Z = 1$ ). We adopt  $g_n = 1$  in all cases. This introduces errors in  $g_{\text{fb}}(\nu, T)$  of 10 – 20 %.

For the free-free gaunt factors, we used the expressions derived by Gronenschild & Mewe (1978). They are valid in the range  $10^{-2} < u = h\nu/kT < 10^3$ :

$$g_{\text{ff}}(\nu, T) = \sqrt{\left( \frac{\sqrt{3}}{\pi} e^x K_0(x) \right)^2 + (a - b \log u)^2} \quad (\text{A.3})$$

with

$$x = \frac{u}{2} \left( 1 + \sqrt{10\gamma^2} \right) \quad (\text{A.4})$$

$$\gamma^2 = Z^2 \frac{I_{\text{H}}}{kT} = 1.578 \cdot 10^5 \frac{Z^2}{T} \quad (\text{A.5})$$

$$a = 1.20 \cdot \exp \left[ - \left( \frac{\log \gamma^2 - 1}{3.7} \right)^2 \right] \quad (\text{A.6})$$

$$b = 0.37 \cdot \exp \left[ - \left( \frac{\log \gamma^2 + 1}{2} \right)^2 \right] \quad (\text{A.7})$$

$K_0$  is the modified Bessel function of the second kind.

In the long wavelength region there are several approximational methods and two of them we found to be the most commonly used ones. In Altenhoff et al. (1960) we found the expression

$$g_{\text{ff}}(\nu, T) = \frac{\sqrt{3}}{\pi} \cdot 21.67 T_e^{0.15} \cdot \nu^{-0.1} \quad (\text{A.8})$$

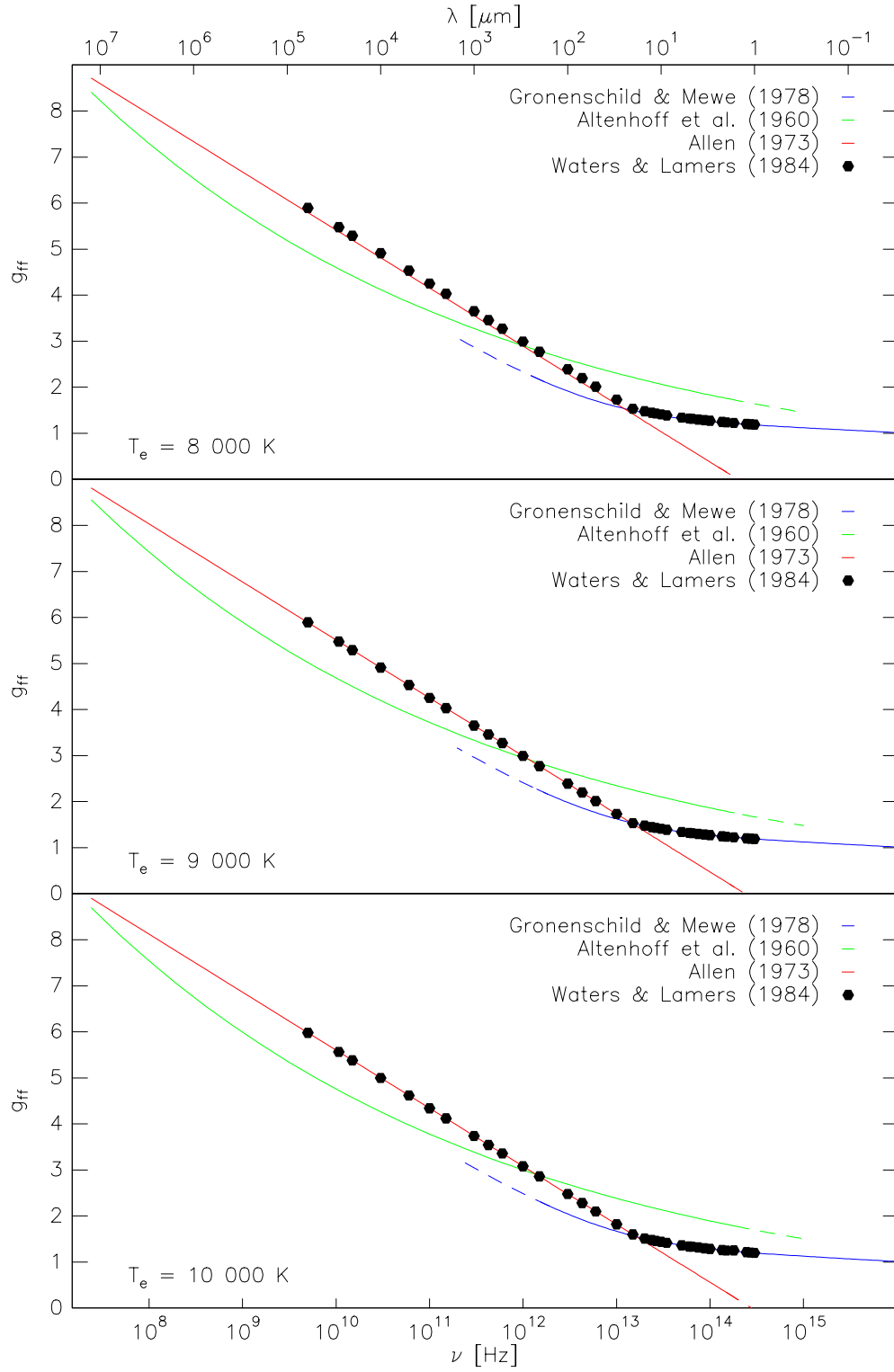


**Figure A.1:** Free-free gaunt factors for different electron temperatures. In the long wavelength region they were calculated with the expressions by Altenhoff et al. (1960) (green line) and Allen (1973) (red line). The blue line is calculated after Gronenschild & Mewe and represents the gaunt factors in the short wavelength region. The dashed parts in each line shows the region where the approximations are no more valid. For comparison, we have also plotted the data given by Waters & Lamers (1984) (black dots).



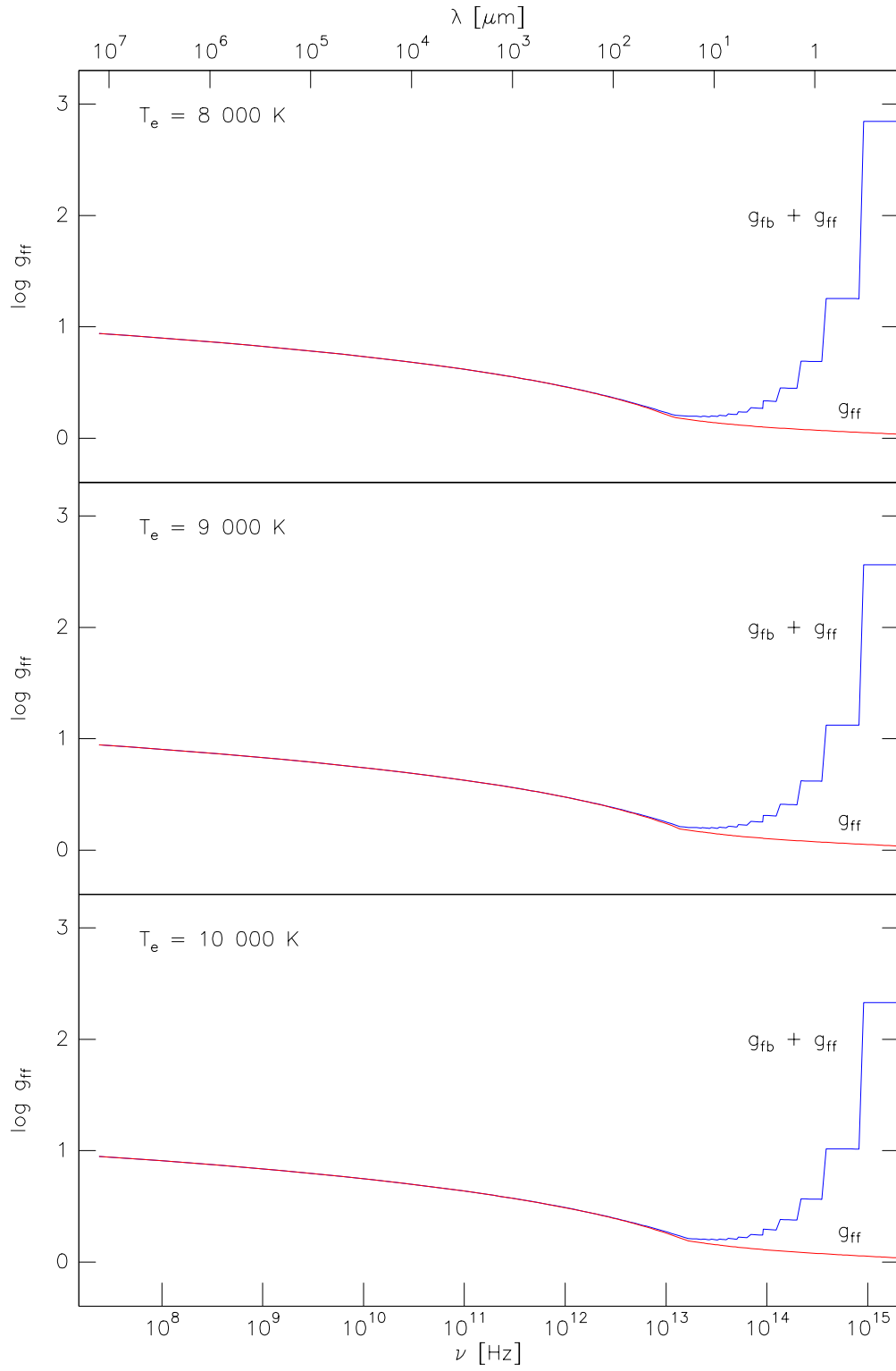


**Figure A.2:** Free-free and sum of free-free and free-bound gaunt factors for different electron temperatures. The free-bound gaunt factors play only a significant role in the high frequency region ( $\nu \gg 10^{13}\text{ Hz}$ ). In the FIR and radio range they vanish.

whereas Allen (1973) gave the following formula

$$g_{\text{ff}}(\nu, T) = 10.6 + 1.9 \log T - 1.26 \log \nu. \quad (\text{A.9})$$

In both cases  $Z = 1$  was inserted.

We plotted the free–free gaunt factors calculated with the above formulae in Figure A.1 for temperatures ranging from 8000 K (upper panel) to  $10^4$  K (lower panel). The gaunt factors within their valid wavelength ranges are drawn as solid lines whereas the dashed line regions mark the wavelength ranges where the approximations fail. For a continuous transition between the gaunt factors calculated in the short and long wavelength approximation, a cross point within the valid regions is necessary. Only Allen’s formula has one, and we choose it (like Waters & Lamers (1984) did) to describe the  $g_{\text{ff}}$  values in the FIR and radio range.

In Figure A.2 the sum of free–free and free–bound gaunt factors is given for the same temperatures. The free–bound gaunt factors become important in the NIR and visible, but for wavelengths longer than  $\sim 50 \mu\text{m}$  they are negligible. In addition, they decrease with increasing temperature, whereas the free–free gaunt factors show nearly no temperature dependence.

## Appendix B

# The oscillator strength of neutral hydrogen

To calculate the oscillator strength,  $f_{nn'}$ , we use the following general formula (Menzel & Pekeris 1935)

$$f_{nn'} = \frac{2^6}{3g_{n'}} \left| \frac{\left(\frac{n-n'}{n+n'}\right)^{2(n+n')}}{n^2 n'^2 \left(\frac{1}{n'^2} - \frac{1}{n^2}\right)^3} \frac{\Delta(n, n')}{(n-n')} \right|, \quad (\text{B.1})$$

where  $g_{n'}$  is the statistical weight of the lower level  $n'$ . It is convenient to parametrize the oscillator strength by  $f_{nn'} = g f'_{nn'}$ , with

$$f'_{nn'} = \frac{2^6}{3\sqrt{3}\pi g_{n'}} \frac{1}{\left(\frac{1}{n'^2} - \frac{1}{n^2}\right)^3} \left| \frac{1}{n^3} \cdot \frac{1}{n'^3} \right| \quad (\text{B.2})$$

which is known as Kramers' formula and which is an approximation, valid in the region of large quantum numbers (where  $g \simeq 1$ ).

$$g \equiv g_{\text{bb}}(n, n') = \pi\sqrt{3} \left| \left(\frac{n-n'}{n+n'}\right)^{2(n+n')} \cdot \frac{nn' \cdot \Delta(n, n')}{(n-n')} \right|, \quad (\text{B.3})$$

is a correction factor and is better known as the gaunt factor of bound-bound transitions between the discrete levels  $n$  and  $n'$ . The function  $\Delta(n, n')$  is defined as

$$\Delta(n, n') \equiv \left[ F\left(-n+1, -n', 1, -\frac{4nn'}{(n-n')^2}\right) \right]^2 - \left[ F\left(-n'+1, -n, 1, -\frac{4nn'}{(n-n')^2}\right) \right]^2 \quad (\text{B.4})$$

where  $F$  is the ordinary hypergeometric function

$$F(\alpha, \beta, \gamma, \chi) = 1 + \frac{\alpha\beta}{1!\gamma}\chi + \frac{\alpha(\alpha+1)\beta(\beta+1)}{2!\gamma(\gamma+1)}\chi^2 + \dots \quad (\text{B.5})$$

In the left panel of Figure B.1 the bound-bound gaunt factors for several hydrogen series are displayed. The values of  $g_{\text{bb}}(n, n')$  for all series converge against a limiting value, which becomes 1 for increasing lower quantum number  $n'$ . The right panel contains the oscillator strengths  $f_{nn'}$  of the individual bound transitions of the series indicated. Our values coincide with the ones calculated by Menzel & Pekeris (1935) which are plotted as black dots.

For large  $n$ , where  $g_{\text{bb}}(n, n')$  is nearly constant and the dependence of  $f_{nn'}$  with  $n$  for a fixed  $n'$  can be approximated by Eq. (B.2), the oscillator strength is roughly proportional to  $\sim n^{-3}$ .

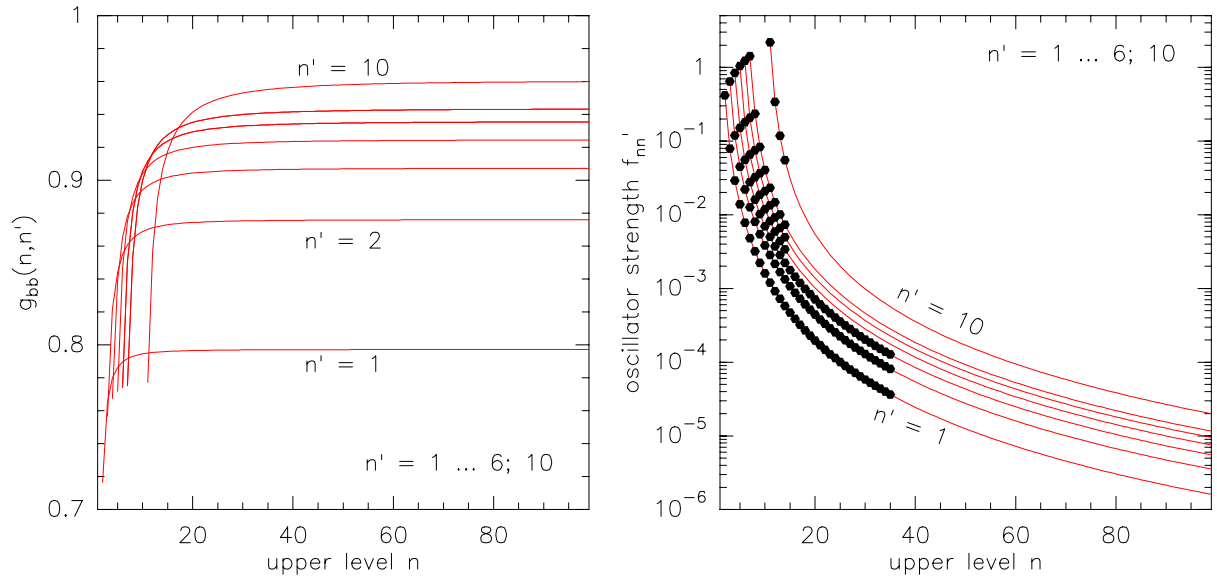


**Figure B.1:** *Left panel:* Gaunt factor  $g_{bb}(n, n')$  of bound-bound processes for different lower levels  $n'$ . *Right panel:* Oscillator strengths  $f'_{nn'}$  of the same levels. The values agree with the ones given by Menzel & Pekeris (1935) shown as the black dots.

# Appendix C

## Objects showing CO band emission

Here we list the objects showing the first overtone CO band emission. Table C.1 contains YSO that were observed with (mostly) too low spectral resolution which does not allow a derivation of the kinematical broadening mechanisms. In Table C.2 several parameters of the YSOs and their surroundings are summarized, and in Table C.3 the objects other than YSOs showing the CO band emission are mentioned.

Although the stellar parameters of these very different type stars cover a broad range, many of these objects seem to possess a circumstellar disk or at least a circumstellar gas and dust shell in connection with a bipolar outflow. This common feature of their circumstellar environment must therefore be of crucial importance for the possibility that the first overtone CO bands can arise in emission.

**Table C.1:** YSOs with spectra of (mostly) low resolution which do not allow a classification of the kinematics of the CO emitting region.

Name	highest resolution $\Delta v_{\text{res}}$ [km/s]	Variable <sup>a)</sup>	Ref.
AS 353 A	440	strongly	(1)
BN	5–18	strongly	(2)
GL 2789	480		(3)
IRAS 04239+2436	600		(4)
S 140 IRS 1	440	strongly	(1)
B 243 (=CEN 51) <sup>b)</sup>	545		(5);(6)
B 268 (=CEN 49)	545		(5);(6)
B 275 (=CEN 24)	545		(5);(6)
B 331 (=CEN 92)	545		(5);(6)
B 337 (=CEN 93)	545		(5);(6)

<sup>a)</sup> based on monitoring observations performed by Biscaya et al. (1997)

<sup>b)</sup> detection of CO band emission uncertain

*References:* (1) Carr (1989); (2) Scoville et al. (1983); (3) Geballe & Persson (1987); (4) Green & Lada (1996a); (5) Hanson & Conti (1995); (6) Hanson, Howarth & Conti (1997).

**Table C.2:** List of parameters for the YSOs and their environment exhibiting the CO first overtone bands in emission.

Name	Object	Spectral Type	Refs.	$L_{\text{bol}}$ [ $L_{\odot}$ ]	Refs.	$L_{*}$ [ $L_{\odot}$ ]	Refs.	$M_{*}$ [ $M_{\odot}$ ]	Refs.	Disk $R$ [AU]	$i_l^{\circ}$ <sup>(a)</sup>	Refs.	Remarks
AS 353 A	T Tau (active)	G0 or K0	(1)	5.8 7.2	(2) (3)								bipolar outflow: HH 32 A-D
BN Objekt	ZAMS	B0	(21)	$\leq 2 \cdot 10^4$	(21)			25					
DG TAU	T Tau (classical)	Ge K7-M0	(3) (4);(24)	7.2; 8.5 9.4; 6.4	(2);(3) (4);(24)	1.7 1.5	(5) (4)	0.56 1.8	(5) (3)	109 $\pm$ 22	20 $\pm$ 10	(6)	HH objects exciting star; $L_{\text{FIR}} \simeq 3.8 L_{\odot}$
GL2789 (= V 645 Cyg = AFGL 2789)	ZAMS	O8 - O9	(8)	$9 \cdot 10^4$	(7);(8)			29.1(?)	(3)				bipolar molecular outflow; disk?
IRAS 04239+2436	Class I			1.3 1.27	(15) (24)			$\leq 0.4$	(15)				strong stellar wind/ outflow; $L_{\text{FIR}} \simeq 1.16 L_{\odot}$
NGC 2024 IRS 2	ZAMS H AeBe	B0 - B0.5 B3	(9) (19)	$\sim 10^4$ $\sim 10^3$	(18) (19)			15	(16)				wind: outflow + rotation
SVS13 (= SSV13)	PMS Class I		(22)	115 66	(2) (20)			1	(16)	$9 \cdot 10^3$ b)		(23)	exciting star of HH 7 - HH 11
S106 IRS 4	BN-like	B0III - O9.5 V	(10);(17)	$2.4 \cdot 10^4$	(10)			25	(16)		$\sim 20$	(11)	disk + bipolar outflow
S140 IRS 1	BN-like		(17)										
V1331 Cyg	T Tau (peculiar)	F0 V	(12)			3	(12)						IR excess: $L_{\text{IR}} = 20 \pm 5 L_{\odot}$
WL16	H AeBe Class I	A(?)	(13) (22)	18 - 22	(13)			2.5	(13)				
1548 C27	H AeBe			740 580	(13) (14)	200	(13)	4	(13)				

<sup>a)</sup> inclination angle of the disk with respect to the line of sight ( $i = 0^{\circ}$  means edge on)

<sup>b)</sup> Star surrounded by an unresolved, very dense disk and a highly flattened disk-like structure of radius 9000 AU (23).

*References:* (1) Böhm & Raga (1987); (2) Cohen & Schwartz (1987); (3) Levreault (1988) and references therein; (4) Cabrit et al. (1990); (5) Beckwith et al. (1990); (6) Kitamura, Kawabe & Saito (1996); (7) McGregor, Persson & Cohen (1984); (8) Harvey & Lada (1980); (9) Chahabaev & Léna (1986); (10) Felli et al. (1985); (11) Riera et al. (1989); (12) Chavarría-K. (1981); (13) Najita et al. (1996); (14) Dent & Aspin (1992); (15) Green & Lada (1996); (16) Chandler, Carlstrom & Scoville (1995); (17) Simon et al. (1981); (18) Jiang, Perrier & Léna (1984); (19) Maihara, Mizutani & Suto (1990); (20) Cohen, Harvey & Schwartz (1985); (21) Moran et al. (1983); (22) Cabrit & André (1991); (23) Sandell et al. (1990); (24) Kenyon & Hartmann (1995).

**Table C.3:** List of parameters for the non-YSOs exhibiting the CO first overtone bands in emission.

Name	Object	Spectral Type	$L_{\text{bol}}$ [ $L_{\odot}$ ]	Remarks	Refs.
Sample of 63 high-luminosity LMC supergiants					
HD 268835	B[e]	B8	$2.6 \cdot 10^5$	a)	(1)
Hen S12	B[e]	B0.5	$2.4 \cdot 10^5$	a)	(1)
HD 38489	B[e]	B0	$3.9 \cdot 10^5$	a)	(1)
HD 37836	(peculiar)	O8	$1.3 \cdot 10^6$	a)	(1)
HD 269953		G0 Ia	$8.1 \cdot 10^5$	b)	(1)
HD 269723		G40	$3.1 \cdot 10^5$		(1)
Sample of 13 high-luminosity early-type emission line (P Cygni) stars <sup>1</sup>					
HR Car	S Doradus type		$7.9 \cdot 10^5$	b)	(2)
CPD -52° 9243	B[e]	~ B3 Ia	$2.5 \cdot 10^5$	c)	(2);(7)
CPD -57° 2874			$> 6.3 \cdot 10^4$	c)	(2)
GG Car	Bep	B0–B2	$5.0 \cdot 10^4$	c);d)	(2);(8)
He3 -1359		B8			(2)
BI Cru	Symbiotic		$3.2 \cdot 10^5$	c)	(2)
Sample of 21 post AGB stars / proto-planetary nebulae					
IRAS 19114+0002 (= HD 179821)		G5 Ia		e)	(3);(4)
IRAS 22223+4327 (= DO 41288)		G0 Ia			(3)
IRAS 22272+5435 (= HD 235858)		G5 Ia		f)	(3)
HD 101584		late B		d);e); h)	(4);(9)
HD 170756 (= AC Her)				e); g)	(4)
MWC 349	peculiar B[e]	O9 III; B0	$3 \cdot 10^4$	i)	(5);(6)

<sup>1</sup> The authors noted that the NIR spectra ( $1.0 - 2.5 \mu\text{m}$ ) of these high-luminosity early-type emission line stars show striking spectral similarities to those of embedded YSOs.

a) normal B supergiant (polar) stellar wind + dense equatorial disk

b) existence of a cool dust shell

c) hot dust; possibly a circumstellar disk

d) known as a binary

e) far IR excess

f) CO bands turned from emission to absorption over a 3 month interval

g) CO band variations are related to the pulsation period of the star: Absorption occurs when the photosphere is expanding (June 1987, August 1992); emission when it is contracting (November 1989)

h) its large NIR excess emission is thought to originate in a hot circumstellar disk

i) nearly edge on circumstellar disk + slow bipolar outflow

*References:* (1) McGregor, Hillier & Hyland (1988); (2) McGregor, Hyland & Hillier (1988); (3) Hrivnak, Kwok & Geballe (1994); (4) Oudmaijer et al. (1995); (5) Lamers et al. (1998); (6) Cohen et al. (1985); (7) Winkler & Wolf (1989); (8) Lopes et al. (1992); (9) Waters et al. (1998).





# Bibliography

- [1] Adams, F.C., Lada, C.J., Shu, F.H., 1987, ApJ 312, 788
- [2] Adams, F.C., Lada, C.J., Shu, F.H., 1988, ApJ 326, 865
- [3] Allen, C.W., 1973, *Astrophysical Quantities* (The Athlone Press, London), p. 103
- [4] Allen, D.A., Swings, J.P., 1976, A&A 47, 293
- [5] Altenhoff, W.J., Mezger, P.G., Wendker, H., Westerhout, G., 1960, Veröff. Sternwarte Bonn No. 59, 48
- [6] Altenhoff, W.J., Strittmatter, P.A., Wendker, H.J., 1981, A&A 93, 48
- [7] Altenhoff, W.J., Thum, C., Wendker, H.J., 1994, A&A 281, 161
- [8] Altenhoff, W.J., Wendker, H.J., 1973, Nature 241, 37
- [9] Andrillat, Y., Ciatti, F., Swings, J.P., 1982, Ap&SS 83, 423
- [10] Andrillat, Y., Jaschek, M., Jaschek, C., 1996, A&AS 118, 495
- [11] Andrillat, Y., Swings, J.P., 1976, ApJ 204, L 123
- [12] Baker, J.G., Menzel, D.H., 1938, ApJ 88, 52
- [13] Bally, J., Langer, W.D., 1982, ApJ 255, 143
- [14] Baldwin, J.E., Harris, C.S., Ryle, M., 1973, Nature 241, 38
- [15] Barlow, M.J., Cohen, M., 1977, ApJ 213, 737
- [16] Beckwith, S.V.W., Sargent, A.I., Chini, R.S., Güsten, R., 1990 AJ 99, 924
- [17] Biscaya, A.M., Rieke, G.H., Narayanan, G., Luhman, K.L., Young, E.T., 1997, ApJ 491, 359
- [18] Böhm, K.H., Raga, A.C., 1987, PASP 99, 265
- [19] Braes, L.L.E., Habing, H.J., Schoenmaker, A.A., 1972, Nature 240, 230
- [20] Brocklehurst, M., 1970, MNRAS 148, 417
- [21] Brussard, P.J., van de Hulst, H.C., 1962, Rev. Mod. Phys. 34, 507
- [22] Cabrit, S., André, P., 1991, ApJ 379, L 25
- [23] Cabrit, S., Edwards, S., Strom, S.E., Strom, K.M., 1990, ApJ 354, 687
- [24] Calvet, N., Patiño, A., Magris, C.G., D'Alessio, P., 1991, ApJ 380, 617

- [25] Carr, J.S., 1989, ApJ 345, 522
- [26] Carr, J.S., 1995, Ap & SS 224, 25
- [27] Carr, J.S., Tokunaga, A.T., 1992, ApJ 393, L 67
- [28] Carr, J.S., Tokunaga, A.T., 1995, J. Astrophys. Astron. S. 16, 331
- [29] Carr, J.S., Tokunaga, A.T., Najita, J., Shu, F.H., Glassgold, A.E., 1993, ApJ 411, L 37
- [30] Casali, M.M., Eiroa, C., 1995, Ap&SS 224, 17
- [31] Casali, M.M., Eiroa, C., 1996, A&A 306, 427
- [32] Casali, M.M., Matthews, H.E., 1992, MNRAS 258, 399
- [33] Chalabaev, A.A., Léna, P., 1986, A&A 168, L 7
- [34] Chandler, C.J., Carlstrom, J.E., Scoville, N.Z., Dent, W.R., Geballe, T.R., 1993, ApJ 412, L 71
- [35] Chandler, C.J., Carlstrom, J.E., Scoville, N.Z., 1995, ApJ 446, 793
- [36] Chandra, S., Maheshwari, V.U., Sharma, A.K., 1996, A&AS 117, 557
- [37] Chavarría-K., C., 1981, A&A 101, 105
- [38] Cohen, M., Bieging, J.H., Dreher, J.W., Welch, W.J., 1985, ApJ 292, 249
- [39] Cohen, M., Harvey, P.M., Schwartz, R.D., 1985, ApJ 296, 633
- [40] Cohen, M., Schwartz, R.D., 1987, ApJ 316, 311
- [41] Dent, W.R.F., Aspin, C., 1992, MNRAS 259, 401
- [42] Dreher, J.W., Welch, W.J., 1983, AJ 88, 1014
- [43] Dunham, J. L., 1932a, Phys.Rev. 41, 713
- [44] Dunham, J. L., 1932b, Phys.Rev. 41, 721
- [45] Escalante, V., Rodríguez, L.F., Moran, J.M., Cantó, J., 1989, Rev. Mex. Astron. Astrofis. 17, 11
- [46] Farrenq, R., Guelachvili, G., Sauval, A. J., Grevesse, N., Farmer, C. B., 1991, J.Mol.Spectrosc. 149, 375
- [47] Felli, M., Simon, M., Fischer, J., Hamann, F., 1985, A&A 145, 305
- [48] Geballe, T.R., Persson, S.E., 1987, ApJ 312, 29
- [49] Geisel, S.L., 1970, ApJ 161, L 105
- [50] Gerardy, C.L., Fesen, R.A., Höflich, P., Wheeler, J.C., 1999, *astro-ph/9912433 (submitted to AJ)*
- [51] Green, T.P., Lada, C.J., 1996a, ApJ 461, 345
- [52] Green, T.P., Lada, C.J., 1996b, AJ 112, 2184

- [53] Gregory, P.C., Seaquist, E.R., 1973, Nat. Phys. Sci. 242, 101
- [54] Gronenschild, E.H.B.M., Mewe, R., 1978, A&AS 32, 283
- [55] Hamann, F., Simon, M., 1986, ApJ 311, 909
- [56] Hamann, F., Simon, M., 1988, ApJ 327, 876
- [57] Hanson, M.M., Conti, P.S., 1995, ApJ 448, L 45
- [58] Hanson, M.M., Howarth, I.D., Conti, P.S., 1997, ApJ 489, 698
- [59] Hartmann, L., Kenyon, S.J., 1996, ARA&A 34, 207
- [60] Harvey, P.M., Lada, C.J., 1980, ApJ 237, 61
- [61] Harvey, P.M., Thronson, H.A., Gatley, I., 1979, ApJ 231, 115
- [62] Hayashi, C., 1981, Suppl.Prog.Theor.Phys. 70, 35
- [63] Herzog, A.D., Gehrz, R.D., Hackwell, J.A., 1980, ApJ 236, 189
- [64] Hjellming, R.M., Blankenship, L.C., Balick, B., 1973 Nat. Phys. Sci. 242, 84
- [65] Hummer, D.G., Storey, P.J., 1987, MNRAS 224, 801
- [66] Hollenbach, D., Johnstone, D., Lizano, S., Shu, F., 1994, ApJ 428, 654
- [67] Hrivnak, B.J., Kwok, S., Geballe, T.R., 1994, ApJ 420, 783
- [68] Jiang, D.R., Perrier, C., Léna, P., 1984, A&A 135, 249
- [69] Kelly, D.M., Rieke, G.H., Campbell, B., 1994, ApJ 425, 231
- [70] Kenyon, S.J., Hartmann, L., 1995, ApJS 101, 117
- [71] Kitamura, Y., Kawabe, R., Saito, M., 1996, ApJ 465, L 137
- [72] Kraus, M., 1997, Diploma Thesis, University of Bonn
- [73] Kuhl, L.V., 1973, Astrophys. Lett. 14, 141
- [74] Lada, C.J., 1987, in: *Star forming Regions*, IAU Symposium No. 115, edited by M. Peimbert and J. Jugaku (Reidel, Dordrecht), p. 1
- [75] Lamers, H.J.G.L.M., Zickgraf, F.-J., de Winter, D., Houziaux, L., Zorec, J., 1998, A&A 340, 117
- [76] Lee, T.A., 1970, PASP 82, 765
- [77] Leinert, C., 1986, A&A 155, L 6
- [78] Levreault, R.M., 1988, ApJ 330, 897
- [79] Lopes, D.F., Damineli Neto, A., de Freitas Pacheco, J.A., 1992, A&A 261, 482
- [80] Maihara, T., Mizutani, K., Suto, H., 1990, ApJ 354, 549
- [81] Mariotti, J.M., Chelli, A., Foy, R., Léna, P., Sibille, F., Tchountonov, G., 1983, A&A 120, 237

- [82] Martin, S.C., 1997, ApJ 478, L 33
- [83] Martín–Pintado, J., Bachiller, R., Thum, C., Walmsley, M., 1989, A&A 215, L 13
- [84] Martín–Pintado, J., Neri, R., Thum, C., Planesas, P., Bachiller, R., 1994, A&A 286, 890
- [85] Mathis, J.S., 1990, ARA&A 28, 37
- [86] Mathis, J.S., Rumpl, W., Nordsieck, K.H., 1977, ApJ 217, 425
- [87] McGregor, P.J., Hillier, D.J., Hyland, A.R., 1988, ApJ 334, 639
- [88] McGregor, P.J., Hyland, A.R., Hillier, D.J., 1988, ApJ 324, 1071
- [89] McGregor, P.J., Persson, S.E., Cohen, J.G., 1984, ApJ 286, 609
- [90] Menzel, D.H., Pekeris, C.L., 1935, MNRAS 96, 77
- [91] Merrill, P.W., Humason, M.L., Burwell, C.G., 1932, ApJ 76, 156
- [92] Mitskevich, A.S., 1995a, A&A 298, 219
- [93] Mitskevich, A.S., 1995b, A&A 298, 231
- [94] Moran, J.M., Garay, G., Reid, M.J., Genzel, R., Wright, M.C.H., Plambeck, R.L., 1983, ApJ 271, L 31
- [95] Najita, J., Carr, J.S., Glassgold, A.E., Shu, F.H., Tokunaga, A.T., 1996, ApJ, 462, 919
- [96] Olmon, F.M., 1975, A&A 39, 217
- [97] Osterbrock, D.E., 1989, *Astrophysics of Gaseous Nebulae and Active Galactic Nuclei* (University Science Books, Mill Valley), p. 73 ff
- [98] Oudmaijer, R.D., Waters, L.B.F.M., van der Veen, W.E.C.J., Geballe, T.R., 1995 A&A 299, 69
- [99] Panagia, N., Felli, M., 1975, A&A 39, 1
- [100] Planesas, P., Martín–Pintado, J., Serabyn, E., 1992, ApJ 386, L 23
- [101] Pringle, J.E., 1981, ARA&A 19, 137
- [102] Riera, A., Mampaso, A., Phillips, J.P., Vilchez, J.M., 1989, A&A 210, 351
- [103] Rodríguez, L.F., Bastian, T.S., 1994, ApJ 428, 324
- [104] Salpeter, E.E., 1974, ApJ 193, 585
- [105] Sandell, G., Aspin, C., Duncan, W.D., Robson, E.I., Dent, W.R.F., 1990, A&A 232, 347
- [106] Schmid–Burgk, J., 1982, A&A 108, 169
- [107] Schwartz, P.R., 1980, PASP 92, 534
- [108] Schwartz, P.R., Spencer, J.H., 1977, MNRAS 180, 297
- [109] Scoville, N., Hall, D.N.B., Kleinmann, S.G., Ridgeway, S.T., 1979, ApJ 232, L 121
- [110] Scoville, N., Kleinmann, S.G., Hall, D.N.B., Ridgeway, S.T., 1983, ApJ 275, 201

- [111] Scoville, N.Z., Krotkov, R., Wang, D., 1980, ApJ 240, 929
- [112] Simon, M., Righini-Cohen, G., Felli, M., Fischer, J., 1981, ApJ 245, 552
- [113] Smith, H.A., Strelitski, V., Miles, J.W., Kelly, D.M., Lacy, J.H., 1997, AJ 114, 2658
- [114] Spyromilio, J., Leibundgut, B., 1996, MNRAS 283, L 89
- [115] Spyromilio, J., Meikle, W.P.S., Learner, R.C.M., Allen, D.A., 1988 Nature 334, 327
- [116] Storey, P.J., Hummer, D.G., 1995, MNRAS 272, 41
- [117] Strelitski, V.S., Haas, M.R., Smith, H.A., Erickson, E.F., Colgan, S.W.J., Hollenbach, D.J., 1996, Sci 272, 1459
- [118] Swings, P., Struve, O., 1942, ApJ 95, 152
- [119] Thompson, R., Reed, M.A., 1976, ApJ 205, L 159
- [120] Thum, C., Martín-Pintado, J., Bachiller, R., 1992, A&A 256, 507
- [121] Thum, C., Martín-Pintado, J., Quirrenbach, A., Matthews, H.E., 1998, A&A 333, L 63
- [122] Thum, C., Matthews, H.E., Harris, A.I., Tacconi, L.J., Schuster, K.F., Martín-Pintado, J., 1994a, A&A 288, L 25
- [123] Thum, C., Matthews, H.E., Martín-Pintado, J., Serabyn, E., Planesas, P., Bachiller, R., 1994b, A&A 283, 582
- [124] Thum, C., Strelitski, V.S., Martín-Pintado, J., Matthews, H.E., Smith, H.A., 1995, A&A 300, 843
- [125] de Vaucouleurs, G., 1970, Science 167, 1203
- [126] Walmsley, C.M., 1990, A&AS 82, 201
- [127] Waters, L.B.F.M., Lamers, H.J.G.L.M., 1984, A&AS 57, 327
- [128] Waters, L.B.F.M., Morris, P.W., Voors, R.H.M., Lamers, H.J.G.L.M., 1998, in: *B[e] Stars*, edited by A.M. Hubert & C. Jaschek (Kluwer Academic Publisher, Netherlands), p. 111
- [129] White, R.L., Becker, R.H., 1985, ApJ 297, 677
- [130] Winkler, H., Wolf, B., 1989, A&A 219, 151



# Acknowledgement

First of all I would like to thank my supervisor, Dr. Endrik Krügel, who opened the possibility for the treatment of this interesting subject, who was always willing to discussion, and who gave me a free hand during the elaboration of the details of this thesis.

I am also pleased to thank Prof. Dr. Hans-Jörg Fahr who was kindly willing to examine and report on this thesis.

I heartily thank Prof. Dr. Richard Wielebinski for including me in his radio continuum group and for the financial support during my stay at the Max-Planck-Institut of Radioastronomy without which this thesis would have never been finished in this short time.

A special thank goes to Dr. Tom Geballe who took the observations of the high resolution spectra at UKIRT, and to Dr. Clemens Thum who put all the observed NIR spectra at my disposal and with whom I had many discussions concerning MWC 349.

It is a great pleasure for me to thank Dr. William Sherwood for his proof-reading, and for the interesting and informative discussions which resulted in several new ideas for future investigations.

In addition, I would like to thank my friends, Carsten van de Bruck, Sabina Cheba, Matthias Soika, Bülent Uyaniker, and Aylin Yar, for lots of discussion sessions during our obligatory coffee breaks and for many relaxing events we had together.

I also thank my colleagues, Matthias Kadler, Andrea Löhr, Bernd Weferling, and Volker Zota for the friendly and informal atmosphere we had in our ‘Kinderzimmer’.

Last but not least I owe my boy-friend, Dieter Nickeler, a great debt of gratitude, for numerous discussions and for his proof-reading of the thesis. He was always right behind me, and for his constant support all the time I have to thank him so much.